

Metastability and Depinning in Inhomogeneous Driven Dissipative Systems

Dissertation
zur Erlangung des Doktorgrades
des Fachbereichs Physik
der Universität Hamburg

vorgelegt von
Thorsten Dröse
aus Hamburg

Hamburg
2001

Gutachter der Dissertation:

Prof. Dr. C. de Morais Smith
Prof. Dr. D. Fay

Gutachter der Disputation:

Prof. Dr. C. de Morais Smith
Prof. Dr. J. Appel

Datum der Disputation:

19. Oktober 2001

Dekan des Fachbereichs Physik und

Vorsitzender des Promotionsausschusses: Prof. Dr. F.-W. Büßer

Abstract

In many physical systems inhomogeneities are present in the form of system boundaries, disorder, or they are due to the discrete structure of the system. In this thesis the influence of inhomogeneities on the decay from metastable states and on the depinning transition in certain driven dissipative systems is investigated.

First, the thermal and quantum decay of finite linear chains with an overdamped dynamics are studied. The decay rate is calculated on the basis of the thermodynamic method commonly known from rate theory. Further, the crossovers between the various metastability regimes that arise due to the interplay of the relevant energy scales are analyzed.

At high temperatures the escape process mainly occurs via the lowest lying saddle-point solutions of the chain's energy functional. It is shown that depending on the coupling strength these configurations are either uniform or bent. Correspondingly, the thermal regime is divided into a rigid and an elastic phase. The crossover between these regimes is continuous. Close to the rigid-to-elastic crossover, the unstable configurations are localized at the boundaries of the system. In large systems with high energy barriers, the elastic decay takes place via nucleation in the bulk.

Below a characteristic crossover temperature, quantum tunneling dominates the escape process. As in the thermal regime, rigid and elastic phases are found in the quantum regime. In the rigid quantum regime decay is preferably occurring via unique saddle-point solutions of the Euclidean action describing the simultaneous tunneling of the chain beads. In the elastic phase the decay occurs via a non-uniform saddle-point solution where the particles leave the metastable state one after another. The quantum rigid-to-elastic crossover can be both continuous and discontinuous. The various regimes are summarized in a decay diagram. The results are discussed in the context of topological excitations in micro- and nano-structured superconductors like Josephson junction arrays and layered superconductors with columnar defects.

Finally, the depinning transition of a driven chain-like system in the presence of frustration and quenched disorder is studied neglecting thermal or quantum fluctuations. This analysis is motivated by recent transport experiments on artificial vortex-flow channels in superconducting thin films. Starting with a London description of the vortices, the complexity of the model is reduced by mapping it onto a generalized Frenkel-Kontorova model and its continuous equivalent, the Sine-Gordon model. Within this simplified description the depinning transition is studied.

In the absence of disorder, frustration reduces the depinning threshold in the commensurate phase which nearly vanishes in the incommensurate regime. Depinning of the driven frustrated chain occurs via unstable configurations that are localized at the boundaries of the sample and evolve into topological defects which move freely through the entire sample.

In the presence of disorder, topological defects can be also generated in the bulk. Further, disorder leads to pinning of topological defects. It is found that weak disorder effectively reduces the depinning threshold in the commensurate phase, but increases the threshold in the incommensurate phase.

Kurzfassung

In vielen physikalischen Systemen treten Inhomogenitäten in Form von Systemgrenzen, Unordnung oder aufgrund der diskreten Struktur der Systeme auf. In dieser Arbeit wird der Einfluss von Inhomogenitäten auf den Zerfall metastabiler Zustände und den Depinning-Übergang in bestimmten getriebenen dissipativen Systemen untersucht.

Zunächst wird der thermische und quantenmechanische Zerfall endlicher linearer Ketten mit überdämpfter Dynamik studiert. Die Zerfallsrate wird mit der aus der Ratentheorie bekannten thermodynamischen Methode berechnet. Weiterhin werden die Übergänge zwischen diversen metastabilen Phasen analysiert, die durch das Wechselspiel der relevanten Energien auftreten.

Bei hohen Temperaturen findet der Zerfallsprozess hauptsächlich über Kettenkonfigurationen statt, die durch die niedrigsten Sattelpunktlösungen des Energiefunktionalen beschrieben werden. Es wird gezeigt, dass diese Konfigurationen in Abhängigkeit der Kopplungsstärke entweder gerade oder gebogen sind. Dementsprechend ist das thermische Regime in eine steife und eine elastische Zerfallsphase unterteilt. Der Übergang zwischen diesen Phasen ist kontinuierlich. Nahe dem Übergang vom steifen zum elastischen Zerfall sind die instabilen Konfigurationen an der Systemgrenze lokalisiert. In großen Systemen mit hohen Energiebarrieren kann der Zerfall durch Nukleation im Innern der Probe dominiert werden.

Unterhalb einer charakteristischen Übergangstemperatur dominiert Quantentunneln den Zerfallsprozess. Wie im thermischen findet man auch im quantenmechanischen Regime steife und elastische Phasen. In der steifen quantenmechanischen Phase findet der Zerfall vornehmlich über uniforme Sattelpunktlösungen der Euklidischen Wirkung statt, die das gleichzeitige Tunneln aller Kettenglieder beschreiben. In der elastischen Phase sind die Sattelpunktlösungen hingegen nicht uniform und die Teilchen verlassen ihre Falle nacheinander. Der quantenmechanische Übergang von steifem zu elastischem Zerfall kann sowohl kontinuierlich als auch diskontinuierlich sein. Die verschiedenen Phasen sind in einem Zerfallsdiagramm aufgetragen. Die Ergebnisse werden im Zusammenhang mit metastabilen Zuständen von topologischen Anregungen in mikro- und nanostrukturierten Proben wie Josephson-Kontakt-Gittern und geschichteten Supraleitern mit kolumnaren Defekten diskutiert.

Schließlich wird der Depinning-Übergang einer getriebenen Kette in Anwesenheit von Frustration und statischer Unordnung studiert, wobei thermische oder quantenmechanische Fluktuationen vernachlässigt werden. Diese Analyse ist durch kürzlich durchgeführte Transportmessungen in supraleitenden Filmen mit künstlichen Wirbelflusskanälen motiviert worden. Ausgehend von einer London-Beschreibung der Vortizes wird die Komplexität des Modells durch Abbildung auf ein verallgemeinertes Frenkel-Kontorova-Modell und seinem kontinuierlichen Äquivalent, dem Sine-Gordon-Modell, reduziert. Anhand dieser vereinfachten Beschreibung wird der Depinning-Übergang studiert.

In Abwesenheit von Unordnung reduziert Frustration in der kommensurablen Phase die Depinning-Schwelle, die in der inkommensurablen Phase fast vollständig verschwindet. Das Losreißen einer getriebenen frustrierten Kette findet über instabile Zustände statt, die zunächst an der Systemgrenze lokalisiert sind und sich dann in topologische Defekte entwickeln, die sich frei durch die gesamte Probe bewegen.

In ungeordneten Systemen können topologische Defekte auch an Schwachstellen im Probeninnern entstehen. Schon bei schwacher Unordnung wird dadurch die kritische Kraft in der kommensurablen Phase reduziert. Im inkommensurablen Fall erhöht sich die kritische Kraft im Vergleich zum geordneten System durch eine effektiv höhere Dichte von Haftzentren.

Contents

1	Introduction	3
2	Decay from metastable states: crossovers	7
2.1	Rate theory	9
2.1.1	Classical rate	10
2.1.2	Quantum rate	19
2.2	Model	22
2.2.1	Euclidean action	22
2.2.2	Physical systems	22
2.2.3	Extrema of the Euclidean action	25
2.3	Thermally activated decay	27
2.3.1	Crossover from rigid to elastic decay	27
2.3.2	Pre-exponential factor	32
2.3.3	Discussions	36
2.4	Quantum statistical decay	40
2.4.1	Onset of quantum fluctuations	40
2.4.2	Crossover temperature from thermal to quantum decay	42
2.4.3	Instantons	43
2.4.4	Iterative perturbation scheme	44
2.4.5	Nonuniform instanton solution	46
2.4.6	Decay diagram and decay rate	50
2.4.7	Discussions	53
3	Depinning in artificial vortex channels	55
3.1	Motivation	56
3.2	A model for artificial vortex channels	58
3.2.1	Channel with a perfect vortex lattice in the environment	58
3.2.2	Equation of motion	59
3.2.3	Commensurate-Incommensurate Transition	61
3.2.4	Depinning in the presence of boundaries	64
3.2.5	Preliminary comparison with experimental data	70
3.2.6	Channel with a distorted vortex lattice in the environment	71
3.2.7	Depinning in a channel with distorted environment	74

3.2.8	Depinning in a channel with randomly displaced edge vortices . . .	76
3.3	Comparison with Experimental Data	83
3.4	Discussions and Conclusions	86
4	Summary	91
A	Thermal prefactor	96
A.1	Curvature Matrix: Determinant and eigenvalues	96
A.1.1	Recurrence relation for the Hessian matrix	96
A.1.2	Uniform case	98
A.1.3	Nonuniform case	99
A.2	Prefactor in the crossover regime	100
A.2.1	Rigid regime ($\Delta \lesssim \Delta_*$)	100
A.2.2	Elastic regime ($\Delta \gtrsim \Delta_*$)	101
	References	103

Chapter 1

Introduction

Driven systems consisting of particles that interact with one another and with their environment exhibit a variety of complex physical phenomena. Many of these effects arise from the interplay between the various ingredients present in such systems. For example, the driving force is promoting motion. On the other hand, the potential energy landscape produced by the surrounding may lead to barriers that might not be overcome by the particles, leading to localization. However, thermal and quantum fluctuations may delocalize the particles. The situation becomes more complex due to interactions between the particles and disorder that is present in many systems. Consequently, many phenomena that arise in these complex systems are either poorly understood or unexplored. In many cases, one is forced to reduce the complexity of the systems by concentrating on the most dominant effects in order to achieve at least a partial, but satisfactory description.

A common characteristic of driven systems with potential energy barriers is the existence of a threshold force above which flow-like motion occurs and below which rare creep-like events can only be triggered by thermal or quantum fluctuations. In this thesis, we focus on two interesting aspects occurring in the regime around the threshold. One topic is the escape from metastable states due to thermal and quantum fluctuations below the threshold force. The second subject is the depinning transition occurring at and the dynamical behavior just above the threshold.

A system is in a metastable state when the decay time from this state is large compared to all other intrinsic time scales. There are numerous examples of processes in physics, chemistry, biology and engineering where a system rests in a metastable state for a relatively long period before leaving its trap by traversing an energy barrier [1].

At high temperatures the decay is mainly induced by thermal excitations over the energy barrier. Cooling the sample, the thermal fluctuations freeze out and quantum tunneling through the barrier may become relevant. For a single particle trapped in the local minimum of a potential, the decay scenario has been described in the whole temperature range from thermally activated decay at high temperatures to quantum tunneling at low temperatures within a thermodynamic method [2–12]. The decay of fields from a metastable state was introduced in the context of homogeneous nucleation induced by thermal fluctuations [13–15]. A familiar example for homogeneous nucleation is the spon-

taneous formation of a sufficiently large droplet of liquid in a super-saturated vapor. Once having exceeded a critical size this droplet rapidly grows and brings about condensation of the entire sample: the metastable vapor phase decays into the stable liquid phase.

The concept of homogeneous nucleation triggered by thermal [14, 15] or quantum fluctuations [16, 17] is certainly appealing. However, in many condensed matter samples inhomogeneities are present. Then the interesting question arises, in which systems do inhomogeneities play a crucial role in the escape process ?

In this thesis we analyze the influence of inhomogeneities from two perspectives. First, we study the effect of boundaries and discreteness on the thermal and quantum decay from a metastable state of a many-particle system. Second, we discuss the depinning of such a system at its boundary or at a weak-pinning site of a randomized potential.

Chapter 2 is devoted to the escape of several elastically coupled degrees of freedom forming a chain that is initially trapped in a local minimum of the potential energy landscape. A chain is an intermediate object between a particle, which is zero-dimensional and an infinite line, which is one-dimensional. For small chains, the important inhomogeneities are the boundaries of the system. However, beyond a certain length the decay mainly takes place via bulk excitations. Hence, one expects that the decay behavior is different for chains of various lengths. Further, it is determined by three competing energy scales: temperature, coupling strength and barrier height of the potential. Thus, there are several distinct decay regimes. Measuring the decay rate, various crossovers can be observed upon varying the system parameters. These crossovers display some analogies with equilibrium phase transitions. Accordingly, the crossovers are classified into first-order and second-order transitions, depending on whether the first or second derivative of the decay rate becomes discontinuous, respectively [6, 18]. A well-studied example is the crossover from thermal to quantum decay. Since most to-date-known metastable systems display second order thermal-to-quantum crossovers, it has become quite popular to search for experimentally accessible systems that show first-order transitions [18, 19].

The elastic chain can be a model for current-driven discrete Josephson transmission lines (DJTL) [20]. These parallel-coupled one-dimensional arrays of Josephson junctions (JJ's) can be seen as the discrete version of a long JJ. They have gained increasing attention since the first overdamped flux-flow devices have been built based on low-temperature [21] and high-temperature superconductors [22]. These days experimentalists start to investigate the decay of metastable states in long JJ and discrete transmission lines [23]. However, only a few theoretical results are available for specific limits, concentrating on long *underdamped* JJ's [24–26]. In this thesis we will study various parameter regimes and the crossovers that occur in the decay of *moderately* and *strongly damped* systems. The evaluation of the decay rate is performed within the framework of the thermodynamic method originally developed to model thermally activated decay processes [13–15, 27] and later generalized to the quantum regime [16, 17]. We determine the hitherto unknown decay rate of a chain of overdamped degrees of freedom trapped in a potential with the shape of a cubic parabola. The theory is mainly discussed in the context of JJ devices and vortices in type-II superconductors with columnar defects.

A different topic is considered in Chapter 3, where the depinning transition in driven

systems is studied. Simply spoken, depinning occurs when the driving force is equal to the pinning force due to the potential energy landscape. The depinning process is influenced by the presence of inhomogeneities like system boundaries or quenched disorder in the bulk. Both types of inhomogeneities are considered in Chapter 3. We do not investigate the effect of thermal or quantum fluctuations which we expect to simply smear the depinning transition in an extremely narrow parameter regime.

Depinning transitions occur in a variety of physical systems, mainly probed by transport experiments. Well-studied driven systems, where quenched disorder is dominant, are charge density waves (CDW's) submitted to an electric field [28], the two-dimensional electron gas in a magnetic field which forms a Wigner crystal moving under an applied voltage [29], magnetic bubbles moving under an applied magnetic field gradient [30, 31], and current-driven JJ arrays [32, 33]. Depinning may also be important to understand tribology and solid friction [34], surface growth of crystals with quenched bulk or substrate disorder, and domain walls in incommensurate solids [35]. A very prominent example of driven systems displaying a depinning transition are vortices in dirty type-II superconductors [36]. In the presence of a transport current the vortices are dragged by a Lorentz force. The interplay between the elasticity of the vortex lattice and the impurities present in the substrate leads to a rich phenomenology with many static and dynamic phases. A crucial question in both the dynamics and the statics is whether – in addition to thermal fluctuations – quenched disorder produces topological defects in the periodic structure. Whereas in the absence of topological defects it is sufficient to consider only elastic deformations with depinning causing elastic flow, the dynamics will be governed by plastic flow, if topological defects exists.

One expects plastic motion to become important for either strong disorder, high temperature, or near the depinning transition in low dimensions. Indeed, experiments and numerical simulations give evidence for the existence of plastic motion. The H-T diagram of type-II superconductors displays regions of both elastic and plastic flow [37, 38]. Other experimental observations that have been attributed to plastic flow are the peak effect [39, 40], unusual broadband noise [41], and steps in the I-V curve [42].

Close to the depinning threshold and in strongly disordered samples, depinning is observed to occur through “plastic channels” between pinned regions. This type of plastic flow has been found in numerical simulations of a two-dimensional thin film geometry [43–45]. Above the threshold, the filamentary channels become both denser and broader. Measurements of the differential resistance of MoGe films display abrupt steps, which could be interpreted in terms of plastic depinning [46].

To study the plastic depinning of vortices, artificial easy-flow channels have been manufactured [47, 48]. The samples are typically made of type-II superconducting thin films which consist of a fairly strong pinning layer on top of a weakly pinning base layer. The artificial vortex flow channels are fabricated by etching away stripes of the stronger pinning top layer. In the Meissner phase, vortices penetrate the sample. Applying a current perpendicular to the channel direction, the resulting Lorentz force in the direction of the channel drives the vortices. Since the influence of point-like material defects in the weak pinning channel is negligible, channel vortices are mainly pinned indirectly via the interaction with

the stronger pinned vortices in the channel environment. Above a threshold force, plastic depinning of the vortices inside the channel takes place. In contrast to natural channels, the depinning threshold force displays interesting oscillations when the externally applied magnetic field is varied. The position of the threshold force maxima hint at commensurability effects between the vortex lattice in the environment and in the channel [49]. The magnitude of the depinning force minima and maxima indicate that lattice distortions produced by quenched disorder in the pinned channel environment is relevant in these samples. In this thesis, we study the depinning and the dynamical behavior of artificial easy-flow channels theoretically. Starting from a London description of vortices inside and outside the channel, we first derive the coefficients of a generalized Frenkel-Kontorova model [50] for a perfectly ordered vortex lattice. The force-velocity curve of this simple model displays a drastic decrease of the threshold pinning force when topological defects enter the system via the system boundaries. However, the experimental data show a smooth variation of the pinning force as a function of magnetic field. The behavior suggests that disorder in the channel edges may lead to smoothening of the transition from the topologically ordered to the defective state. In order to investigate the transition in presence of disorder, we take into account that the vortex lattice in the channel environment is distorted due to impurities in the superconducting substrate. To determine the characteristic current-voltage or force-velocity curves, the problem is most conveniently tackled with numerical molecular dynamics simulations. This method enables us also to nicely visualize how depinning occurs in the topologically ordered and defective regime. It turns out that systems that are topologically ordered in the static phase depin at the boundary or by generating mobile defect droplets at weak spots in the random channel potential. In the defective static phase the pre-existing topological defects are pinned by the random potential. Then the depinning transition occurs via a release of these defects at the threshold.

The thesis is organized as follows. In Chapter 2, we investigate crossovers in the thermal and quantum decay of interacting particles in a metastable state. After a short review of rate theory in Section 2.1 we introduce a model of elastically coupled particles interacting with their environment in Section 2.2. Their thermally activated escape from a metastable state is explored in Section 2.3. The quantum statistical decay is investigated in Section 2.4. The subject of Chapter 3 is the depinning transition. After discussing the experiments that motivated the theoretical study in Section 3.1, we introduce the model in Section 3.2. Further, in this Section the results concerning the depinning transition are presented. They are compared to experimental data in Section 3.3, and discussed in Section 3.4. A summary of the thesis is given in Chapter 4.

Chapter 2

Crossovers in the decay from metastable states

Imagine a potential with a local minimum which is not the global one. A particle interacting with a heat bath performs a Brownian motion in the potential landscape. Once the particle is trapped in the local potential minimum it will need some time before it eventually leaves the well. The escape can be due to purely classical effects, such that the particle is kicked out of the well by a thermal fluctuation or it can be due to quantum tunneling through the energy barrier between the well and its exterior. When the time during which the particle is localized in the well is large compared to all other intrinsic time scales, the system is said to be metastable. Important time scales are the correlation time t_c of the noise generated by the heat bath, the thermal time $\hbar/k_B T$ and the time scales $t_a = \omega_a^{-1}$ and $t_s = \omega_s^{-1}$ associated with the curvature of the potential at the bottom of the well and the saddle point, respectively. Weak metastability implies that the energy V_s to activate the particle from the bottom of the well to the top of the barrier is by far the largest energy of the problem. It has to be much larger than the thermal energy, $V_s \gg k_B T$ to ensure that thermal activation is a rare event. On the other hand, $V_s \gg \hbar\omega_a$ guarantees that the well is deep enough to localize a quantum particle.

The main quantity of interest is the decay rate Γ , which is the probability per unit time that the system escapes from its metastable state. A convenient parameterization of the decay rate

$$\Gamma \sim P \exp(-A) \tag{2.1}$$

has been proposed by Van't Hoff [51] and Arrhenius [52] at the end of the nineteenth century. The pre-exponential factor P is the attempt frequency of the particle in the well towards the barrier and A is a dimensionless measure of the strength of the barrier. The main question we are concerned with in this chapter is how P and A behave as a function of externally tunable parameters for a system with many degrees of freedom, where the rate displays transitions between various decay regimes.

One transition is the crossover from thermal to quantum decay. Cooling a sample, the thermal fluctuations freeze out and below a characteristic temperature T_0 thermally

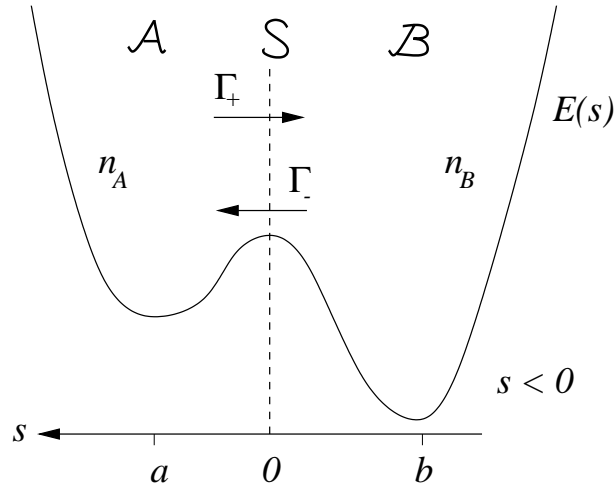


Figure 2.1: The populations n_A and n_B of the two states \mathcal{A} and \mathcal{B} , respectively, vary whenever the generalized coordinate s characterizing the state of a system crosses the dividing surface \mathcal{S} at $s = 0$. Transitions from \mathcal{A} to \mathcal{B} (\mathcal{B} to \mathcal{A}) occur at a constant rate Γ_+ (Γ_-).

assisted quantum tunneling is the main mechanism that leads to decay [2, 6–12]. The more complex a physical system is, the more parameters can be varied. Hence, one expects that upon tuning these parameters, the system may be driven through various transitions marking the borderlines between several distinct parameter regimes. In this chapter we study the statistical decay of N elastically coupled particles, each of them initially trapped in a local minimum of the single particle potential. One then has three competing energy scales that may be altered: the temperature, the energy barrier and the coupling strength. Accordingly, one expects that in addition to the thermal-to-quantum crossover further transitions should occur. Indeed, one finds a rigid phase, where the particles behave as a rigid rod and decay together, as well as an elastic phase, where the particles most probably decay via a bent configuration. One finds regimes, where boundary effects are important and others, where the decay occurs via excitations in the bulk. This provides an interesting model to study the crossovers between the various phases.

The phenomenological model analyzed in this thesis can be applied to a number of physical systems, however, here we mainly concentrate on crossovers occurring in the decay of metastable states in JJ devices, where the phenomena are most likely to be observed with experimental techniques available today. A short discussion in the context of vortices in artificially structured type-II superconductors is also given. Before we analyze this system in detail in the next sections, let us give a short introduction to rate theory.

2.1 Rate theory

Let us consider an ensemble of n systems, n_A in region \mathcal{A} and n_B in region \mathcal{B} in the space of possible states, see Fig. 1. On time scales much larger than the characteristic time scale t_s of microscopic processes, $t \gg t_s$, let the time evolution of the populations n_A and n_B be described by the rate equation

$$\begin{aligned}\dot{n}_A &= -\Gamma_+ n_A + \Gamma_- n_B, \\ \dot{n}_B &= \Gamma_+ n_A - \Gamma_- n_B.\end{aligned}\tag{2.2}$$

Γ_+ and Γ_- are the forward and backward rate constant, respectively. In order to relate the phenomenological equation to a specific physical situation, our goal is to express the constants Γ_+ and Γ_- in terms of ensemble averages of dynamical observables. The state of a system may be characterized by a generalized coordinate s , which is a function of the microscopic degrees of freedom. It is chosen to be positive in \mathcal{A} , zero on \mathcal{S} , and negative in \mathcal{B} . Hence, the Heavyside function $\theta(s)$ is the characteristic function of \mathcal{A} , being 1 for $s > 0$ and 0 for $s < 0$.

There are several ways to relate the rates to averages of dynamical variables. Simple and hence commonly considered situations are the (quasi-) stationary ones. For example, the rate of decay from the metastable region \mathcal{A} can be determined in a quasi-stationary non-equilibrium situation. Imagine that all the systems are prepared to be in thermal equilibrium but restricted to region \mathcal{A} at $t = 0$. After a short time $\sim t_s$ a quasi-stationary situation establishes [53–55], where the probability to find systems near a is approximately given by the equilibrium value and near b is ≈ 0 . On time scales $t_s \ll t \ll \Gamma_{+/-}^{-1}$, the decay rate is then given by

$$\Gamma_+ = \frac{I_s}{n_A},\tag{2.3}$$

where I_s is the total probability flux across a surface \mathcal{S} that separates the well (the metastable region) \mathcal{A} from its exterior.

Another possibility is to relate the rate to thermal equilibrium averages of dynamical observables. The fluctuation-dissipation theorem relates the dynamics of spontaneous fluctuations in equilibrium to the relaxation of a non-equilibrium state towards equilibrium. From Eq. (2.2) then follows that the equilibrium correlation function $\langle \delta\theta[s(0)]\delta\theta[s(t)] \rangle$ decays exponentially with time,

$$\langle \delta\theta[s(0)]\delta\theta[s(t)] \rangle \sim \exp[-(\Gamma_+ + \Gamma_-)t].\tag{2.4}$$

The time derivative of Eq. (2.4) normalized to $\langle \delta\theta[s(0)]^2 \rangle$ yields the so-called reactive flux. On intermediate time scales $t_s \ll t \ll \Gamma_{+/-}^{-1}$, the reactive flux is approximately proportional to the forward rate which then reads,

$$\Gamma_+ = \frac{\langle \delta[s(0)]\dot{s}(0)\theta[-s(t)] \rangle}{\langle \theta(s) \rangle}.\tag{2.5}$$

The rate Γ_+ is thus given by the flux $\delta[s(0)]\dot{s}(0)$ through $s = 0$ at time $t = 0$ averaged over all systems with $s(t) < 0$ that ended in state \mathcal{B} at time t .

In the following we discuss some properties of the forward rate Γ (we drop the index “+” from now on), and motivate crossover scenarios. We first concentrate on the classical case $T \gg T_0$, then we consider the regimes $T \gtrsim T_0$, and $T < T_0$.

2.1.1 Classical rate

In this section we derive the decay rate for multi-dimensional systems in the classical regime and discuss how crossovers occur. Following Langer’s derivation, we explicitly show that Kramers’ moderate-to-strong damping result for one-dimensional systems applies also for the multi-dimensional case if the unstable coordinate is decoupled. Starting from a generalized Langevin equation with memory friction, this has been shown by Grote and Hynes within the framework of the molecular rate method [56]. In the Markovian limit, the equivalent derivation beginning from a Fokker-Planck description is still lacking and given here. The importance of the result becomes clear since many authors starting from a Fokker-Planck equation unnecessarily restrict their analysis to the strong damping limit though the moderate damping regime can be treated without more effort.

We consider a $2N$ -dimensional phase space \mathcal{P} represented by position coordinates $\mathbf{x} = (x_0, \dots, x_{N-1})$ and conjugate momenta $\mathbf{p} = (p_0, \dots, p_{N-1})$. The generalized coordinate s is a function of phase space variables, $s(\mathbf{x}, \mathbf{p})$ with the property $s(\mathbf{x}, \mathbf{p}) = 0$ for $(\mathbf{x}, \mathbf{p}) \in \mathcal{S}$. The ensemble average of a dynamical variable $A(\mathbf{x}, \mathbf{p})$ is defined by

$$\langle A(t) \rangle = \frac{\int d^N x d^N p \rho(\mathbf{x}, \mathbf{p}, t) A(\mathbf{x}, \mathbf{p})}{\int d^N x d^N p \rho(\mathbf{x}, \mathbf{p}, t)}. \quad (2.6)$$

In the case of thermal equilibrium the canonical distribution normalized to one in the region \mathcal{A} is given by

$$\rho_0(\mathbf{x}, \mathbf{p}) = Z_A^{-1} \exp[-\beta H(\mathbf{x}, \mathbf{p})], \quad (2.7)$$

where $\beta = (k_B T)^{-1}$ is the inverse temperature, H the Hamiltonian, and Z_A is the partition sum for the states in the well,

$$Z_A = (2\pi\hbar)^{-N} \int_{(\mathbf{x}, \mathbf{p}) \in \mathcal{A}} d^N x d^N p \rho_0(\mathbf{x}, \mathbf{p}). \quad (2.8)$$

Transition state theory in one dimension

The simplest rate theory is the so-called transition state theory (TST) [57]. Let us consider the simplest case, $N = 1$. In TST two ad-hoc assumptions are made: first, thermal equilibrium prevails in the well \mathcal{A} . Second, a system will never return to \mathcal{A} once it has reached the barrier top at $s = 0$. The TST rate is thus given by the limit $t \rightarrow 0^+$ of Eq. (2.5). We choose \mathcal{S} by requiring $s = x_s - x$, where x_s is the barrier top of the potential

$V(x)$. Noting that $\lim_{t \rightarrow 0^+} \theta(x(t) - x_s) = \theta(p(0))$ and $\dot{x} = p/m_0$, where m_0 is the mass of the particle, we find

$$\Gamma_{TST} = (2\pi\hbar)^{-1} \int dp dx \rho_0(x, p) \delta(x - x_s) \theta(p) \frac{p}{m_0}. \quad (2.9)$$

Expanding $V(x)$ up to second order near the bottom of the well \mathcal{A} , $x = 0$, one obtains $Z_A \approx k_B T / \hbar \omega_a$, where $m_0 \omega_a^2 = V''(0)$ is the curvature of the potential at the minimum. Hence, the classical TST rate is given by

$$\Gamma_{TST} = \frac{\omega_a}{2\pi} \exp(-\beta V_s). \quad (2.10)$$

Spatial-diffusion-limited rate in arbitrary dimensions

We now derive the rate in the quasi-stationary case using the flux-over-population method given by Eq. (2.3). The total flux through \mathcal{S} is

$$I_s = (2\pi\hbar)^{-N} \int d^N x d^N p \delta(s) (\nabla_{x,p} s) \cdot \mathbf{J}, \quad (2.11)$$

where $\nabla_{x,p} = (\partial/\partial x_0, \dots, \partial/\partial x_{N-1}; \partial/\partial p_0, \dots, \partial/\partial p_{N-1})$ and $\mathbf{J}(\mathbf{x}, \mathbf{p}, t)$ is the probability current density at (\mathbf{x}, \mathbf{p}) in phase space. The population n_A in the well \mathcal{A} is

$$n_A = (2\pi\hbar)^{-N} \int d^N x d^N p \rho(\mathbf{x}, \mathbf{p}, t) \theta[s(\mathbf{x}, \mathbf{p})]. \quad (2.12)$$

In order to calculate the classical rate Γ_{cl} , one is generally confronted with the problem to solve the dynamical equations governing the time-dependent evolution of ρ and \mathbf{J} within the metastable region.

Matters simplify considerably in the quasi-stationary case, where $\dot{\rho} \approx 0$. A stationary probability flow through \mathcal{S} requires sources in the metastable region \mathcal{A} and sinks in \mathcal{B} . A stationary state is reached, when the production rate of the sources is equal to the destruction rate of the sinks. In other words, whenever a system has decayed, it is removed from the ensemble and replaced by a new metastable one. If on average the systems stay in the metastable state \mathcal{A} for a long time, the stationary distribution $\rho(\mathbf{x}, \mathbf{p})$ is close to the equilibrium distribution and can be parameterized by

$$\rho(\mathbf{x}, \mathbf{p}) = \sigma(\mathbf{x}, \mathbf{p}) \rho_0(\mathbf{x}, \mathbf{p}), \quad (2.13)$$

where $\sigma(\mathbf{x}, \mathbf{p})$ takes into account the non-equilibrium effects.

In general, the correction function σ has to be determined from the equation of motion for ρ . Kramers' treatment for a Brownian particle in one dimension diffusing over a parabolic barrier [54] was generalized to higher dimensions, $N > 1$, by Langer [15]. The domain of attraction \mathcal{A} is separated by a saddle point from lower lying minima of the potential. The Langevin equation can be conveniently written as a matrix equation for phase space vectors,

$$\begin{pmatrix} \dot{\mathbf{x}} \\ \dot{\mathbf{p}} \end{pmatrix} = -\mathbf{M} [\nabla_{x,p} H(\mathbf{x}, \mathbf{p}) - \mathbf{f}]. \quad (2.14)$$

The fluctuating forces $\mathbf{f} = (f_0, \dots, f_{N-1}; 0, \dots, 0)$ are characterized by the ensemble averages

$$\langle f_n \rangle = 0, \quad \langle f_m(t) f_n(t') \rangle = 2m_n \gamma_n k_B T \delta_{m,n} \delta(t - t'), \quad (2.15)$$

where $m, n < N$, m_n are the masses, and γ_n are the friction coefficients.

The matrix \mathbf{M} can be expressed as a sum of a symplectic matrix \mathbf{A} describing the Hamiltonian dynamics of the system in absence of dissipation and a symmetric matrix \mathbf{D} modeling dissipation,

$$\mathbf{M} = \begin{pmatrix} \mathbf{0} & -\mathbf{I} \\ \mathbf{I} & \mathbf{D} \end{pmatrix}, \quad (2.16)$$

where $\mathbf{I} = \text{diag}(1, \dots, 1)$ is the $N \times N$ unity matrix and the dissipative part is given by $\mathbf{D} = \text{diag}(m_0 \gamma_0, \dots, m_{N-1} \gamma_{N-1})$. Note that \mathbf{D} has dimensions of mass per unit time. A matrix with mixed units may look a bit awkward at first sight. Here, however, the matrix \mathbf{M} is simply understood as an object to introduce a compact notation. The Hamiltonian is given by

$$H = \sum_{n=0}^{N-1} \frac{p_n^2}{2m_n} + V(\mathbf{x}). \quad (2.17)$$

Close to the saddle point $\mathbf{x}_s, \mathbf{p}_s$, where sinks and sources are assumed to be absent, the Klein-Kramers equation for ρ reads

$$\partial_t \rho + \nabla_{x,p} \mathbf{J} = 0 \quad (2.18)$$

with

$$\mathbf{J} = -\mathbf{M}[(\nabla_{x,p} H) + k_B T \nabla_{x,p}] \rho. \quad (2.19)$$

The following assumptions are made: Since we consider metastability in the moderate-to-strong damping regime the particle nearly thermalizes in the well and near the local minimum at $(\mathbf{x}, \mathbf{p}) = (\mathbf{0}, \mathbf{0})$ the density function is close to the equilibrium one, $\rho(\mathbf{x}, \mathbf{p}) \approx \rho_0(\mathbf{x}, \mathbf{p})$. Hence, $\sigma(\mathbf{0}, \mathbf{0}) \approx 1$. Far beyond the saddle, particles are absorbed by sinks, $\rho(\mathbf{x}, \mathbf{p}) \approx 0$ implying that $\sigma(\mathbf{x}, \mathbf{p}) \approx 0$. Making the ansatz $\rho = \sigma \rho_0$ the equation of motion for the stationary σ reads

$$[(\nabla_{x,p} H) - k_B T \nabla_{x,p}] \mathbf{M} \nabla_{x,p} \sigma = 0. \quad (2.20)$$

Near the extrema, we approximate the potential by quadratic forms,

$$V(\mathbf{x}) \approx \frac{1}{2} \mathbf{x}^T \mathbf{V}_a \mathbf{x} \quad \text{for } \mathbf{x} \approx \mathbf{0}, \quad V(\mathbf{x}) \approx V_s + \frac{1}{2} \mathbf{x}^T \mathbf{V}_s \mathbf{x} \quad \text{for } \mathbf{x} \approx \mathbf{x}_s. \quad (2.21)$$

Accordingly, we approximate the Hamiltonian close to the minimum of the well $(\mathbf{x}, \mathbf{p}) = (\mathbf{0}, \mathbf{0})$ by

$$H(\mathbf{x}, \mathbf{p}) \approx \frac{1}{2} (\mathbf{x}, \mathbf{p}) \mathbf{E}_a \begin{pmatrix} \mathbf{x} \\ \mathbf{p} \end{pmatrix}, \quad (2.22)$$

and close to the saddle point $(\mathbf{x}_s, \mathbf{0})$ as

$$H(\mathbf{x}, \mathbf{p}) = V_s - \frac{1}{2} \mathbf{y}^T \mathbf{E}_s \mathbf{y} \quad (2.23)$$

Here we have introduced $V_s = H(\mathbf{x}_s, \mathbf{0})$, $\mathbf{y} = (\mathbf{x} - \mathbf{x}_s, \mathbf{p})$, and the transposed \mathbf{y}^T of \mathbf{y} . With a quadratic Hamiltonian Eq. (2.20) becomes linear,

$$\left[\mathbf{y}^T \mathbf{E}_s + k_B T \nabla_{x,p} \right] \mathbf{M} \nabla_{x,p} \sigma = 0. \quad (2.24)$$

Substituting the ansatz $\sigma(\mathbf{x}, \mathbf{p}) = g[u(\mathbf{x}, \mathbf{p})]$, into Eq. (2.24), where $u(\mathbf{x}, \mathbf{p}) = \mathbf{u} \cdot \mathbf{y}$ is a linear combination of coordinates and momenta, one obtains an ordinary differential equation for g ,

$$(\mathbf{y}^T \mathbf{E}_s \mathbf{M} \mathbf{u}) g'(u) + k_B T (\mathbf{u}^T \mathbf{M} \mathbf{u}) g''(u) = 0, \quad (2.25)$$

if the coefficient of g' is a function of u , that is $\mathbf{y}^T \mathbf{E}_s \mathbf{M} \mathbf{u} \propto u$. This constraint provides an eigenvalue equation for \mathbf{u} ,

$$-\mathbf{E}_s \mathbf{M} \mathbf{u} = \lambda \mathbf{u}, \quad (2.26)$$

which has a unique positive solution λ . One can normalize \mathbf{u} such that $\mathbf{u}^T \mathbf{E}_s^{-1} \mathbf{u} = -1$ and $\lambda = \mathbf{u}^T \mathbf{M} \mathbf{u}$. The solution of the resulting equation $u g'(u) + k_B T g''(u) = 0$ satisfying the boundary conditions for ρ is then given by

$$g(u) = (2\pi k_B T)^{-1/2} \int_u^\infty dx \exp\left(-\frac{\beta x^2}{2}\right). \quad (2.27)$$

Substituting $\sigma(\mathbf{x}, \mathbf{p}) = g[u(\mathbf{x}, \mathbf{p})]$ into Eq. (2.19), we obtain the probability current

$$\mathbf{J} = \sqrt{\frac{k_B T}{2\pi}} \rho_0 \exp\left(-\frac{\beta u^2}{2}\right) \mathbf{M} \mathbf{u}. \quad (2.28)$$

Inserting \mathbf{J} into Eq. (2.11), choosing the dividing surface $s(\mathbf{x}, \mathbf{p}) \propto u(\mathbf{x}, \mathbf{p})$ and performing the integrals, one finds that the flux I_s is given by

$$I_s = \frac{\lambda}{2\pi} \left[\det\left(\frac{\hbar}{k_B T} \mathbf{E}_s\right) \right]^{-1/2} Z_A^{-1} \exp(-\beta V_s). \quad (2.29)$$

Eq. (2.12) with the approximate Hamiltonian given by Eq. (2.22) yields the population n in the well,

$$n = Z_A^{-1} \left[\det\left(\frac{\hbar}{k_B T} \mathbf{E}_a\right) \right]^{-1/2}. \quad (2.30)$$

Hence, the classical rate $\Gamma_{\text{cl}} = I/n$ is given by

$$\Gamma_{\text{cl}} = \frac{\lambda}{2\pi} \left\{ \frac{\det[\mathbf{E}_a]}{|\det[\mathbf{E}_s]|} \right\}^{1/2} \exp(-\beta V_s) = \frac{\lambda}{2\pi} \left\{ \frac{\det[\mathbf{V}_a]}{|\det[\mathbf{V}_s]|} \right\}^{1/2} \exp(-\beta V_s). \quad (2.31)$$

The rate has now the desired Arrhenius form as in Eq. (2.1) with the pre-exponential factor $P = \lambda \sqrt{\det[\mathbf{V}_a]/|\det[\mathbf{V}_s]|}/(2\pi)$ and the strength of the barrier $A = \beta V_s$.

Langer defined the free energy of a metastable state in the following way [13]. Deform a potential with a global minimum such that the minimum becomes a local one. The corresponding analytical continuation of the free energy, which is well defined for the stable potential, becomes complex for the metastable situation. The imaginary part evaluated in steepest descent approximation reads

$$\text{Im}\mathcal{F} = \frac{k_B T}{2} \left\{ \frac{\det[\mathbf{V}_a]}{|\det[\mathbf{V}_s]|} \right\}^{1/2} \exp(-\beta V_s). \quad (2.32)$$

Analogous to the definition of life times of resonant states in quantum mechanics, he conjectured that the imaginary part of the free energy should be proportional to the decay rate of the metastable state [13]. The proportionality constant is given by Eq. (2.31),

$$\Gamma_{\text{cl}} = \frac{\lambda}{\pi k_B T} \text{Im}\mathcal{F}. \quad (2.33)$$

All one is left with is the determination of the positive eigenvalue λ in Eq. (2.26), which can be done exactly only in special cases. It is interesting to note that Langer applied his quite general theory valid in the moderate-to-strong-damping regime only to the overdamped limit $\gamma \gg \omega_s$ with symmetric friction, $\gamma_n = \gamma$, where the solution of Eq. (2.26) becomes trivial. In the last thirty years, many authors who applied his result, restricted their analysis to the overdamped case being unaware of the fact that the moderate friction regime can be treated without much more effort [1]. Though Grote and Hynes [58] were aware that it should in principle be possible to derive the multidimensional rate for moderate damping starting from a Fokker-Planck description¹, they did not explicitly show how, and even in the most recent literature unnecessary restrictions are made [59].

Let us now calculate λ for the specific case they discussed, namely a system with a decoupled unstable mode x_0 . First, we rederive Kramers' [54] celebrated result for $N = 1$. Then we show how to obtain λ in the multidimensional case that Grote and Hynes considered, namely a Hamiltonian with a decoupled unstable mode x_0 .

Kramers studied a Brownian particle in one dimension $N = 1$ interacting with a potential $V(x_0)$ [54] obeying the Langevin equation (2.14) with a Hamiltonian $H = p_0^2/2m_0 + V(x_0)$, a white noise fluctuating force $\mathbf{f} = (f_0, 0)$, and a dynamical matrix

$$\mathbf{M} = \begin{pmatrix} 0 & -1 \\ 1 & \gamma_0 m_0 \end{pmatrix}. \quad (2.34)$$

¹Grote and Hynes derived a multi-dimensional rate for the case of memory friction starting from a generalized Langevin equation. Discussing the Markovian limit of their result, they mention in Ref. [58] : "Since the ordinary LE [Langevin equation] is strictly equivalent to a Fokker-Planck probability description Eq. (3.21) [their result] must also be the prediction of an uncoupled mode FP [Fokker-Planck] treatment. Indeed, while Eq. (3.21) is new, it is hardly a surprise since its diffusive limit Eq. (3.20) [overdamped limit] has been derived a number of times as a multidimensional generalization of a well-known result of Kramers."

Here, γ_0 is the friction coefficient and m_0 the mass of the particle. With $\omega_a^2 = V''(0)/m_0$ and $\omega_s^2 = -V''(x_s)/m_0$, the matrices appearing in Eqs. (2.22) and (2.23) read $\mathbf{E}_a = \text{diag}(m_0\omega_a^2, m_0^{-1})$ and $\mathbf{E}_s = \text{diag}(-m_0\omega_s^2, m_0^{-1})$, respectively. The positive eigenvalue λ of $-\mathbf{E}_s\mathbf{M}$ is

$$\lambda = \sqrt{1 + \frac{\gamma_0^2}{4}} - \frac{\gamma_0}{2}. \quad (2.35)$$

We denote the associated eigenvector (v_1, v_{N+1}) . Hence, Kramers' rate is

$$\Gamma_K = \varrho \Gamma_{TST}, \quad (2.36)$$

where $\varrho = \lambda/\omega_s$ is the transmission factor. Comparing Γ_K with Γ_{TST} , one notices that the latter overestimates the true rate since in TST one neglects that particles might re-cross the barrier. Note that the spatial-diffusion-limited approach presented here breaks down in the underdamped regime, where the particle does not have enough time to approach local thermal equilibrium. In the strong damping limit, $\gamma \gg \omega_s$, the rate can readily be calculated to yield $\varrho = \omega_s/\gamma$, which is consistent with the rate that one obtains starting with the Smoluchowski equation.

In the multidimensional case with a decoupled unstable mode x_0 , the Hamiltonian is given by

$$H = \sum_{n=0}^{N-1} \frac{p_n^2}{2m_n} - \frac{m\omega_0^2 x_0^2}{2} + \tilde{V}(x_1, \dots, x_{N-1}). \quad (2.37)$$

The eigenvalue problem for λ reads

$$-\mathbf{E}_s\mathbf{M}\mathbf{u} = \begin{pmatrix} & -m_0\omega_s^2 & & \\ \mathbf{0} & & \ddots & \\ m_0^{-1} & & \gamma_0 & \\ & \ddots & & \ddots \end{pmatrix} \begin{pmatrix} u_1 \\ \vdots \\ u_{N+1} \\ \vdots \end{pmatrix} = \lambda\mathbf{u}. \quad (2.38)$$

For a single unstable mode the matrix $-\mathbf{E}_s\mathbf{M}$ has only one positive eigenvalue λ . Instead of calculating the entire spectrum, we only have to determine the positive eigenvalue. Comparing with the one-dimensional case, we see that $\mathbf{u} = (v_1, 0, \dots, 0, v_{N+1}, 0, \dots, 0)$ is an eigenvector with a positive eigenvalue λ given by Eq. (2.35). Thus, we have shown that for a system with a decoupled unstable mode x_0 the moderate-to-strong-damping rate reads

$$\Gamma_{\text{cl}} = \frac{\varrho\omega_s}{2\pi} \left\{ \frac{\det[\mathbf{V}_a]}{|\det[\mathbf{V}_s]|} \right\}^{1/2} \exp(-\beta V_s). \quad (2.39)$$

In the overdamped limit, $\gamma \gg \omega_s$, the transmission factor reduces to $\varrho = \omega_s/\gamma$.

Transition state theory for system-plus-reservoir models

The results found with the flux-over-population method can also be derived within the equilibrium reactive flux equation, which we consider in this section. One aim is to show

that the equilibrium treatment yields equivalent results, the other is to introduce the concept of the system-plus-reservoir model [60] in order to take into account dissipation, which we need later when we treat the quantum regime [3–5].

We start with a Hamiltonian describing a system interacting with a heat bath,

$$H = H_s(\mathbf{x}, \mathbf{p}) + \sum_{n=0}^{N-1} H_b(\mathbf{X}_n, \mathbf{P}_n; x_n). \quad (2.40)$$

The system consists of N degrees of freedom with masses m_n , represented by the coordinates $\mathbf{x} = (x_0, \dots, x_{N-1})$ and the momenta $\mathbf{p} = (p_0, \dots, p_{N-1})$ with the bare Hamiltonian

$$H_s(\mathbf{x}, \mathbf{p}) = \sum_{n=0}^{N-1} \frac{p_n^2}{2m_n} + V(\mathbf{x}). \quad (2.41)$$

Without loss of generality we choose the coordinate system such that the curvature matrix of the potential evaluated at the saddle point, \mathbf{V}_s as defined in Eq. (2.21), is diagonal. Each of the degrees of freedom is coupled bilinearly to a bath of M harmonic oscillators with identical spectrum,

$$H_b(\mathbf{X}_n, \mathbf{P}_n; x_n) = \frac{1}{2} \sum_{j=0}^{M-1} \left\{ \frac{P_{n,j}^2}{M_j} + M_j \Omega_j^2 \left[X_{n,j} + \frac{C_j}{M_j \Omega_j^2} x_n \right]^2 \right\}, \quad (2.42)$$

where $\mathbf{X}_n = (X_{n,0}, \dots, X_{n,M-1})$ and $\mathbf{P}_n = (P_{n,0}, \dots, P_{n,M-1})$ are the coordinates and momenta of the harmonic oscillator bath coupled to the n -th degree of freedom, respectively. C_j are the coupling constants between a degree of freedom and the associated bath. Starting with the Hamilton equations and integrating out the bath variables, one finds the generalized Langevin equations [60],

$$m_n \ddot{x}_n + \frac{\partial}{\partial x_n} V(\mathbf{x}) + m_n \int_0^t dt' \gamma_n(t-t') \dot{x}_n(t') = f_n(t). \quad (2.43)$$

Assuming that the total system is initially prepared in thermal equilibrium, the forces $\mathbf{f} = (f_0, \dots, f_{N-1})$ become a stationary Gaussian noise of vanishing mean,

$$f_n(t) = - \sum_{j=0}^{M-1} C_j \left\{ \left[X_{n,j}(0) + \frac{C_j}{M_j \Omega_j^2} x_n(0) \right] \cos(\Omega_j t) + \frac{\dot{X}_{n,j}(0)}{\Omega_j} \sin(\Omega_j t) \right\}, \quad (2.44)$$

obeying the fluctuation-dissipation theorem,

$$\langle f_n(t) f_m(t') \rangle = k_B T m_n \delta_{n,m} \gamma_n(t-t'). \quad (2.45)$$

The friction kernels $\gamma_n(t)$ read

$$\gamma_n(t) = \frac{1}{m_n} \sum_{j=0}^{M-1} \frac{C_j}{M_j \Omega_j^2} \cos(\Omega_j t). \quad (2.46)$$

With finite M these are quasi-periodic functions in time. A phenomenologically decaying memory friction, where $\gamma_n(t) \rightarrow 0$ as $t \rightarrow \infty$, can be modeled by a suitable choice of bath parameters in equation (2.42) followed by performing a continuum limit for the distribution of frequencies which densely extends down to zero frequencies.

If the frequency spectrum of the bath is Debye-like and the momentum varies slowly over time scales of the order of the inverse Debye frequency, the Langevin equation becomes Markovian.

We have seen in the preceding paragraph that a metastable system with Langevin dynamics has a decay rate that takes into account friction and that particles may return to the well once they have crossed the barrier. Multidimensional TST applied to the system-plus-reservoir model discussed here provides the same result [56]. Near the saddle point \mathbf{x}_s , the total Hamiltonian can be approximated by a quadratic one, see Eq. (2.21). The curvature matrix of H can be partly diagonalized by transforming the system and bath coordinates for $n = 0$ to normal ones, $(x_0, \mathbf{x}_0) \rightarrow (\tilde{x}_0, \tilde{\mathbf{x}}_0)$. The effective frequency ω_R of the unstable mode \tilde{x}_0 ,

$$\omega_R^2 + \omega_R \hat{\gamma}_0(\omega_R) = \omega_s^2, \quad (2.47)$$

is reduced compared to the bare barrier frequency ω_s of x_0 . Here $\hat{\gamma}_0$ is the Laplace transform of γ_0 . Since in the quadratic approximation \tilde{x}_0 is decoupled from the rest of the degrees of freedom, its energy E_0 can be separated from the total (conserved) energy, $E = E_0 + E_{n \neq 0}$. Noting that the system decays as soon as the energy E_0 of the unstable mode is larger than the barrier energy V_s , the rate can be rewritten in energy-phase space as

$$\Gamma_{\text{cl}} = \int_{V_s}^{\infty} dE_0 w(E_0). \quad (2.48)$$

where $dE_0 w(E_0)$ is the probability per unit time that the unstable mode has an energy in the interval $[E_0, E_0 + dE_0]$,

$$w(E_0) = \int \frac{d^{NM} x d^{NM} p}{(2\pi\hbar)^{NM}} \delta[E_0 - H_0(\tilde{x}_0, \tilde{p}_0)] \rho(\{x_n, p_n; \mathbf{X}_n, \mathbf{P}_n\})$$

with $H_0 = \tilde{p}_0^2/(2m_0) + V_s - m_0\omega_R^2\tilde{x}_0^2/2$. In TST, the density function in the well is approximated by the equilibrium one, $\rho \approx \rho_0$ and

$$w(E_0) \approx w_0(E_0) = \frac{\beta\omega_R}{2\pi} \left\{ \frac{\det[\mathbf{E}_a]}{|\det[\mathbf{E}_s]|} \right\}^{1/2} \exp(-\beta E_0). \quad (2.49)$$

Substituting Eq. (2.49) into Eq. (2.48) we find

$$\Gamma_{\text{cl}} = \frac{\omega_R}{2\pi} \left\{ \frac{\det[\mathbf{V}_a]}{|\det[\mathbf{V}_s]|} \right\}^{1/2} \exp(-\beta V_s). \quad (2.50)$$

In the absence of memory effects, $\gamma_0(t) = 2\gamma\delta(t)$, the frequency of the unstable mode reduces to $\omega_R = \omega_s$ and Eq. (2.50) becomes identical to Eq. (2.39). This result is regarded as a cornerstone in rate theory: Langers spatial-diffusion-limited formula and the TST rate for a system coupled linearly to a bath of harmonic oscillators yield the same result.

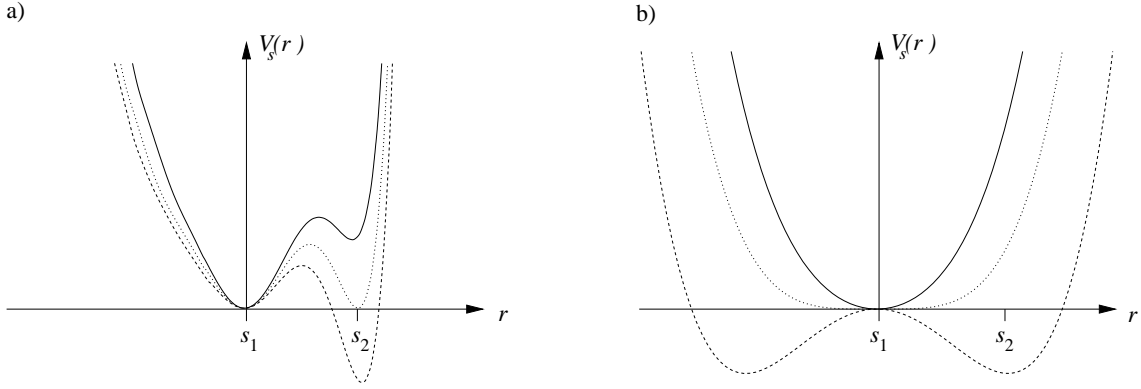


Figure 2.2: Saddle points V_s of the potential energy V parameterized by the distance r from the saddle s_1 along the dividing surface \mathcal{S} . (a) A first order crossover occurs, if a competing saddle s_2 becomes the lowest one upon tuning an external parameter causing a discontinuous crossover from $\Gamma_{\text{cl}} \approx \Gamma_{s_1}$ to $\Gamma_{\text{cl}} \approx \Gamma_{s_2}$. (b) A stable mode of V at s_1 becomes unstable upon varying the external parameter leading to a saddle-point bifurcation $s_1 \rightarrow s_2$. The saddle point s_2 develops continuously leading to a smooth second-order crossover $\Gamma_{\text{cl}} \approx \Gamma_{s_1} \rightarrow \Gamma_{\text{cl}} \approx \Gamma_{s_2}$

Crossovers in the classical decay rate

So far we discussed the classical decay rate for a metastable system with a single saddle point. In general there might be the possibility that the escape occurs via several saddles. The escape probability is given by the sum of probabilities over all probable escape paths. If the saddle nodes are fairly well separated, the total escape rate is approximately the sum of all saddle-point contributions Γ_{s_j} ,

$$\Gamma_{\text{cl}} \approx \sum_j \Gamma_{s_j} \quad (2.51)$$

If there is a saddle point s_1 with a barrier energy V_{s_1} several orders of $k_B T$ smaller than the barriers $V_{s_{j \neq 1}}$ of the other saddles, it will give the largest contribution to the rate, whereas the contributions of the higher lying saddles are exponentially suppressed,

$$\Gamma_{\text{cl}} \approx \Gamma_{s_1}. \quad (2.52)$$

Let us now consider the case where the potential energy landscape changes its shape upon varying an external parameter. In the simplest case, the height of the lowest lying barrier V_{s_1} is altered and the rate is a simple function of the external parameter. A crossover to a regime with a different decay behavior occurs, if upon turning the external parameter a new saddle point s_m with barrier V_{s_m} becomes the lowest one. This is due to the fact that now the rate achieves the strongest contribution from the saddle s_m and in general V_{s_m} varies differently than V_{s_1} if the parameter is tuned.

In Fig. 2.2 cross sections of potential landscapes along the dividing surface \mathcal{S} are shown, which we have chosen such that all saddles are lying on \mathcal{S} . The coordinate r denotes the distance to the saddle point s_1 and parameterizes the potential energy, $V_s(r) = V[\mathbf{x}(r)]$ with $\mathbf{x}(r) \in \mathcal{S}$. The initial potential is represented by the solid line, the crossover potential by the dotted line and the final one by the dashed line. Initially s_1 is the energetically lowest lying saddle and after the crossover has occurred, s_2 has the smallest energy barrier.

The potential evolution shown in Fig. 2.2a leads to a discontinuous crossover from $\Gamma_{\text{cl}} \sim \exp(-\beta V_{s_1})$ to $\Gamma_{\text{cl}} \sim \exp(-\beta V_{s_2})$. The situation is analogous to the development of the Landau free energy of a system undergoing a first-order phase transition and is hence called first-order crossover.

Fig. 2.2b depicts a second-order crossover. Here, the lowest saddle point s_1 is deformed into two lower lying ones s_2 and the barrier V_{s_1} is smoothly changing to V_{s_2} . Consequently, the crossover from $\Gamma_{\text{cl}} \sim \exp(-\beta V_{s_1})$ to $\Gamma \sim \exp(-\beta V_{s_2})$ is continuous. Note that before splitting, the saddle point s_1 has only one unstable direction. After the saddle-point bifurcation one of the stable modes of s_1 has become unstable. Hence, one of the eigenvalues of the curvature matrix \mathbf{V}_{s_1} , which is positive before the saddle-point splitting, vanishes at the crossover and becomes negative after the bifurcation. Clearly, at the crossover itself and within a narrow regime around it, the Gaussian approximation that has been made to obtain Eqs. (2.39) and (2.50) breaks down. However, the divergencies can be cut off by taking higher order terms than quadratic ones into account in the approximation for the potential.

2.1.2 Quantum rate

The quantum version of the reactive-flux equation (2.5) reads [61, 62]

$$\Gamma_{\text{qu}} = \frac{\text{Re} \left[\text{Tr} \left(\hat{\rho}_0 \hat{F}_{\mathcal{S}} \hat{\mathcal{P}}_p \right) \right]}{\text{Tr} \left(\hat{\rho}_0 \hat{\mathcal{P}}_{\mathcal{A}} \right)} \quad (2.53)$$

where $\hat{\rho}_0$ is the equilibrium density operator, $\hat{\mathcal{P}}_p$ projects onto states that are scattered from \mathcal{A} to \mathcal{B} , $\hat{\mathcal{P}}_{\mathcal{A}}$ is the projector onto metastable states in \mathcal{A} , and

$$\hat{F}_{\mathcal{S}} = \frac{1}{m} \nabla_x s(\hat{\mathbf{x}}) \delta[s(\hat{\mathbf{x}})] \hat{\mathbf{p}} \quad (2.54)$$

is the flux-through-surface operator. The dividing surface \mathcal{S} is defined by $\langle \mathbf{x}_{\mathcal{S}} | s(\hat{\mathbf{x}}) | \mathbf{x}_{\mathcal{S}} \rangle = 0$ and $\hat{\mathbf{x}} | \mathbf{x}_{\mathcal{S}} \rangle = \mathbf{x}_{\mathcal{S}} | \mathbf{x}_{\mathcal{S}} \rangle$ with $\mathbf{x}_{\mathcal{S}} \in \mathcal{S}$. The dividing surface \mathcal{S} is smooth. Introducing the resolvent operator $\hat{G}^+(E) = (E - \hat{H} + i0^+)^{-1}$, Eq. (2.53) can be brought into the form

$$\Gamma_{\text{qu}} = (2\pi\hbar) Z_{\mathcal{A}}^{-1} \int_0^\infty dE p(E) e^{-\beta E}. \quad (2.55)$$

with $p(E)$ being the micro canonical decay probability at total energy E [62],

$$p(E) = 2\hbar \text{Im} \left\{ \text{Tr} \left[\hat{G}^+(E) \hat{F}_{\mathcal{S}} \hat{\mathcal{P}}_p \right] \right\}. \quad (2.56)$$

If we choose our coordinate system such that x_0 is the coordinate of the unstable direction and take the flat surface $s(\hat{\mathbf{x}}) = \hat{x}_0 - x_{s,0}$, where $x_{s,0}$ is the saddle-point coordinate in the unstable direction, the projection operator $\hat{\mathcal{P}}_p$ reads

$$\hat{\mathcal{P}}_p = \lim_{t \rightarrow \infty} e^{\frac{i}{\hbar} \hat{H} t} \theta(\hat{p}_0) e^{-\frac{i}{\hbar} \hat{H} t} = \lim_{t \rightarrow \infty} e^{\frac{i}{\hbar} \hat{H} t} \theta(\hat{x}_0 - x_{s,0}) e^{-\frac{i}{\hbar} \hat{H} t}. \quad (2.57)$$

It projects onto outgoing states that have positive momentum or are in \mathcal{B} in the infinite future selecting the decay events.

Quantum transition state theory

The quantum transition state theory (QTST) limit of Eq. (2.53) is then found by replacing $\mathcal{P}_p \rightarrow \theta(\hat{p}_0)$. For the above chosen surface we have $\hat{F}_S = \delta(\hat{x}_0 - x_{s,0}) \hat{p}_0 / m$. With $\hat{p}_0 \theta(\hat{p}_0) = (|\hat{p}_0| + \hat{p}_0)/2$ one obtains [62]

$$p(E) = \frac{\hbar}{m} \int d\mathbf{x} \delta(x_0 - x_{s,0}) \langle \mathbf{x} | \hat{G}^+(E) | \hat{p}_0 | | \mathbf{x} \rangle. \quad (2.58)$$

This expression can be evaluated in the semiclassical limit using Gutzwiller's trace formula [63],

$$p(E) = \sum_{n=1}^{\infty} (-1)^{n-1} \exp \left[-\frac{n\Phi(E)}{\hbar} \right] \prod_{m=1}^N \left\{ 2 \sinh \left[\frac{1}{2} n T(E) \omega_m(E) \right] \right\}^{-1}, \quad (2.59)$$

where

$$\Phi(E) = \int_0^{T(E)} d\tau \mathbf{p}(\tau) \mathbf{x}(\tau) \quad (2.60)$$

denotes the abbreviated action integral along the periodic orbit in imaginary time $t = -i\tau$ of period $T(E)$ that passes through \mathcal{S} . The sum over n takes into account multiple traversals of the periodic orbit. The parameters $\omega_m(E)$ denote the dynamical stability frequencies of the periodic orbit at energy E . Expanding the sinh functions, introducing the energy

$$E_0 = E - \sum_{n=1}^N \hbar \omega_n(E_0) \quad (2.61)$$

left in the unstable mode while traversing the saddle point, and approximating the potential landscape locally by a parabolic one, Hänggi and Hontscha [64] found

$$p(E) = \sum_{n_0, \dots, n_{N-1}=0}^{\infty} \{1 - \exp[\Phi(E_0)]\}^{-1}. \quad (2.62)$$

Hence the calculation of $p(E)$ reduces to an evaluation of $\Phi(E_0)$. For $T > T_0$ one finds

$$\Gamma_{\text{qu}} = \frac{\omega_a}{2\pi} \frac{\sinh(\hbar\beta\omega_0^a/2)}{\sinh(\hbar\beta\omega_0^s/2)} \prod_{n=1}^N \frac{\sinh(\hbar\beta\omega_n^a/2)}{\sinh(\hbar\beta\omega_n^s/2)} \exp(-V_s/k_B T), \quad (2.63)$$

where ω_n^a and ω_n^s are the dynamical stability frequencies evaluated at the minimum and the saddle point, respectively.

Below the crossover temperature, $T < T_0$, Eq. (2.59) is dominated by the $n = 1$ term. The abbreviated action $\Phi(E)$ can be evaluated by the method of steepest descent. In this approximation, only the extremal orbit with the period $T(E = E_B) = \hbar\beta$ and quadratic fluctuations around it are taken into account. The saddle-point trajectory \mathbf{x}_B , known as bounce solution, yields the extremal Euclidean action

$$S_B = S_E[\mathbf{x}_B] = \hbar\beta E_B + \Phi(E_B) = \int_0^{2\pi} d\tau \left\{ V[\mathbf{x}_B(\tau)] + \frac{1}{2} \mathbf{p}_B(\tau) \dot{\mathbf{x}}_B(\tau) \right\}. \quad (2.64)$$

The rate in the quantum regime then reads

$$\Gamma_{\text{qu}} = Z_A^{-1} |2\pi\hbar T'(E_B)|^{-1/2} \prod_{m=1}^N \left\{ 2 \sinh \left[\frac{1}{2} T(E_B) \omega_m(E_B) \right] \right\}^{-1} \exp(-S_B/\hbar). \quad (2.65)$$

The pre-exponential factor can be related to the eigenvalue spectrum of the second functional derivative of the Euclidean action at the bottom of the well and the saddle point, respectively,

$$\Gamma_{\text{qu}} = \left\{ \frac{m}{2\pi\hbar} \int_0^{\hbar\beta} d\tau [\dot{\mathbf{x}}_B(\tau)]^2 \right\}^{1/2} \left[\frac{\det(\delta^2 S_E / \delta \mathbf{x}^2)_{\mathbf{x}=\mathbf{x}_a}}{|\det'(\delta^2 S_E / \delta \mathbf{x}^2)_{\mathbf{x}=\mathbf{x}_B(\tau)}|} \right]^{1/2} \exp(-S_B/\hbar), \quad (2.66)$$

where \det' means that the zero eigenvalue has to be omitted. Finally, the rate can be written in the compact form

$$\Gamma_{\text{qu}} = \frac{2}{\hbar} \text{Im} \mathcal{F}, \quad (2.67)$$

where the equilibrium free energy is given by

$$\exp(-\beta \mathcal{F}) = \int \mathcal{D}\mathbf{x}(\tau) \exp(-S_E[\mathbf{x}, \dot{\mathbf{x}}]/\hbar). \quad (2.68)$$

Crossovers in the quantum decay rate

In the quantum regime, the extremal of the action S_B plays the same role as the saddle point of the potential energy V_s in the classical regime. In fact, in the high temperature limit, $T \gg T_0$, the bounce action converges to $S_B \rightarrow \hbar V_s / k_B T$.

Analogous to the classical case, one defines first-order and second-order crossovers in the quantum regime. Crossovers occur, if a new saddle point of the Euclidean action becomes the lowest one. A first-order crossover is due to a change of the relevant saddle causing a discontinuity of the rate as a function of an external parameter (see Fig. 2.2, but replace $r \rightarrow \zeta$ and $V_s(r) \rightarrow S_E(\zeta)$.) If at the saddle a stable mode of the action becomes unstable upon tuning an external parameter, the saddle point of the action bifurcates. This leads to a second-order or continuous crossover from one decay regime to the other.

2.2 Model

2.2.1 Euclidean action

Let us consider a system of N degrees of freedom with a Euclidean action

$$S_E = \int_0^{\hbar\beta} d\tau [K(\mathbf{x}) + E(\mathbf{x}) + D(\mathbf{x})], \quad (2.69)$$

where τ is the imaginary time, $\mathbf{x} = (x_0, \dots, x_{N-1})$ represents the coordinates of the degrees of freedom, E is the potential energy, and D models the dissipation. The “kinetic” energy is given by

$$K(\mathbf{x}) = \frac{m_0}{2} \sum_{n=0}^{N-1} \left(\frac{\partial x_n}{\partial \tau} \right)^2,$$

where m_0 corresponds to the mass of an individual particle. Each of the particles experiences a single-particle potential $U(x_n)$, and interacts with the others via spring-like nearest-neighbor interactions,

$$E(\mathbf{x}) = \frac{\kappa}{2} \sum_{n=1}^{N-1} (x_n - x_{n-1})^2 + \sum_{n=0}^{N-1} U(x_n), \quad (2.70)$$

where κ is the spring constant. We assume that all the particles are initially situated near a local minimum of the potential U . The coordinates x_n measure the distance of each particle n from the minimum at $x_n = 0$. Close to $x_n = 0$, the single-particle potential can be approximated by a cubic parabola,

$$U(x_n) = U_B \left[3\Delta \left(\frac{x_n}{r} \right)^2 - 2 \left(\frac{x_n}{r} \right)^3 \right]. \quad (2.71)$$

Here $\Delta \ll 1$ is a tunable parameter. The constants U_B and r are the characteristic energy and length scales, respectively. At $x_n = r\Delta$ the single-particle potential has a maximum. The energy difference between the local minimum and the maximum is $\tilde{U}_B = U(r\Delta) = U_B\Delta^3$. Dissipation is modelled by coupling each particle to a bath of harmonic oscillators as introduced in Sec. 2.1.1 for the classical case. For an ohmic environment, after tracing out the bath degrees of freedom, the kernel of the influence action reads [3, 65],

$$D(\mathbf{x}) = -\frac{\eta}{2\pi} \int_0^{\hbar\beta} d\tau' \frac{\partial \mathbf{x}}{\partial \tau'} \cdot \frac{\partial \mathbf{x}}{\partial \tau} \ln \left| \sin \left[\frac{\pi}{\hbar\beta} (\tau - \tau') \right] \right|,$$

where $\eta = m_0\gamma$ is the phenomenological friction coefficient.

2.2.2 Physical systems

Josephson transmission lines

Among the physical systems that can be described by the action in Eq. (2.69) are current biased one-dimensional arrays of identical parallelly coupled Josephson junctions, also called

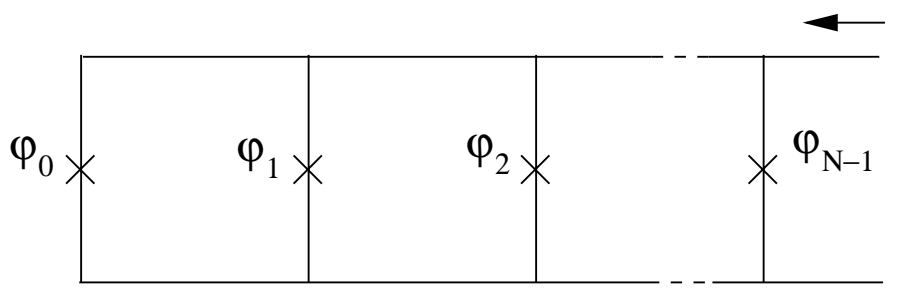


Figure 2.3: A discrete Josephson transmission line. The relevant degrees of freedom are the phase differences φ_n across the junctions.

discrete Josephson transmission lines (DJTL) [20], see Fig. 2.3. Within the framework of the resistively and capacitively shunted junction (RCSJ) model, the potential energy of a system of N identical JJ's in the presence of a bias current I is given by

$$\begin{aligned}
 V(\varphi_0, \dots, \varphi_{N-1}) = & \frac{E_J^2}{2LI_c^2} \sum_{n=1}^{N-1} (\varphi_n - \varphi_{n-1})^2 \\
 & + E_J \sum_{n=0}^{N-1} \left[1 - \cos(\varphi_n) - \frac{I\varphi_n}{NI_c} \right]. \quad (2.72)
 \end{aligned}$$

Here the phase differences across the JJ's are $\varphi_0, \dots, \varphi_{N-1}$. The first term in Eq. (2.72) represents the interaction energy due to the inductances between the loops. Here only the self-inductances of the loops are taken into account, whereas the mutual inductances are neglected [66]. Here, $E_J = (\Phi_0/2\pi)I_c$ is the Josephson energy, I_c the critical current of a single junction, L is the inductance, and $\Phi_0 = hc/2e$ is the flux quantum. The second term represents the tilted washboard potentials of the driven JJ's that arise due to the relation between currents and gauge invariant phases across the junctions. If we concentrate on the experimentally most interesting limit of currents I close to criticality, $NI_c - I \ll NI_c$, the tilted washboard potential can be well approximated by its cubic expansion, and we can identify $E = V$ [see Eqs. (2.70)-(2.72)] with $\kappa = E_J^2/LI_c^2$, $U_B = 4\sqrt{2}E_J/3$, $r = 2\sqrt{2}$, $\Delta = \sqrt{(1 - I/NI_c)}$, and $x_n = \varphi_n + r\Delta/2 - \pi/2$. In addition, we can use the particle picture, if we relate the mass m_0 to the capacitance of a junction by $m_0 = C(\Phi_0/2\pi)^2$ and the friction coefficient to the inverse of the ohmic shunt resistance, $\eta = 1/R$. Here, we consider systems with an overdamped dynamics such that we can neglect the contribution of the massive term.

Vortices in layered superconductors

Another physical realization of the model described by Eq. (2.69) is a stack of pancake vortices trapped in a columnar defect, which is artificially introduced in a layered superconductor. Both the magnetic field that produces the pancake vortices and the columnar

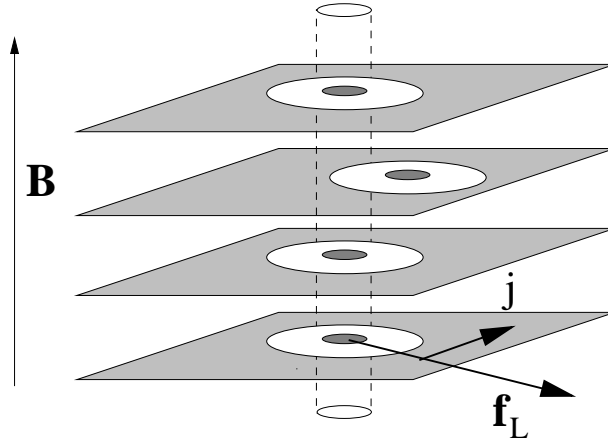


Figure 2.4: A stack of “pancakes” produced by a magnetic field **B** applied perpendicular to the layers. The pancakes are coupled to each other via magnetic interaction and Josephson currents. A columnar defect pins the vortex. When a current j is flowing through the system, a Lorentz force \mathbf{f}_L acts on the pancakes, reducing the energy barrier the vortex has to overcome to escape from the defect.

defect are perpendicular to the superconducting layers; see Fig. 2.4. Once a bias current $\mathbf{j} = j\mathbf{e}_y$ flows through the layers perpendicular to the magnetic field pointing in the z direction, the pancakes will be driven by the resulting Lorentz force. The corresponding free energy reads

$$\mathcal{F} = \frac{\varepsilon_l}{2s} \sum_{n=1}^{N-1} (\mathbf{u}_n - \mathbf{u}_{n-1})^2 + \sum_{n=0}^{N-1} [U_p(\mathbf{u}_n) - \mathbf{f}_L \cdot \mathbf{u}_n]. \quad (2.73)$$

The displacement of the n th pancake vortex from its equilibrium position in the columnar defect is now given by a two-dimensional vector $\mathbf{u}_n = (u_{n,x}, u_{n,y})$. The first sum in Eq. (2.73) models the magnetic and Josephson couplings between the layers by elastic interactions between pancakes in adjacent layers [67]. Here $\varepsilon_l = (\varepsilon_0 \lambda_{ab}^2 / \lambda_c^2) \ln(\lambda_{ab} / \xi_{ab})$ is the elastic constant, $\varepsilon_0 = \Phi_0^2 / (4\pi \lambda_{ab})^2$ is the vortex self energy per unit length, s is the interlayer spacing, and ξ_{ab} is the in-plane coherence length. Further, λ_c and λ_{ab} are the flux-penetration radii in the ab -plane and perpendicular to it, respectively. The second sum contains the columnar defect pinning potentials U_p felt by the single pancakes and the Lorentz force $\mathbf{f}_L = \Phi_0 \mathbf{j} \wedge \mathbf{e}_z / c$, where \mathbf{e}_z is the unit vector pointing perpendicular to the planes. The potential U_p is smooth on the length scale ξ_{ab} with a local minimum at the center of the defect. An upper estimate for the depth of the potential well is given by $U_B \approx d\varepsilon_0 \ln(R/\xi_{ab})$, where R is the radius of the columnar defect [36] and the parameter d denotes the superconducting layer thickness.

In the large current limit, $\Delta = \sqrt{1 - j/j_c} \ll 1$ gives a measure of how close the current j is to the critical current j_c . Then the sum of the pinning and the Lorentz part of the free

energy is approximately

$$U_B \sum_{n=0}^{N-1} \left[3\Delta \left(\frac{u_{n,x}}{R} \right)^2 - 2 \left(\frac{u_{n,x}}{R} \right)^3 + \frac{3}{2} \left(\frac{u_{n,y}}{R} \right)^2 \right], \quad (2.74)$$

where we have kept only the terms that are of order Δ^3 . The terms proportional to $\Delta(u_{n,y}/R)^2$ and $u_{n,y}^2 u_{n,x}/R^3$, that are of the order Δ^4 , have been neglected. Hence the displacements in the y direction are essentially decoupled from the displacements in the x direction. As a consequence, two identical integrals over $u_{n,y}$ appear in the numerator and in the denominator of the decay rate expression [14, 15], which will cancel each other. For this reason, we will neglect $u_{n,y}$ in the following. Renaming $x_n = u_{n,x}$, we obtain Eq. (2.70) with $\kappa = \varepsilon_l/s$. At low fields and low temperatures, the friction constant is given by the Bardeen-Stephen expression, $\eta = \Phi_0 H_{c2}/\rho_n c^2$, where H_{c2} is the upper critical magnetic field, ρ_n is the resistivity in the normal state, and c the speed of light. In most to-date known type-II superconductors, the vortex mass is extremely small and inertia terms are commonly neglected in the equations of motion [36].

2.2.3 Extrema of the Euclidean action

By applying the variational principle to the Euclidean action of the overdamped system, one finds the equations of motion in imaginary time

$$m\ddot{\mathbf{x}} + \nabla E(\mathbf{x}) + \frac{\eta}{\hbar\beta} \int_0^{\hbar\beta} d\tau' \frac{\partial \mathbf{x}}{\partial \tau'} \cot \left[\frac{\pi}{\hbar\beta} (\tau - \tau') \right] = 0. \quad (2.75)$$

Their solutions are given by the extremal trajectories, of which the saddle-point solutions are of special interest, since they lead to the decay of the chain from its metastable state. At high temperatures, quantum fluctuations play a minor role and the solutions of the equation of motion are time independent, $\partial_\tau \mathbf{x} = 0$. Hence, they are given by the extrema of the potential, $\nabla E(\mathbf{x}) = 0$. However, below a crossover temperature T_0 , quantum tunneling becomes relevant for the decay process and the solutions of the equation of motion are a function of the imaginary time.

A trivial type of saddle-point solution can be readily constructed from physical arguments. Consider the case in which the attractive interaction between the particles is much larger than the energy barrier. At high temperatures, the strongly coupled particles most probably are thermally activated over the barrier all at once and the chain basically behaves as a *rigid* rod. In this case the saddle point of the potential E is identical to the local maximum of the single DOF potential, $x_0 = \dots = x_{N-1} = r\Delta$. If, on the other hand, the energy barrier is of the order of the interaction strength or even larger, another saddle point of the potential emerges. Then above a certain barrier height the chain preferably decays via a kinked saddle-point solution with $x_0 \neq \dots \neq x_{N-1}$ that we call *elastic*. In the quantum regime, $T < T_0$, similar types of saddle points can be found. Since the saddle-point solutions determine the decay behavior, we find four decay regimes: thermal-rigid,

thermal-elastic, quantum-rigid, and quantum-elastic. In the following sections, we analyze the extrema of the Euclidean action which determine the decay in the various regimes.

Crossovers in the decay rate can also be related to the behavior of the pre-exponential factor. An example is the crossover from boundary- to bulk-excited decay, which is displayed by the model considered here and which is discussed in the context of thermal decay.

2.3 Thermally activated decay

2.3.1 Crossover from rigid to elastic decay

The thermally activated escape from the local minimum $\mathbf{x}_{\min} = (0, \dots, 0)$ of the potential proceeds mainly via the saddle-point solutions \mathbf{x}_s of (2.70). These unstable stationary solutions satisfy $\nabla E(\mathbf{x}_s) = 0$ and their curvature matrix $\mathbf{V}(\mathbf{x}_s)$ with elements

$$V_{nm}(\mathbf{x}_s) = \frac{\partial^2}{\partial x_n \partial x_m} E(\mathbf{x}_s) \quad (2.76)$$

has at least one negative eigenvalue.

Saddle-point bifurcation

The saddle point $\mathbf{x}_{rs} = (r\Delta, \dots, r\Delta)$, which we call the rigid saddle point (rs), can be readily identified. In Appendix A we calculate the eigenvalues of a curvature matrix for a uniform extremal solution. Using Eq. (A.10) we find the eigenvalues for $\mathbf{V}(\mathbf{x}_{rs})$,

$$\mu_n^{rs} = -\frac{6U_B\Delta}{r^2} + 4\kappa \sin^2\left(\frac{n\pi}{2N}\right). \quad (2.77)$$

The lowest eigenvalue $\mu_0^{rs} = -6U_B\Delta/r^2 < 0$ indicates that there is at least one unstable direction. It is the only one, if Δ is smaller than

$$\Delta_* = \frac{2\kappa r^2}{3U_B} \sin^2\left(\frac{\pi}{2N}\right). \quad (2.78)$$

However, when $\Delta \rightarrow \Delta_*$, the eigenvalue $\mu_1^{rs} = 6U_B(\Delta_* - \Delta)/r^2$ vanishes. At $\Delta = \Delta_*$ the saddle splits indicating the existence of an *elastic* saddle-point configuration \mathbf{x}_{es} . Below, we will show that for $\Delta > \Delta_*$ the energy $E(\mathbf{x}_{es})$ is smaller than $E(\mathbf{x}_{rs}) = N\tilde{U}_B$. Hence the *elastic* saddle-point configuration \mathbf{x}_{es} instead of the *rigid* one is the most probable configuration that leads to decay. One identifies the energy of the most probable configuration with the activation energy V_s . The saddle-point bifurcation can thus be interpreted as a crossover between two types of decay: the crossover from a *rigid* regime ($\Delta \leq \Delta_*$) with an activation energy $V_s = N\tilde{U}_B$ to an *elastic* regime ($\Delta > \Delta_*$) with $V_s = E(\mathbf{x}_{es})$. The corresponding decay diagram is shown in Fig. 2.5.

Rigid and elastic saddles

We now calculate the elastic saddle-point solutions. First, we discuss the appearance of the elastic saddle in the crossover regime for arbitrarily many DOF. The evolution of the elastic saddle point with increasing Δ is elucidated by analyzing the exactly solvable case of three DOF. Far from the crossover, the three-particle result is used to make an ansatz for the N -particle solutions, which can again be determined perturbatively.

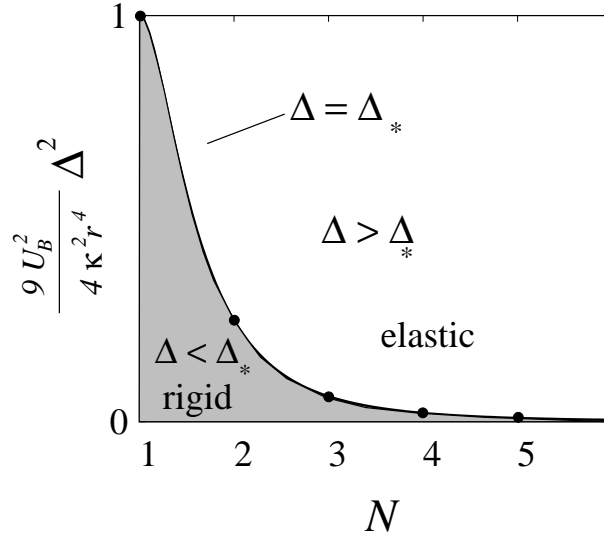


Figure 2.5: The decay diagram of a system with a small number of degrees of freedom N . The solid line and the dots indicate the crossover from rigid to elastic decay at $\Delta = \Delta_*$ as a function of N .

Near the crossover, we expand the elastic solution around the rigid one, $\mathbf{x}_{\text{es}} = \mathbf{x}_{\text{rs}} + \delta\mathbf{x}$. Then E is most conveniently represented in the coordinate system of the principal axis of $H(\mathbf{x}_{\text{rs}})$. The transformation is achieved by rewriting \mathbf{x} as a trigonometric polynomial,

$$x_n = r\Delta \left[q_0 + \sqrt{2} \sum_{k=1}^{N-1} q_k \cos \left(\frac{\pi k (n + 1/2)}{N} \right) \right]. \quad (2.79)$$

Here the coordinates q_k are the dimensionless amplitudes of the Fourier modes with a wave number k that measure the deviations from the minimum solution $x_n^{\text{min}} = 0$. In vector notation they read $\mathbf{q} = (q_0, \dots, q_{N-1})$. We define the dimensionless potential energy,

$$\mathcal{V}(\mathbf{q}) = \frac{1}{3U_B N \Delta^3} E(\mathbf{x}(\mathbf{q})) = \frac{1}{2} \sum_{k=0}^{N-1} \lambda_k^{\text{min}} q_k^2 + \mathcal{N}(\mathbf{q}), \quad (2.80)$$

where

$$\lambda_k^{\text{min}} = \frac{4\kappa r^2}{3U_B \Delta} \sin^2 \left(\frac{\pi k}{2N} \right) + 2 \quad (2.81)$$

are the eigenvalues of $(\partial_m \partial_n \mathcal{V})$ evaluated at the local minimum $\mathbf{q} = \mathbf{0}$ and $\mathcal{N}(\mathbf{q})$ contains the cubic terms,

$$\begin{aligned} \mathcal{N}(\mathbf{q}) = & -\frac{2}{3} q_0^3 - 2q_0 \sum_{k=1}^{N-1} q_k^2 - \frac{\sqrt{2}}{3} \sum_{k=1}^{N-1} q_k^2 (q_{2k} - q_{2(N-k)}) \\ & - \frac{2\sqrt{2}}{3} \sum_{m>k=1}^{N-1} q_m q_k (q_{m+k} + q_{m-k} - q_{2N-m-k}). \end{aligned}$$

Here, we define $q_k \equiv 0$ for $k > N - 1$. At the rigid saddle \mathbf{q}_{rs} the eigenvalues of the curvature matrix $(\partial_k \partial_l \mathcal{V})$ are given by

$$\lambda_k^{\text{rs}} = \frac{4\kappa r^2}{3U_B \Delta} \sin^2 \left(\frac{\pi k}{2N} \right) - 2. \quad (2.82)$$

For $\Delta < \Delta_*$, where the saddle-point solution is the rigid one with $x_n = R\Delta$, we have $q_0 = 1$ and $q_{k>0} = 0$ yielding $\mathcal{V}(\mathbf{q}_{\text{rs}}) = 1/3$. The second order expansion of \mathcal{V} around the rigid saddle point with $\mathbf{q} = \mathbf{q}_{\text{rs}} + \tilde{\mathbf{q}}$ thus reads

$$\mathcal{V}(\mathbf{q}) = \frac{1}{3} + \frac{1}{2} \sum_{k=0}^{N-1} \lambda_k^{\text{rs}} \tilde{q}_k^2. \quad (2.83)$$

At the crossover, λ_1^{rs} vanishes and the quadratic approximation of \mathcal{V} becomes independent of q_1 . Since large fluctuations in q_1 would not contribute to \mathcal{V} , this approximation becomes insufficient within the crossover regime where $\lambda_1^{\text{rs}} \ll 1$. Thus, in order to describe the contributions of fluctuations in q_1 more properly, higher-order terms in q_1 that arise due to the coupling to the other fluctuation coordinates have to be taken into account. One estimates that $\delta^2 \mathcal{V} \sim q_{n \neq 1} q_{m \neq 1} \sim q_{n \neq 1} q_1^2$. In comparison, the third-order terms $q_k q_m q_n$ with $m, n \neq 1$ are much smaller and hence can be neglected. Expanding around the rigid saddle, $q_0 = 1 + \tilde{q}_0$ and $q_k = \tilde{q}_k$ for $k > 0$, we approximate the potential energy thus by

$$\mathcal{V} = \frac{1}{3} + \frac{1}{2} \sum_{k=0}^{N-1} \lambda_k^{\text{rs}} \tilde{q}_k^2 - \tilde{q}_1^2 (2\tilde{q}_0 + \sqrt{2}\tilde{q}_2). \quad (2.84)$$

In the following, we define the crossover parameter $\alpha = \Delta_*/\Delta$. At the crossover $\alpha = 1$. We have $\alpha > 1$ in the rigid regime and $\alpha < 1$ in the elastic one. Within the crossover regime, $-1 \ll (\alpha - 1) \ll 1$. Note that $\lambda_1^{\text{rs}} = 2(\alpha - 1)$. By solving $\nabla \mathcal{V} = 0$, one finds the extrema. In addition to the extrema already found in the rigid regime, an elastic saddle-point solution \mathbf{q}_{es} with a *single* kink emerges slightly below the crossover, for $\alpha \lesssim 1$,

$$\begin{aligned} q_0^{\text{es}} &= \frac{(\alpha - 1)\lambda_2^{\text{rs}}}{\lambda_0^{\text{rs}} + 2\lambda_2^{\text{rs}}}, \\ q_1^{\text{es}} &= \left[\frac{(\alpha - 1)\lambda_0^{\text{rs}}\lambda_2^{\text{rs}}}{2\lambda_0^{\text{rs}} + 4\lambda_2^{\text{rs}}} \right]^{1/2}, \\ q_2^{\text{es}} &= \frac{\sqrt{2}(\alpha - 1)\lambda_0^{\text{rs}}}{2\lambda_0^{\text{rs}} + 4\lambda_2^{\text{rs}}}, \\ q_k^{\text{es}} &= 0, \quad k > 2, \end{aligned} \quad (2.85)$$

where λ_0^{rs} and λ_2^{rs} are evaluated at the crossover. This *elastic* solution has a lower activation energy than the stiff solution,

$$\mathcal{V}_{\text{es}}(\alpha) = \mathcal{V}[\mathbf{q}_{\text{es}}(\alpha)] \approx \frac{1}{3} - \frac{(\alpha - 1)^2}{8\pi\delta}, \quad (2.86)$$

where

$$\delta = -\frac{1}{2\pi} \left(\frac{2}{\lambda_0^{\text{rs}}} + \frac{1}{\lambda_2^{\text{rs}}} \right) > 0. \quad (2.87)$$

Since both $\mathcal{V}_{\text{es}}(\alpha)$ and its derivative $\mathcal{V}'_{\text{es}}(\alpha)$ are continuous, but $\mathcal{V}''(\alpha)_{\text{es}}$ is discontinuous at $\alpha = 1$, the crossover from rigid to elastic decay is of second order.

In order to illustrate that in our discrete model, close to the crossover, *boundary* nucleation is the dominant process leading to decay in the elastic regime, we will study a chain consisting of three particles, where the saddle-point solutions can be determined exactly. The parameter α can now take any value in the interval $\Delta_* \ll \alpha < \infty$. After substituting $\lambda_0^{\text{min}} = 2$, $\lambda_1^{\text{min}} = 2(1 + \alpha)$ and $\lambda_2^{\text{min}} = 2(1 + 3\alpha)$, the potential reads

$$\begin{aligned} \mathcal{V}(q_0, q_1, q_2) = & q_0^2 - \frac{2}{3}q_0^3 - (1 + \alpha)q_1^2 + (1 + 3\alpha)q_2^2 \\ & - 2q_0(q_1^2 + q_2^2) - \sqrt{2}q_2q_1^2 + \frac{\sqrt{2}}{3}q_2^3, \end{aligned} \quad (2.88)$$

From the extremal condition $\nabla \mathcal{V} = 0$ we calculate the extrema and find that slightly below the crossover in the elastic regime, only $\mathbf{q}_{\text{es}} = (q_0^{\text{es}}, q_1^{\text{es}}, q_2^{\text{es}})$ with

$$q_0^{\text{es}} = 1 - \frac{2}{3}(1 - \alpha), \quad (2.89)$$

$$q_1^{\text{es}} = (\pm) \left[\frac{2}{3}(1 - \alpha) - \frac{1}{2}(1 - \alpha)^2 \right]^{1/2}, \quad (2.90)$$

$$q_2^{\text{es}} = \frac{(1 - \alpha)}{6}, \quad (2.91)$$

is a possible elastic saddle-point solution. Energetically, the sign in front of q_1^{es} does not have any relevance since q_1 appears only quadratically in \mathcal{V} . It arises due to the existence of two degenerate solutions that can be mapped into each other by changing the sign of q_1 , which is equivalent to a mirror symmetry transformation. Inserting the solutions for the elastic saddle \mathbf{q}_{es} into \mathcal{V} , we can represent the free energy as a function of α ,

$$\mathcal{V}(\mathbf{q}_{\text{es}}) = \frac{1}{9}(1 + 3\alpha - \alpha^3). \quad (2.92)$$

At $\alpha = 1$ one finds $\mathcal{V}(\mathbf{q}_{\text{es}}) = \mathcal{V}(\mathbf{q}_{\text{rs}})$. For $\alpha > 1$, the value of $\mathcal{V}(\mathbf{q}_{\text{es}})$ is smaller than that of $\mathcal{V}(\mathbf{q}_{\text{rs}})$. There is a smooth crossover from the rigid \mathbf{q}_{rs} to the elastic configuration \mathbf{q}_{es} , which becomes the most probable one. To summarize, the activation energy $V_s = 9U_B\Delta^3\mathcal{V}$ of a three particle chain is given by

$$\begin{aligned} V_s^{\text{rs}} &= 3U_B\Delta^3, \\ V_s^{\text{es}} &= U_B(\Delta^3 + 3\Delta_*^2\Delta - \Delta_*^3) \end{aligned} \quad (2.93)$$

in the rigid and elastic regimes, respectively. In order to visualize the most probable configuration leading to decay, we represent the saddle-point solution in the original coordinates

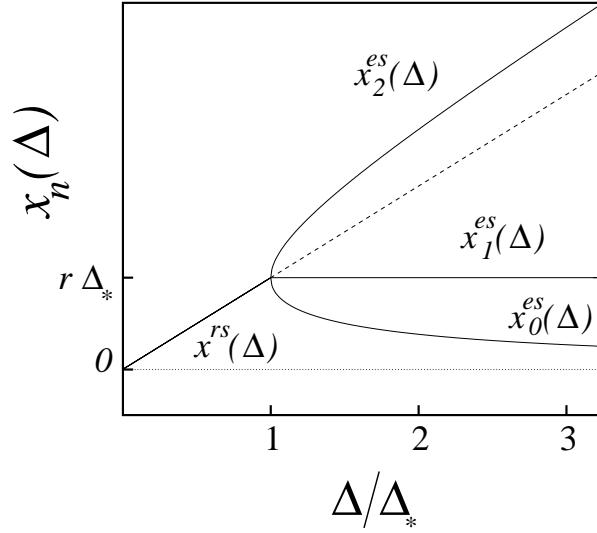


Figure 2.6: The saddle-point solutions x_n of a system with three degrees of freedom as a function of the barrier parameter Δ . For $\Delta < \Delta_*$ the system escapes rigidly from the local minimum of the potential via a configuration where all the particles are sitting on top of the barrier, $x_n = x^{rs}$. At $\Delta = \Delta_*$ the saddle splits and the elastic regime is entered for $\Delta > \Delta_*$. With decreasing increasing Δ , $x_0 = x_0^{es}$ approaches the minimum, $x_1 = x_1^{es} = r\Delta_*$ and the last particle $x_2 = x_2^{es} \rightarrow r(\Delta + \Delta_*)$ is hanging over the maximum of the single-particle potential.

x_0, x_1 , and x_2 as a function of the parameter Δ . We find that, for $\Delta > \Delta_*$,

$$x_0^{es} = \frac{r}{2} \left[\Delta + \Delta_* - \left(\Delta^2 + 2\Delta\Delta_* - 3\Delta_*^2 \right)^{1/2} \right], \quad (2.94)$$

$$x_1^{es} = r\Delta_*, \quad (2.95)$$

$$x_2^{es} = \frac{r}{2} \left[\Delta + \Delta_* + \left(\Delta^2 + 2\Delta\Delta_* - 3\Delta_*^2 \right)^{1/2} \right]. \quad (2.96)$$

Note that there exists a second solution with the same energy, which can be found by simply exchanging the indices 0 and 2. The results are displayed in Fig. 2.6 and illustrated in Fig. 2.7. By increasing the barrier parameter Δ above Δ_* , the symmetry along the defect is broken as the elastic saddle-point solution develops. When Δ is raised further, particle 0 approaches the potential minimum at $x_{\min} = 0$. Particle 1 tries to adjust between its neighbors. It is dragged towards the minimum by particle 0, but due to the coupling to particle 2, there will be a finite distance between the particles 1 and 0. On the other hand, particle 2 has swapped to the other side of the maximum.

Far in the elastic regime, $\Delta/\Delta_* \gg N^2$, we can generalize this picture to arbitrary N . Making the ansatz $x_{N-1} \gg x_{N-2} \gg x_{N-3} \sim 0$ we find the approximate solutions of $\nabla\mathcal{V} = 0$,

$$x_{N-1}^{es} \approx r\Delta + \kappa r^3/6U_B, \quad (2.97)$$

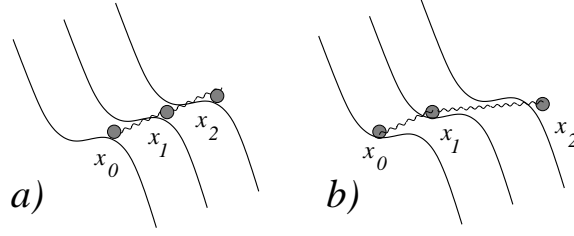


Figure 2.7: a) Rigid saddle-point solutions. b) Elastic saddle-point solutions.

$$x_{N-2}^{\text{es}} \approx \kappa r^3 / 6U_B, \quad (2.98)$$

$$x_{n \leq N-3}^{\text{es}} \approx 0, \quad (2.99)$$

and the equivalent saddle $x_n \rightarrow x_{N-1-n}$ with an activation energy

$$V_s = U_B \Delta^3 \left(1 + \frac{\kappa r^2}{2U_B \Delta} \right). \quad (2.100)$$

The activation energy V_s is displayed in Fig. 2.8 for $N = 2, 3, 4$. Note, that in this limit the elasticity term $\kappa r^2 \ll 2U_B \Delta$ and the activation energy resembles that of a single particle $V_s \sim U_B \Delta^3$ with a renormalized barrier parameter. This means that for large Δ the system cannot gain much energy by nucleating at the boundary and bulk excitations become important. The bulk saddles are particle like excitations at position m with a double kink,

$$x_m^{bs} \approx r\Delta + \kappa r^3 / 3U_B, \quad (2.101)$$

$$x_{m \pm 1}^{bs} \approx \kappa r^3 / 6U_B, \quad (2.102)$$

$$x_n^{bs} \approx 0, \quad (2.103)$$

where $|m - n| > 1$. They have an activation energy

$$V_s \approx U_B \Delta^3 \left(1 + \frac{\kappa r^2}{U_B \Delta} \right), \quad (2.104)$$

which is larger than the activation energy of the elastic boundary saddles. Though energetically not preferable, for $N \gg 1$ the decay can occur via bulk saddle-point solutions if the barrier parameter exceeds a crossover value, $\Delta > \Delta_{bs}$. The crossover to this new regime will be discussed in more detail in the next section.

2.3.2 Pre-exponential factor

Having determined the activation energies $V_s(\Delta)$ for the different regimes, the remaining task is to calculate the prefactor $P(\Delta)$ in Eq. (2.1).

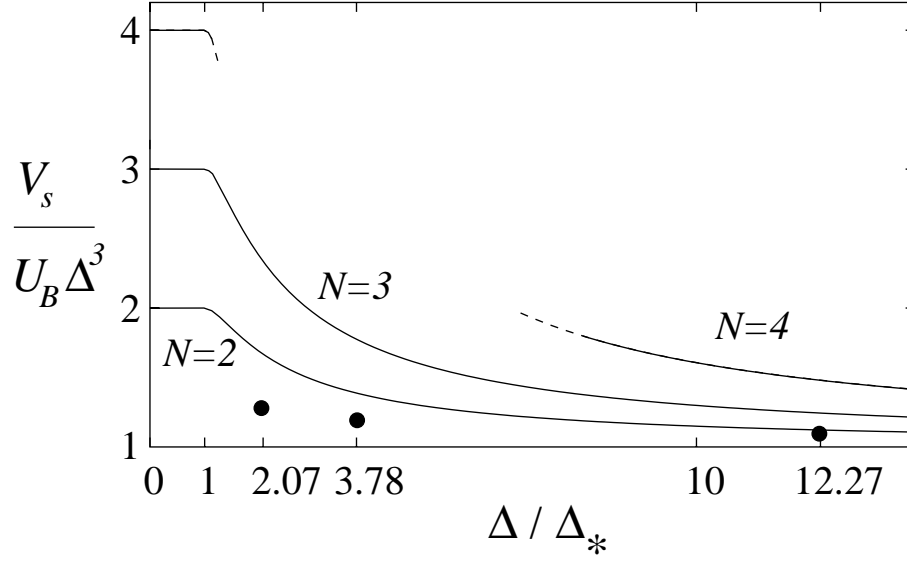


Figure 2.8: The activation energy V_s normalized to the activation energy of a single particle $U_B \Delta^3$ as a function of the barrier parameter Δ for various number of particles N . For $N = 2, 3$ the results are exact, for $N > 3$ the activation energy is calculated perturbatively in the crossover regime $\Delta \sim \Delta_*$ and in the limit of large Δ . For $N = 2$ the theoretical result and the experimental data (full dots) for activation energy are taken from Ref. [68].

Far from the crossover: Gaussian approximation

In the Gaussian approximation, the integrals in Eqs. (2.11) and (2.12) are evaluated by taking into account only the quadratic fluctuations around the saddle point \mathbf{q}_s ,

$$\mathcal{V}(\mathbf{q}) \approx \mathcal{V}(\mathbf{q}_s) + \frac{1}{2} \sum_{k=0}^{N-1} \lambda_k^s (q_k - q_k^s)^2, \quad (2.105)$$

and the local minimum \mathbf{q}_{\min} ,

$$\mathcal{V}(\mathbf{q}) \approx \mathcal{V}(\mathbf{q}_{\min}) + \frac{1}{2} \sum_{k=0}^{N-1} \lambda_k^{\min} (q_k - q_k^{\min})^2, \quad (2.106)$$

respectively. According to Eq. (2.31) one thus obtains a prefactor

$$\begin{aligned} P &= \frac{1}{2\pi} \sum_s \left(\sqrt{\frac{\gamma^2}{4} + \frac{|\mu_0|}{m_0}} - \frac{\gamma}{2} \right) \left[\frac{\det \mathbf{V}(\mathbf{x}_{\min})}{|\det \mathbf{V}(\mathbf{x}_s)|} \right]^{1/2} \\ &= \frac{1}{2\pi} \sum_s \left(\sqrt{\frac{\gamma^2}{4} + \frac{3U_B \Delta |\lambda_0^s|}{m_0 r^2}} - \frac{\gamma}{2} \right) \left(\prod_{n=0}^{N-1} \frac{\lambda_n^{\min}}{|\lambda_n^s|} \right)^{1/2}, \end{aligned} \quad (2.107)$$

where the sum over the saddle index s takes into account the contributions of equivalent saddles. Here $(\lambda_n^{\min})\mu_n^{\min}$ and $(\lambda_n^s)\mu_n^s$ are the (dimensionless) eigenvalues of the curvature

matrices $\mathbf{V}(\mathbf{x}_{\min})$ and $\mathbf{V}(\mathbf{x}_s)$ evaluated at the local minimum $(\mathbf{q}_{\min})\mathbf{x}_{\min}$ and the saddles $(\mathbf{q}_s)\mathbf{x}_s$, respectively. In contrast to a system with translational invariance, in the finite systems considered here there is no Goldstone mode of the critical nucleus. Hence, well above and below the crossover, where $\mu_1^s \neq 0$, the evaluation of P is not corrupted by divergences.

In the rigid regime, we take only the energetically lowest-lying saddle into account, and the sum over s reduces to a single contribution. With the determinants $\det \mathbf{V}(\mathbf{x}_{\min})$ and $\det \mathbf{V}(\mathbf{x}_{rs})$ given in Eqs. (A.7) and (A.9) in Appendix A.1, we find

$$P(\Delta < \Delta_*) = \frac{1}{2\pi} \left(\sqrt{\frac{\gamma^2}{4} + \frac{6U_B\Delta}{m_0 r^2}} - \frac{\gamma}{2} \right) \left[\frac{\sinh(N\Omega) \tanh(\Omega/2)}{\sin(N\tilde{\Omega}) \tan(\tilde{\Omega}/2)} \right]^{1/2}, \quad (2.108)$$

where $\Omega = 2 \operatorname{arcsinh}(\omega/2)$ and $\tilde{\Omega} = 2 \operatorname{arcsin}(\tilde{\omega}/2)$ with $\omega = \tilde{\omega} = \sqrt{6U_B\Delta/\kappa r^2}$. Below the crossover, two equivalent low-energy saddle-point solutions arise, as was discussed in Sec. 2.3.1. Taking the sum over both saddles yields

$$P(\Delta > \Delta_*) = \frac{1}{\pi} \left(\sqrt{\frac{\gamma^2}{4} + \frac{|\mu_0^{\text{es}}|}{m_0}} - \frac{\gamma}{2} \right) \left[\frac{\det \mathbf{V}(\mathbf{x}_{\min})}{|\det \mathbf{V}(\mathbf{x}_{\text{es}})|} \right]^{1/2}. \quad (2.109)$$

In Eqs. (A.11) and (A.12) we have estimated the determinant $\det \mathbf{V}(\mathbf{x}_{\text{es}})$ and the eigenvalue μ_0^{es} , respectively, in the limit $\Delta \gg \Delta_*$. We obtain

$$P(\Delta \gg \Delta_*) \approx \frac{1}{\pi} \left(\sqrt{\frac{\gamma^2}{4} + \frac{6U_B\Delta}{m_0 r^2}} - \frac{\gamma}{2} \right) [1 + \mathcal{O}(\Delta_*/\Delta)]. \quad (2.110)$$

As already mentioned in the previous section, for $N \gg 1$ a crossover to a regime can occur, where the decay dominantly occurs via bulk excitations. The number of degrees of freedom N_{bs} , where the crossover from boundary to bulk nucleation occurs, is found by comparing the corresponding rates according to Eq. (2.39). In the bulk regime, one has approximately N equivalent saddles and thus with Eqs. (A.13) and (A.14) the prefactor is given by

$$P \approx \frac{N}{2\pi} \left(\sqrt{\frac{\gamma^2}{4} + \frac{6U_B\Delta}{m r^2}} - \frac{\gamma}{2} \right) [1 + \mathcal{O}(\Delta_*/\Delta)]. \quad (2.111)$$

Comparing the rates for boundary and bulk nucleation with V_s given by Eqs. (2.100) and (2.104), and P given by Eqs. (2.110) and (2.111), respectively, we obtain

$$\Delta_{bs} \approx \left[\frac{2k_B T \ln(N/2)}{\kappa r^2} \right]^{1/2}, \quad (2.112)$$

Note, that within our approximations the choice of the system specific parameters N, R, κ and the temperature T is restricted to values that meet the constraint $\Delta_{bs} \ll 1$. If we vary

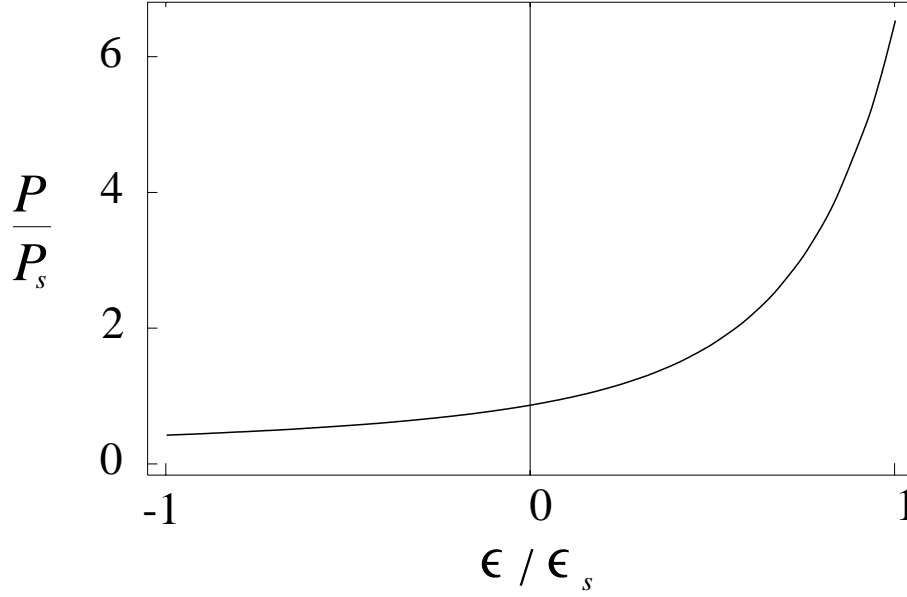


Figure 2.9: Scaling property of the prefactor P as a function of Δ near Δ_* . P/P_s is shown as a function of the distance ϵ from the crossover. Both P_s and ϵ_s are system specific scaling variables.

the number of particles at fixed Δ , the crossover from bulk to boundary nucleation occurs at

$$N_{bs} = 2 \exp \left[\frac{\kappa r^2 \Delta^2}{2k_B T} \right]. \quad (2.113)$$

Thus, the stiffer the chain, the longer the system has to be such that bulk nucleation is favored. At high temperatures the crossover occurs in smaller systems than at low ones.

Near the saddle-point bifurcation: Beyond steepest descent

In the crossover regime, where $\Delta \rightarrow \Delta_*$, the prefactor calculated in the Gaussian approximation diverges due to the vanishing eigenvalue $\lambda_1 \rightarrow 0$ as $P \sim 1/\sqrt{\lambda_1}$. The divergence can be regularized by taking into account the third order terms in q_1 in the approximation of $\mathcal{V}(\mathbf{q}')$ around the thermal saddle point. Defining $\epsilon = -\lambda_1/2 = 1 - \alpha$, the system-dependent scaling variables

$$P_s \approx \left(\sqrt{\frac{\gamma^2}{4} + \frac{3U_B \Delta_* |\lambda_0^{rs}|}{mr^2}} - \frac{\gamma}{2} \right) \frac{[\tanh(\Omega/2) \sinh(N\Omega)]^{1/2}}{4\pi \tan(\pi/2N)} \left(\frac{3U_B \Delta_*^3}{8\pi^3 N k_B T \delta} \right)^{1/4}$$

and

$$\epsilon_s = \left(\frac{8\pi \delta k_B T}{3N \Delta_*^3 U_B} \right)^{1/2},$$

we show in Appendix A.2 that

$$P(\epsilon) = P_s F(\epsilon/\epsilon_s), \quad (2.114)$$

where the function F is found to be

$$F(y) = \begin{cases} \pi \sqrt{\frac{|y|}{2}} \exp(y^2) [I_{-1/4}(y^2) - I_{1/4}(y^2)], & \Delta < \Delta_*, \\ 8^{-1/4} \Gamma(1/4), & \Delta = \Delta_*, \\ \pi \sqrt{\frac{|y|}{2}} \exp(y^2) [I_{-1/4}(y^2) + I_{1/4}(y^2)], & \Delta > \Delta_*. \end{cases} \quad (2.115)$$

For large $|\epsilon/\epsilon_s|$ the prefactor given in Eq. (2.114) matches with the Gaussian result. However, in the crossover regime, where $|\epsilon/\epsilon_s| < 1$, the Gaussian prefactor deviates strongly from Eq. (2.114), as expected, since here the Gaussian approximation becomes invalid. Since we considered a metastable situation, where $k_B T \ll U_B \Delta^3$, we have $\epsilon_s \ll 1$. Hence, the crossover regime is extremely narrow, $|\Delta - \Delta_*| \ll \Delta_*$. The function $F = P/P_s$, which is shown in Fig. 2.9, reflects two interesting aspects. First, one realizes that the behavior of the rate is smooth at the crossover. The divergences that occur in the Gaussian approximation are regularized by taking into account higher orders of the fluctuation coordinates. Second, F can be regarded as a scaling function, where the constants ϵ_s and P_s contain the system-specific parameters. The scaling relation is universal in the sense that it does not depend on the details of the considered system. Of course, a constraint is that the crossover must be of second order to guarantee the validity of the perturbative treatment that we applied. However, we have excluded systems with a single-particle potential that enforce a first-order transition from the beginning. Note, that Eq. (2.114) was found by taking into account only the cubic terms of the modes q_0 , q_1 , and q_2 . These long-wavelength excitations determine the decay process at the crossover, where the discreteness of the system becomes irrelevant. Hence the result can be applied to continuous systems as well. In fact, a similar crossover function is found at the second-order transition from thermal to quantum decay of a single particle in a metastable state [11]. Formally, this theory can also be used to describe a rigid-to-elastic crossover in the thermal decay of an elastic line escaping from a homogeneous defect, but with *periodic* instead of *open* boundary conditions, which we considered here. Note that the scaling function found in Ref. [11] is different from ours. One can indeed show that the functional form of the scaling function is influenced by the symmetry of the system.

2.3.3 Discussions

We studied the thermal decay of a chain of elastically coupled particles from a metastable state. The metastability arises from each of the particles being trapped in a local minimum of their single-particle potential. The energy barrier that separates the local minimum from energetically lower-lying ones can be tuned by a barrier parameter Δ . At $\Delta = 0$ the energy barrier vanishes and the metastability ceases to exist. With increasing Δ ,

we find three regimes. For small Δ , the decay occurs mainly via a rigid configuration, where all the degrees of freedom leave the trap at once. At $\Delta_* = 2\kappa r^2 \sin^2(\pi/2N)/3U_B$ a saddle-point bifurcation occurs, which marks a crossover from rigid to elastic motion. For $\Delta > \Delta_*$ the decay occurs mainly via boundary nucleation. However, at even higher values $1 \gg \Delta > \Delta_{bs} > \Delta_*$ a crossover to bulk nucleation can take place.

Our main goal was to evaluate the thermal decay rate $\Gamma_{cl} = P \exp(-V_s/k_B T)$ in the three classical regimes. This involves the calculation of the prefactor P and the activation energy V_s . The latter is given by the energy E of the most probable configuration leading to decay, namely, the lowest-lying saddle-point solution. We solved the problem for $N = 3$ particles exactly. Furthermore, we treated the case of an arbitrary number N of degrees of freedom perturbatively in the crossover regime and deep in the elastic regime. We have shown how the system uses its elasticity to lower the activation energy in the elastic regime. Whereas in the rigid regime the activation barrier is $V_s^{rs} = NU_B \Delta^3$, in the elastic regime near the crossover $V_s^{es} \approx V_s^{rs}(1 - C\epsilon^2)$, where $\epsilon = 1 - \Delta_*/\Delta$ and $C \sim 1$ is a positive constant that depends on the details of the potential. Increasing Δ far from the crossover in the elastic regime, the particles first escape via nucleation at the boundaries with an activation energy $V_s^{es} \sim U_B \Delta^3 + \kappa r^2 \Delta^2/2$, where the first term arises from the potential energy of the activated particle and the second term is the elastic energy of the kink that occurs in the boundary saddle. Due to the imposed free (von Neumann) boundary conditions, this kind of activation is energetically preferred compared to bulk nucleation with an activation energy $V_s^{bs} \sim U_B \Delta^3 + \kappa r^2 \Delta^2$. Since the bulk saddle consists of two kinks, twice the elastic energy is needed to activate a bulk nucleation process. However, in large systems, with $N \gg 1$, bulk nucleation becomes more probable for $1 \gg \Delta > \Delta_{bs} = \sqrt{2k_B T \ln(N/2)/\kappa r^2}$. Above Δ_{bs} the many possibilities to excite a particle somewhere in the bulk, which grow as N in the prefactor P , outnumber the two possibilities of boundary nucleation. At large Δ , the elastic interaction between the particles becomes less and less important and the activation energy approaches the energy $U_B \Delta^3$ which is needed to excite a single particle over the barrier independently of the others. To discuss the relevant energy scales, we now fix all variables except N . The crossover occurs when the number of degrees of freedom is increased above $N_{bs} = 2 \exp(\kappa r^2 \Delta^2/2k_B T)$. Hence, when the elastic coupling is weak and the temperature is high, bulk nucleation already occurs at lower values of N_{bs} . The crossover is thus determined by the ratio of elastic energy and thermal energy.

Second, we determined the prefactor P . Far from the rigid-to-elastic crossover, the calculation of the prefactor P was done in Gaussian approximation both in the rigid and elastic regimes. Near the crossover, the Gaussian approximation breaks down due to a diverging integral, which is caused by a vanishing eigenvalue of the curvature matrix. By taking into account higher orders in the fluctuation coordinates, we remove the divergence and obtain a smooth behavior of the rate at the crossover. The prefactor of the rate exhibits a scaling property $P/P_s = F(\epsilon/\epsilon_s)$. The function F is universal, but depends on the symmetries of the model. The scaling parameters P_s and ϵ_s are system-specific constants.

At the saddle-point bifurcation $V_s(\Delta)$, $V'_s(\Delta)$, $P(\Delta)$, $P'(\Delta)$, and $P''(\Delta)$ are continuous,

whereas $V_s''(\Delta)$ is discontinuous. Hence $\Gamma_{cl}(\Delta)$ and $\Gamma'_{cl}(\Delta)$ are continuous, but $\Gamma''_{cl}(\Delta)$ is discontinuous. Interpreting V_s as a thermodynamic potential, one easily sees the analogy between the crossover described here and a second-order phase transition. Note that close to the crossover the discrete structure of the model becomes unimportant, this kind of crossover can also be found in continuous systems [24, 25, 69]. The question arises whether first-order-like transitions could occur also in the thermal decay of elastic chain systems. As in the crossover from thermal to quantum decay [6, 18] the type of the crossover depends crucially on the shape of the single-particle potential $U(x_n)$. For a cubic parabola as is discussed in this work, the crossover is of second order. However, one could imagine other physical systems where the single-particle potential has a form that causes a first order transition.

The discrete model that we have used here is quite general. In the following we will discuss the application of the theory to two physical situations, the dynamics of the phases in DJTL's and the thermal creep of pancake vortices in layered superconductors with columnar defects.

DJTL are parallel coupled one dimensional Josephson-junction arrays, and the N degrees of freedom in this case are the phase differences across each of the N Josephson junctions. In current driven DJTL, metastable states occur when the degrees of freedom are trapped in a local minimum of the tilted washboard potential common to these systems. For $N = 2$, the problem reduces to the decay of the phases in a current biased dc SQUID [68, 70, 71]. Both the rigid decay [72], where the two phases behave as a single one, and the elastic case [68], where the two phases decay one after another, were experimentally observed. In the continuous limit, $N \rightarrow \infty$, the system becomes identical to a long JJ. The rigid-to-elastic crossover occurs [24, 25] when the junction length L_J becomes of the order of the Josephson length $L_J \sim \pi\lambda_J$. Here we analyzed a model for a DJTL, that provides a system to study the intermediate case of decay from a metastable state with a finite number of degrees of freedom. An experimental investigation of the rigid-to-elastic crossover requires that the current I can be driven through the crossover current $I_* = NI_c(1 - \Delta_*^2)$. An orientation for the choice of the system parameters can be obtained by comparison with the dc-SQUID [68, 72], noting that $I_* - NI_c \sim \Phi_0^2/(N^3 L^2 I_c)$. A systematic experimental study of the rigid-to-elastic crossover as a function of the system parameters L , I_c , and N is still lacking and would be highly desirable. A remaining question was, if additional crossovers occur in systems with a large number of degrees of freedom. In addition to the rigid-to-elastic crossover due to a saddle-point bifurcation of the potential energy, we find that in systems with large N a second crossover from boundary to bulk nucleation can take place. DJTL's with a large number of degrees of freedom offer the possibility to observe such a crossover by varying system-specific parameters or the temperature.

Let us now discuss our theory in the context of a single stack of pancake vortices trapped in a columnar defect in a layered superconductor. In the presence of a current density j that flows within the layers, the vortices are driven by the resulting Lorentz force. Once thermally activated from the defect, the pancake stack starts to move through the sample until it is trapped by another defect. The resulting motion is called thermal vortex creep. A typical example of a layered system is a high-temperature superconductor (HTSC). A

HTSC like YBCO is characterized by an anisotropy ratio of penetration depths $\lambda_c/\lambda_{ab} \sim 7$, and the ratio of the penetration depth to the coherence length is $\lambda_{ab}/\xi_{ab} \sim 100$. The distance between the layers s and their thickness d are $s \sim d \sim \xi_{ab}$, and the defect radius is $R \sim 2\xi_{ab}$. In order to observe the transition from rigid to elastic decay experimentally, the ratio $(j_c - j_*)/j_c > 0$ must be sufficiently large. However, substituting the defect energy $U_B \sim d\varepsilon_0 \ln(R/\xi_{ab})$ and the elastic energy $\varepsilon_l r^2/s$, with $\varepsilon_l = (\varepsilon_0/\gamma^2) \ln(\lambda_{ab}/\xi_{ab})$, into $(j_c - j_*)/j_c = \Delta_*^2$, one finds that even in systems with low anisotropy and a small number of layers $(j_c - j_*)/j_c < 10^{-2}$, indicating that the phenomenon could hardly be observed experimentally in high- T_c superconductors since j_* is very close to j_c . Thus, for large currents $j_c - j \ll j_c$ as considered here, the vortex system turns out to be mainly in the elastic regime where the layered structure of the material is important. Then, the activation barrier V_s is of the order of the single-particle barrier $U_B(1 - j/j_c)^{3/2}$, which can be interpreted as a vortex creep induced by the escape of individual pancakes from the columnar defect [73, 74]. This “decoupling” regime can be also entered from the low-current half-loop regime $j \ll j_c$, when the width of the bulk critical nucleus becomes of the order of the layer separation [67]. We find that at low temperatures T the thermal creep is induced by boundary (surface) nucleation. It would be interesting to investigate experimentally if the crossover from bulk to surface nucleation might be observed in thin layered samples. In sum, we calculated analytically the creep rate for coupled particles trapped in a metastable state and found that an interesting behavior arises from the interplay between elasticity, pinning, discreteness and finite-size effects.

2.4 Quantum statistical decay

So far we have discussed the classical regime at rather high temperatures, where the decay is determined by the extrema of the potential energy and the thermal fluctuations around them. Lowering the temperature, quantum fluctuations become relevant and one encounters the following scenario: above the crossover temperature from thermal to quantum decay, the quantum fluctuations around the time-independent thermal saddle-point solutions lead to an enhancement of the decay rate. The quantum mechanical enhancement factor is related to the spectrum of the second functional derivatives of the Euclidean action evaluated at the minimum and the thermal saddlepoint solution, respectively. Lowering the temperature, the quantum fluctuations become increasingly important. Within a narrow regime around the crossover temperature, the quantum corrections become exponentially large. Beyond the crossover temperature, in the quantum tunneling regime, the decay is dominated by the time-dependent saddle-point solutions of the Euclidean action.

In this section, which was partly published in Ref. [75], we discuss the effects of quantum fluctuations on the decay rate in the context of overdamped DJTL, which provide an ideal system for experimental investigations that can be manufactured with present day techniques. We first show the enhancement due to quantum fluctuations in the thermal regime. We calculate the crossover temperature from thermal to quantum decay in the rigid, as well as in the elastic regime. Then, we discuss the saddle-point solutions of the action as a function of the temperature and the energy barrier height, which in the case of DJTL or pancake vortices is determined by the bias current. An iterative perturbation procedure to calculate these extrema close to a saddle-point bifurcation is presented and applied to evaluate the split-instanton solutions, the elastic quantum saddle-point solutions of the Euclidean action. The various decay regimes, which are summarized in a diagram and the corresponding relaxation rates are discussed. Finally, the conclusions are drawn.

2.4.1 Onset of quantum fluctuations

In order to keep the dimensionless notation of the previous section, let us introduce the Euclidean action in terms of the dimensionless coordinates

$$S_E = g \int_{-\pi}^{\pi} d\tilde{\tau} L_E, \quad (2.116)$$

where the dimensionless imaginary time is given by $\tilde{\tau} = 2\pi\tau/\hbar\beta$ and the Euclidean Lagrangian is

$$L_E = M \frac{\theta^2}{J} \left(\frac{\partial \mathbf{q}}{\partial \tilde{\tau}} \right)^2 + \mathcal{V}(\mathbf{q}) - \frac{\theta}{\pi\sqrt{J}} \frac{\partial \mathbf{q}}{\partial \tilde{\tau}} \int_{-\pi}^{\pi} d\tilde{\tau}' \frac{\partial \mathbf{q}}{\partial \tilde{\tau}'} \ln \left| \sin \left[\frac{\tilde{\tau} - \tilde{\tau}'}{2} \right] \right|.$$

Here $g = 3N\hbar U_B \Delta^3 / (2\pi k_B T) \gg 1$ is the semiclassical parameter, the dimensionless temperature is given by $\theta = \pi\eta k_B T / [2\hbar\kappa \sin^2(\pi/2N)]$, and $M = 12U_B \Delta m / (r^2 \eta^2)$ is the dimensionless mass. In this chapter we will discuss the theory in the context of DJTL and it is

convenient to introduce the dimensionless current $J = 1/\alpha^2$. Note that $J = 0$ corresponds to criticality, $I = NI_c$.

From Eq. (2.63) one finds that the rate is related to the spectrum of the second functional derivative of the Euclidean action,

$$\Gamma = \frac{\rho\omega_s}{2\pi} \prod_{k=0}^{N-1} \left[\frac{\det(\hat{Q}_k^a)}{|\det(\hat{Q}_k^s)|} \right]^{1/2} \exp(-\beta V_s), \quad (2.117)$$

where the fluctuation operators \hat{Q}_k^a and \hat{Q}_k^s are defined by the second functional derivatives of S_E at the minimum \mathbf{q}_a ,

$$\hat{Q}_k^a \mathbf{q}(\tilde{\tau}) = \int_{-\pi}^{\pi} d\tilde{\tau}' \frac{\delta^2 S_E[\mathbf{q}_a]}{\delta q_k^2} \mathbf{q}(\tilde{\tau}'), \quad (2.118)$$

and at the thermal saddlepoint \mathbf{q}_s ,

$$\hat{Q}_k^s \mathbf{q}(\tilde{\tau}) = \int_{-\pi}^{\pi} d\tilde{\tau}' \frac{\delta^2 S_E[\mathbf{q}_s]}{\delta q_k^2} \mathbf{q}(\tilde{\tau}'), \quad (2.119)$$

respectively. The eigenvalues of the operator \hat{Q}_k^a are given by

$$^a\Lambda_n^k = \lambda_k^{min} + 2\frac{\theta}{\sqrt{J}}|n| + M\frac{\theta^2}{J}n^2. \quad (2.120)$$

For the thermal saddlepoint \mathbf{q}_s the eigenvalues of \hat{Q}_k^s read

$$^s\Lambda_n^k = \lambda_k^s + 2\frac{\theta}{\sqrt{J}}|n| + M\frac{\theta^2}{J}n^2. \quad (2.121)$$

The ratio of the determinants appearing in Eq. (2.117) is conveniently expressed in terms of the eigenvalues $^a\Lambda_n^k$ and $^s\Lambda_n^k$,

$$\frac{\det(\hat{Q}_k^a)}{|\det(\hat{Q}_k^s)|} = \prod_{n=-\infty}^{\infty} \frac{^a\Lambda_n^k}{|^s\Lambda_n^k|} = \frac{\lambda_k^{min}}{|\lambda_k^s|} \left\{ \frac{\Gamma[1 + \rho_1(\lambda_k^{min})]\Gamma[1 + \rho_2(\lambda_k^{min})]}{\Gamma[1 + \rho_1(\lambda_k^s)]\Gamma[1 + \rho_2(\lambda_k^s)]} \right\}^2, \quad (2.122)$$

where the products of eigenvalues are rewritten in terms of Gamma functions, and $\rho_{1,2}$ are the roots

$$\rho_{1,2}(\lambda) = \frac{\sqrt{J}}{\theta M} (1 \mp \sqrt{1 - M\lambda}). \quad (2.123)$$

Introducing the quantum correction factor

$$c_{qm} = \prod_{k=0}^{N-1} \left\{ \frac{\Gamma[1 + \rho_1(\lambda_k^{min})]\Gamma[1 + \rho_2(\lambda_k^{min})]}{\Gamma[1 + \rho_1(\lambda_k^s)]\Gamma[1 + \rho_2(\lambda_k^s)]} \right\}, \quad (2.124)$$

the thermal decay rate in the rigid regime including quantum corrections can thus be written in terms of the purely classical result,

$$\Gamma_{th} = c_{qm}\Gamma_{cl}. \quad (2.125)$$

At high temperatures c_{qm} simplifies to

$$c_{qm} = \exp\left(\frac{\pi^2 J}{6M\theta^2} \sum_{k=0}^{N-1} (\lambda_k^{min} - \lambda_k^s)\right) + \mathcal{O}(\theta^{-4}), \quad (2.126)$$

which is independent of dissipation, since $\theta \propto \eta$ and $M \propto \eta^{-2}$. In the limit $\theta \rightarrow \infty$, c_{qm} becomes unity. In the rigid regime one finds

$$c_{qm} = \exp\left(\frac{2\pi^2 J}{3M\theta^2}\right) + \mathcal{O}(\theta^{-4}). \quad (2.127)$$

2.4.2 Crossover temperature from thermal to quantum decay

Since λ_0^s is negative, there exists a characteristic temperature θ_0 at which ${}^s\Lambda_1^0$ vanishes,

$$\lambda_0^s + 2\frac{\theta_0}{\sqrt{J}} + M\frac{\theta_0^2}{J} = 0. \quad (2.128)$$

Thus, lowering the temperature, c_{qm} increases and diverges at

$$\theta_0 = \frac{\sqrt{J}}{M} \left(\sqrt{1 - M\lambda_0^s} - 1 \right). \quad (2.129)$$

The overdamped limit reads

$$\theta_0 = \frac{|\lambda_0^s|\sqrt{J}}{2}. \quad (2.130)$$

For the rigid regime, where $\lambda_0^{rs} = -2$ we find

$$\theta_0(J < 1) = \sqrt{J}, \quad (2.131)$$

and in the elastic regime with $\lambda_0^{es} \approx \lambda_0^{rs} - 2\lambda_1^{rs}\lambda_2^{rs}/(\lambda_0^{rs} - \lambda_2^{rs})$

$$\theta_0(J \gtrsim 1) = \sqrt{J} + (J - \sqrt{J}) \left(2 - \frac{1}{2\cos^2(\pi/2N)} \right). \quad (2.132)$$

The divergence of c_{qm} at θ_0 has its origin in the Gaussian treatment of the fluctuations, which breaks down in the thermal to quantum crossover regime. Taking into account higher order fluctuation terms in the action in the same manner as presented for the thermal decay, the divergent terms should be regularized, as was shown for the single particle case [2, 11].

2.4.3 Instantons

For $\theta < \theta_0$ quantum tunneling becomes relevant and the instanton solutions dominate the decay from metastability. For $J > 1$, the crossover from thermal to quantum decay is of second order. A detailed procedure showing how to obtain the saddle-point solutions close to the thermal-to-quantum crossover was given in Ref. [76] and can be applied to calculate the quantum elastic solutions. In this paper we will concentrate on the current regime $J < 1$, where in addition to the transition from the thermal to the quantum rigid regime a crossover from the quantum rigid to the quantum elastic phase can take place.

The rigid quantum solution is found by setting $q_k = 0$ for $k > 0$. In this case the equations $\delta S_E / \delta q_k = 0$ with $k > 0$ are trivially satisfied and the remaining equation for $k = 0$ describes the thermally assisted quantum tunneling of a single degree of freedom q_0 . Its solution is the well-known instanton obtained by Larkin and Ovchinnikov [6]

$$q_0^{(0)}(\tilde{\tau}) = \left(\frac{\theta}{\theta_0}\right)^2 \frac{1}{1 - \sqrt{1 - \theta^2/\theta_0^2} \cos(\tilde{\tau})}. \quad (2.133)$$

Inserting $q_0^{(0)}$ and $q_{k>0}^{(0)} = 0$ into Eq. (2.116), one obtains the extremal action in the rigid quantum regime

$$S_{qr} = S_0 \left[1 - \frac{1}{3} \left(\frac{\theta}{\theta_0}\right)^2 \right], \quad (2.134)$$

where $S_0 = 4\pi N \eta \Delta^2$.

As for $J > 1$, nonuniform saddle-point solutions of the action exist in the quantum regime in a certain parameter range even for $J < 1$. If the action evaluated at this extremum is lower than S_{qr} , the nonuniform configuration is the most probable one leading to decay from the metastable state via quantum tunneling. Tuning the temperature θ at a fixed bias current, a nonuniform saddle-point solution can develop in two different ways. One possibility is that a less probable nonuniform configuration, which coexists with the rigid saddle point above a critical temperature θ_1 , becomes the lowest-lying saddle point of the Euclidean action below θ_1 . Then the most probable configuration abruptly changes from uniform to nonuniform. Since the first derivative of the rate $\partial_\theta \Gamma$ is discontinuous at θ_1 , the crossover is of first order. Another scenario is encountered, if at a critical temperature θ_2 the rigid saddle point bifurcates into new saddle points which have the lowest action. This crossover, known as instanton splitting, [70, 71] is of second order.

A strategy to determine nonuniform saddle-point solutions for $J < 1$ is to first search for a saddle-point splitting and then to verify whether a first-order transition might have occurred before the bifurcation has taken place. If a first-order transition can be ruled out, the new bifurcated saddle points have the lowest action. In this case the bifurcation causes a second-order crossover from a single to a split-instanton regime.

Following this idea, we first identify the saddle-point bifurcation, calculate the split instantons and test whether or not a first-order transition has already occurred.

2.4.4 Iterative perturbation scheme

In this section we present an iteration scheme to calculate the split-instanton solutions for $J < 1$. We start by expanding the coordinates around the single instanton solution,

$$q_k(\tilde{\tau}) = q_k^{(0)}(\tilde{\tau}) + \tilde{q}_k(\tilde{\tau}). \quad (2.135)$$

and rewrite the Euclidean action in terms of the new variables,

$$S_E = S_{qr} + g \int_{-\pi}^{\pi} d\tilde{\tau} \left[\frac{1}{2} \sum_{k=0}^{N-1} \tilde{q}_k \hat{Q}_k \tilde{q}_k + \mathcal{N}(\tilde{\mathbf{q}}) \right]. \quad (2.136)$$

The operators \hat{Q}_k are defined as

$$\begin{aligned} \hat{Q}_k \tilde{q}_k(\tilde{\tau}) &= \frac{1}{g} \int_{-\pi}^{\pi} d\tilde{\tau}' \frac{\delta^2 S_E[\mathbf{q}^{(0)}]}{\delta q_k(\tilde{\tau}) \delta q_k(\tilde{\tau}')} \tilde{q}_k(\tilde{\tau}') \\ &= (\lambda_k^{\min} - 4q_0^{(0)}) \tilde{q}_k(\tilde{\tau}) \\ &\quad + \frac{\theta}{\pi\sqrt{J}} \int_{-\pi}^{\pi} d\tilde{\tau}' \frac{\partial \tilde{q}_k(\tilde{\tau}')}{\partial \tilde{\tau}'} \cot\left(\frac{\tilde{\tau} - \tilde{\tau}'}{2}\right). \end{aligned}$$

To determine the split instantons, we have to find saddle points of the action with nonzero \tilde{q}_k . Hence we have to solve the equations of motion,

$$\hat{Q}_k \tilde{q}_k = -\frac{\partial \mathcal{N}(\tilde{\mathbf{q}})}{\partial \tilde{q}_k}, \quad (2.137)$$

which constitute a system of coupled nonlinear differential equations. In general, they cannot be solved exactly. However, close to the saddle-point bifurcation, the extremal amplitudes \tilde{q}_k are small and we can calculate approximate solutions by applying an iterative perturbation scheme. This leads to a hierarchy of inhomogeneous *linear* equations,

$$\hat{Q}_k \tilde{q}_k^{(i)} = F_k^{(i)}, \quad (2.138)$$

where i denotes the iteration step. In the first iteration $i = 1$ we take only terms into account that are linear in \tilde{q}_k . The higher-order terms on the right-hand side of Eq. (2.137) are neglected. Thus, $F_k^{(1)} = 0$ and Eqs. (2.138), which have to be solved, are homogeneous. For $i > 1$, the amplitudes calculated in the previous iteration are substituted into $\partial \mathcal{N}$ such that the inhomogeneous terms are given by

$$F_k^{(i)}(\tilde{\tau}) = -\frac{\partial \mathcal{N}[\tilde{\mathbf{q}}^{(i-1)}(\tilde{\tau})]}{\partial \tilde{q}_k}. \quad (2.139)$$

After each iteration step i , we thus obtain approximate (special) solutions for the amplitudes \tilde{q}_k by formally inverting Eq. (2.138),

$$\tilde{q}_k^{(i)} = \hat{Q}_k^{-1} F_k^{(i)}. \quad (2.140)$$

Of course, a straightforward inversion is not possible, if \hat{Q}_k is singular. Below, we will discuss how to handle equations with a singular operator.

The inversion is most conveniently performed by representing Eq. (2.140) in terms of the eigenfunctions of the operators \hat{Q}_k which we will determine now. One realizes that the operators \hat{Q}_0 and \hat{Q}_k only differ by a constant term

$$\hat{Q}_k = \hat{Q}_0 + \lambda_k^{\min} - \lambda_0^{\min}.$$

They trivially commute and have a common set of eigenfunctions ψ_m . The eigenvalues Λ_m^k of the operators \hat{Q}_k are related by

$$\Lambda_m^k = \Lambda_m^0 + \lambda_k^{\min} - \lambda_0^{\min}.$$

It is, therefore, sufficient to concentrate on the eigenvalue problem

$$\hat{Q}_0 \psi_m = \Lambda_m^0 \psi_m,$$

which was studied by Larkin and Ovchinnikov [7] in the context of single-particle tunneling with dissipation. They obtained the spectrum

$$\begin{aligned} \Lambda_1^0 &= -2 + 2\alpha_c, \\ \Lambda_0^0 &= -2\alpha_c, \\ \Lambda_{-1}^0 &= 0, \\ \Lambda_m^0 &= 2[1 + (|m| - 2)\theta/\theta_0], \quad |m| \geq 2, \end{aligned}$$

where $\alpha_c = 1/2 + \sqrt{5/4 - \theta^2/\theta_0^2}$ and showed that the eigenfunctions

$$\psi_m = \sum_{n=-\infty}^{\infty} C_{m,n} e^{in\tilde{\tau}}$$

have Fourier coefficients of the form

$$C_{m,n} = \begin{cases} S_m(\tilde{C}_{m,n} + d_{m,n}), & n \geq 0, \\ \pm S_m(\tilde{C}_{m,n} + d_{m,n}), & \pm m > 0, \quad n < 0, \end{cases}$$

with $d_{m,n} = 0$ for $|m| < 2$ and $|n| + 2 > |m| \geq 2$. Note that the ψ_m are even (odd) for positive (negative) m and the S_m are chosen such that the eigenfunctions are normalized,

$$\langle \psi_m, \psi_m \rangle = \int_{-\pi}^{\pi} d\tilde{\tau} \psi_m^2(\tilde{\tau}) = 1.$$

For $m = 0, 1$ they obtained

$$\tilde{C}_{m,n} = \left(|n| - \frac{\theta_0}{2\theta} \Lambda_m^0 \right) e^{-b|n|} \quad (2.141)$$

with $\tanh b = \theta/\theta_0$. In fact, calculating the remaining coefficients for $m \leq -1$ and $m \geq 2$, we find that Eq. (2.141) holds for any m with

$$d_{m,n} = \begin{cases} -\tilde{C}_{m,n}, & |n| < |m| - 2, \\ & n = m + 2 = 0, \\ \frac{1}{2} \left(\frac{\theta_0^2}{\theta^2} + 1 \right), & n = m - 2 = 0, \\ \frac{1}{4} \left(\frac{\theta_0^2}{\theta^2} - 1 \right) e^{-b(|m|-4)}, & |n| = |m| - 2 > 0. \end{cases}$$

With these results, we now represent Eq. (2.140) in terms of the basis ψ_m with

$$\tilde{q}_k^{(i)} = \sum_{m=-\infty}^{\infty} c_{k,m}^{(i)} \psi_m,$$

$$F_k^{(i)} = \sum_{m=-\infty}^{\infty} f_{k,m}^{(i)} \psi_m,$$

and obtain a special solution in terms of the coefficients

$$c_{k,m}^{(i)} = f_{k,m}^{(i)} / \Lambda_m^k, \quad \text{if } \Lambda_m^k \neq 0. \quad (2.142)$$

If for some k' and m' the eigenvalue $\Lambda_{m'}^{k'} = 0$, the operator \hat{Q}_k is singular and a unique solution of Eq. (2.138) cannot be found within the i th iteration. However, after performing all necessary iterations, the solutions have to be the lowest-lying saddle point of the Euclidean action. This constraint enables us to determine the so far arbitrary coefficients $c_{k',m'}^{(i)}$ by requiring that the Euclidean action as a function of the coefficients has to be minimal,

$$S_E \left(\{c_{k',m'}^{(i)}\} \right) = \min.$$

2.4.5 Nonuniform instanton solution

After we have explained in detail how to obtain the approximate solutions, we are now ready to perform the calculations explicitly. First, we show that the instanton splitting occurs at $\alpha = \alpha_c$ and then we apply the perturbation scheme to determine the split-instanton solutions.

Recall that $\alpha = (\lambda_1^{\min} - \lambda_0^{\min})/2 = 1/\sqrt{J}$. The negative Λ_0^0 indicates that the operator \hat{Q}_0 has an unstable mode, which is responsible for the imaginary part of the free energy and hence for the finite decay rate of the metastable state. For $\alpha > \alpha_c$, the spectrum of \hat{Q}_1 is positive definite. Since $\lambda_k^{\min} - \lambda_0^{\min} > 2\alpha$, for $k > 1$ we have $\Lambda_m^k > 0$ and hence all higher modes $q_{k>0}$ are stable. For $\alpha < \alpha_c$, the lowest eigenvalue Λ_0^1 of \hat{Q}_1 becomes negative, indicating that the corresponding mode also becomes unstable and that a new saddle point with a lower S_E exists. Thus at $\alpha = \alpha_c$ a split-instanton solution emerges [71].

To determine the split-instanton solutions for $\alpha \lesssim \alpha_c$, we now apply the iterative procedure and solve Eqs. (2.138). In the first iteration $F_m^{(1)} = 0$. According to Eq. (2.142) most of the coefficients $c_{k,m}^{(1)}$ are zero except $c_{0,-1}^{(1)}$ and $c_{1,0}^{(1)}$. The coefficient $c_{0,-1}^{(1)}$ cannot be uniquely determined since $\Lambda_{-1}^0 = 0$. However, the corresponding odd eigenfunction ψ_{-1} is associated to imaginary time translation symmetry and does not contribute to the value of S_E . We have, therefore, the freedom to choose $c_{0,-1}^{(i)} = 0$ within this and the following iterations. At $\alpha = \alpha_c$, where $\Lambda_0^1 = 0$, the operator \hat{Q}_1 becomes singular. Here the instanton splits since the coefficient $\zeta \equiv c_{1,0}^{(1)}$ of the dangerous mode ψ_0 of \hat{Q}_1 can have a finite value that remains to be determined by minimizing $S_E(\zeta)$. To lowest order, the split-instanton solution at $\alpha = \alpha_c$ is thus given by

$$\tilde{q}_1^{(1)}(\tilde{\tau}) = \zeta \psi_0(\tilde{\tau}), \quad \tilde{q}_{k \neq 1}^{(1)}(\tilde{\tau}) = 0. \quad (2.143)$$

In analogy with the Landau theory of phase transitions we can interpret S_E as a thermodynamic potential and ζ as an order parameter. A finite ζ indicates the existence of a quantum elastic solution.

Using $\hat{Q}_1(\alpha) = \hat{Q}_1(\alpha_c) + 2(\alpha - \alpha_c)$, recalling that $\hat{Q}_1(\alpha_c)\psi_1 = 0$ and inserting the perturbative result (2.143) into Eq. (2.136), one obtains the split-instanton action up to terms quadratic in the dangerous mode, $S_E(\zeta) = S_{qr} + g(\alpha - \alpha_c)\zeta^2$. However, in order to be able to minimize the action as a function of ζ for $\alpha < \alpha_c$, at least the terms quartic in ζ have to be calculated,

$$S_E(\zeta) = S_{qr} + g \left[(\alpha - \alpha_c)\zeta^2 + \delta\zeta^4 \right]. \quad (2.144)$$

The case $\delta \leq 0$, which indicates that a first-order transition has occurred will be discussed later in more detail. For $\delta > 0$, the minimal value of S_E is given by $|\zeta_{min}| = \sqrt{(\alpha_c - \alpha)/2\delta}$ and the extremized action reads

$$S_{qe} = S_E(\zeta_{min}) = S_{qr} - \frac{g(\alpha - \alpha_c)^2}{4\delta}. \quad (2.145)$$

Note that ζ is small close to α_c and can be regarded as a perturbation parameter.

In the first iteration we considered corrections to the single instanton solution of the order ζ . In order to determine δ , the split-instanton solution up to orders of ζ^2 has to be treated. Consequently, we have to perform the second iteration of the perturbation procedure. The inhomogeneous terms $F_k^{(2)}$ in Eq. (2.138) are found by substituting $\tilde{q}_k^{(1)}$ into Eq. (2.139). For $k \neq 0, 2$ the $F_k^{(2)} = 0$, hence $\tilde{q}_k^{(2)} = \tilde{q}_k^{(1)}$, whereas for $k = 0, 2$ we obtain $F_0^{(2)} = 2\zeta^2(\psi_0)^2$ and $F_2^{(2)} = \sqrt{2}\zeta^2(\psi_0)^2$. The remaining task within this iteration is to solve the equations

$$\begin{aligned} \hat{Q}_0 \tilde{q}_0^{(2)} &= 2\zeta^2(\psi_0)^2, \\ \hat{Q}_2 \tilde{q}_2^{(2)} &= \sqrt{2}\zeta^2(\psi_0)^2. \end{aligned}$$

Representing $(\psi_0)^2$ in the basis ψ_m , we obtain

$$(\psi_0)^2 = \sum_{m=0}^{\infty} a_m \psi_m.$$

Note that the odd ψ_m with $m < 0$ do not appear in the sum, since $(\psi_0)^2$ is an even function. The coefficients a_m are given by

$$a_m = \langle \psi_m, \psi_0^2 \rangle = 2\pi \sum_{l,n} C_{m,n} C_{0,l} C_{0,n+l}.$$

For our purposes it will be more than sufficient to consider only the first three coefficients a_0, a_1 and a_2 , since $a_m/a_{m+1} \ll 1$ in the entire quantum regime. After tedious but straightforward calculations, we find

$$a_0 = \frac{\left(\frac{13}{8}\alpha_c + \frac{17}{4}\right) \frac{\theta_0}{\theta} - \left(\frac{37}{4}\alpha_c + \frac{19}{2}\right) \frac{\theta_0^3}{\theta^3} + \left(\frac{69}{8}\alpha_c + \frac{21}{4}\right) \frac{\theta_0^5}{\theta^5}}{\sqrt{2\pi} \left[\left(2\alpha_c + \frac{3}{2}\right) \frac{\theta_0^3}{\theta^3} - \left(\alpha_c + \frac{3}{2}\right) \frac{\theta_0}{\theta} \right]^{3/2}}, \quad (2.146)$$

$$a_1 = \frac{\left(-\frac{1}{8}\alpha_c + \frac{1}{8}\right) \frac{\theta_0}{\theta} - \left(\frac{1}{4}\alpha_c + \frac{3}{4}\right) \frac{\theta_0^3}{\theta^3} + \left(\frac{3}{8}\alpha_c + \frac{5}{8}\right) \frac{\theta_0^5}{\theta^5}}{\sqrt{2\pi} \left[\left(-2\alpha_c + \frac{7}{2}\right) \frac{\theta_0^3}{\theta^3} - \left(\alpha_c - \frac{5}{2}\right) \frac{\theta_0}{\theta} \right]^{1/2} \left[\left(2\alpha_c + \frac{3}{2}\right) \frac{\theta_0^3}{\theta^3} - \left(\alpha_c + \frac{3}{2}\right) \frac{\theta_0}{\theta} \right]}, \quad (2.147)$$

$$a_2 = \frac{\left(\frac{5}{4}\alpha_c + \frac{13}{8}\right) \frac{\theta_0}{\theta} - \left(\frac{7}{2}\alpha_c + \frac{13}{4}\right) \frac{\theta_0^3}{\theta^3} + \left(\frac{9}{4}\alpha_c + \frac{13}{8}\right) \frac{\theta_0^5}{\theta^5}}{\sqrt{2\pi} \left[\frac{1}{4} \frac{\theta_0^4}{\theta^4} - \frac{1}{2} \frac{\theta_0^3}{\theta^3} + \frac{1}{2} \frac{\theta_0^2}{\theta^2} - \frac{1}{2} \frac{\theta_0}{\theta} + \frac{1}{4} \right]^{1/2} \left[\left(2\alpha_c + \frac{3}{2}\right) \frac{\theta_0^3}{\theta^3} - \left(\alpha_c + \frac{3}{2}\right) \frac{\theta_0}{\theta} \right]}, \quad (2.148)$$

$$a_m \approx 0, \quad m > 2. \quad (2.149)$$

Note that for $\theta \rightarrow \theta_0$ the coefficients converge to $a_0 \rightarrow 1/\sqrt{2\pi}$ and $a_k \rightarrow 0$ for $k > 0$. Substituting $f_{0,m} = 2\zeta^2 a_m$ and $f_{2,m} = \sqrt{2}\zeta^2 a_m$ into Eq. (2.142) we find excellent approximations of the expansion coefficients $c_{0,m}^{(2)}$ and $c_{2,m}^{(2)}$. Having determined $\tilde{q}_0^{(2)}$ and $\tilde{q}_2^{(2)}$, the second iteration of the perturbation procedure is completed.

Evaluating Eq. (2.136) with $\tilde{q}_0^{(2)}, \tilde{q}_2^{(2)} \propto \zeta^2$, we obtain the coefficient δ of the quartic term in $S_E(\zeta)$,

$$\delta = -\frac{1}{\zeta^2} \int_{-\pi}^{\pi} d\tilde{\tau} [\psi_0(\tilde{\tau})]^2 \left(\tilde{q}_0^{(2)} + \frac{\tilde{q}_2^{(2)}}{\sqrt{2}} \right). \quad (2.150)$$

Performing the integral and using the orthogonality of the ψ_m , we find

$$\delta = -\sum_{m=0}^{\infty} a_m^2 \left(\frac{2}{\Lambda_m^0} + \frac{1}{\Lambda_m^2} \right). \quad (2.151)$$

The function $\delta(\theta/\theta_0)$ is shown in Fig. 2.10 for $N = 2, 3$ and $N \rightarrow \infty$. At first it may be surprising that the curve for $N \rightarrow \infty$ lies in between the curves for $N = 2$ and $N = 3$. The reason is that for $N = 2$ the mode \tilde{q}_2 does not exist and $\delta = -\sum a_m^2/\Lambda_m^0$. Since $\Lambda_m^2 = \Lambda_m^0 + 8\alpha_c \cos^2(\pi/2N) > 0$ for $N > 2$ it is clear that $\delta(\theta/\theta_0, N = 2) > \delta(\theta/\theta_0, N > 2)$. When evaluating Eq. (2.151) for $N \geq 3$ one obtains the relation $\delta(\theta/\theta_0, N) < \delta(\theta/\theta_0, N+1)$. In other words, for $N > 3$ the graphs lie in between the ones for $N = 3$ and $N \rightarrow \infty$. In the limit $\theta \rightarrow 0$ we find $\delta \propto \theta_0/\theta$ when taking into account only the leading terms in Eqs. (2.146)-(2.148). Hence, g/δ in Eq. (2.145) converges to a constant value for $\theta \rightarrow 0$. With increasing θ the coefficient δ decreases and vanishes at the characteristic temperature

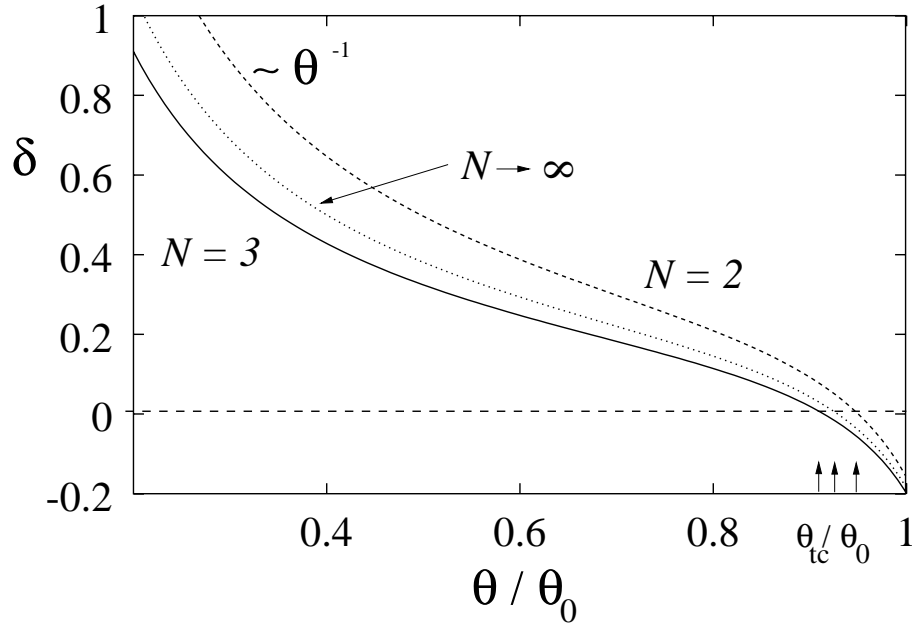


Figure 2.10: The fourth-order expansion coefficient δ of the Euclidean action $S_E(\zeta) = S_{qr} + g[(\alpha - \alpha_c)\zeta^2 + \delta\zeta^4 + \gamma\zeta^6]$ as a function of dimensionless temperature θ/θ_0 for $N = 2, 3$ degrees of freedom and the continuous limit $N \rightarrow \infty$. In the low-temperature limit δ is positive and diverges as $\delta(\theta) \sim 1/\theta$. At the tricritical temperature θ_{tc} it vanishes, $\delta(\theta_{tc}) = 0$ and becomes negative for $\theta > \theta_{tc}$. The negative δ indicates a first-order transition.

θ_{tc} , where Eq. (2.145) loses its validity. At θ_{tc} the first-order and second-order transition lines merge. In analogy to the classical theory of phase transitions it is called tricritical temperature [70, 71]. Above θ_{tc} the parameter δ becomes negative, indicating that the transition from rigid quantum to elastic quantum decay becomes first-order-like. The values of θ_{tc} are given in Table 2.1 for $N = 2, 3$ and $N \rightarrow \infty$. Note that θ_{tc} is smallest for $N = 3$ and increases monotonically with N for $N > 3$. Recall that θ_{tc} is largest for $N = 2$ due to the absence of \tilde{q}_2 in a system with only two degrees of freedom.

We now concentrate on the case where $\delta < 0$. Then in order to find the minimal values of S_E , we have to determine terms of the action $\propto \zeta^6$,

$$S_E(\zeta) = S_{qr} + g[(\alpha - \alpha_c)\zeta^2 + \delta\zeta^4 + \gamma\zeta^6], \quad (2.152)$$

which are obtained in the third iteration ($i = 3$) of the perturbation procedure. For $k \neq 1, 3$ one has $\tilde{q}_k^{(3)} = \tilde{q}_k^{(2)}$. Inverting the equations

$$\begin{aligned} \hat{Q}_1 \tilde{q}_1^{(3)} &= (4\tilde{q}_0^{(2)} + 2\sqrt{2}\tilde{q}_2^{(2)}) \zeta \psi_0(\tilde{\tau}), \\ \hat{Q}_3 \tilde{q}_3^{(3)} &= 2\sqrt{2}\zeta \psi_0(\tilde{\tau}) \tilde{q}_2^{(2)} \end{aligned}$$

N	2	3	∞
J_{tc}	0.8424	0.7652	0.7938
θ_{tc}	0.8719	0.8000	0.8275
$\delta'(\theta_{tc}/\theta_0)$	-2.274	-1.384	-1.675
$\gamma(\theta_{tc}/\theta_0)$	0.4118	0.2105	0.2698

Table 2.1: Numerical values of the tricritical current J_{tc} , tricritical temperature θ_{tc} , the derivative of the coefficient of the forth-order term $\delta'(\theta_{tc}/\theta_0)$ and the coefficient $\gamma(\theta_{tc}/\theta_0)$ of the sixth-order term for various numbers of degrees of freedom N .

numerically and inserting the values into

$$\begin{aligned}
\gamma = & \frac{1}{\zeta^6} \int_{-\pi}^{\pi} d\tilde{\tau} \left\{ -\sqrt{2}\zeta\psi_0(\tilde{\tau})q_2^{(2)}q_3^{(3)} \right. \\
& -\frac{2}{3}\left(q_0^{(2)}\right)^3 - \left(q_2^{(2)}\right)^2 \left(2q_0^{(2)} - \frac{\sqrt{2}}{3}\delta_{N,3}q_2^{(2)}\right) \\
& \left. - \left[q_1^{(3)} - \zeta\psi_0(\tilde{\tau})\right] \left[2q_0^{(2)} + \sqrt{2}q_2^{(2)}\right] \zeta\psi_0(\tilde{\tau}) \right\},
\end{aligned} \tag{2.153}$$

we calculate the coefficient $\gamma(\theta/\theta_0)$. Minimizing Eq. (2.152) with respect to ζ for $\alpha - \alpha_c < \delta^2/3\gamma$, one obtains, in addition to the rigid instanton solution with $\zeta = 0$, an elastic instanton solution with

$$\zeta^2 = \frac{\delta}{3\gamma} \left(-1 + \sqrt{1 - \frac{3\gamma}{\delta^2}(\alpha - \alpha_c)} \right). \tag{2.154}$$

The first-order transition occurs at $\alpha = \alpha_1 = \alpha_c + \delta^2/4\gamma$ when the nonuniform solution becomes the global minimum of the action, $S_E(\zeta) = S_E(0) = 0$.

Using the perturbation scheme, one could, in principle, determine the split-instanton solution to arbitrary order in ζ . For our discussion of the behavior of the decay rate close to the crossover from the single instanton to the split-instanton regime, the calculation shown above is sufficient.

2.4.6 Decay diagram and decay rate

In this section, we discuss the various decay regimes which are presented in the decay diagram (Fig. 2.11). Let us start with the thermal regime $\theta > \theta_0(J)$, where the decay occurs via thermal activation. For $J < 1$, the coupled degrees of freedom behave like a single degrees of freedom since the coupling energy is large compared to the thermal or the barrier energy. Then the system is in the rigid thermal regime. Increasing J , one enters the elastic thermal decay regime [77] passing the second-order crossover line at $J = 1$. On the other hand, starting in the thermal rigid phase and reducing θ , quantum fluctuations become important and at $\theta_0(J)$ a second-order crossover from thermal to quantum decay

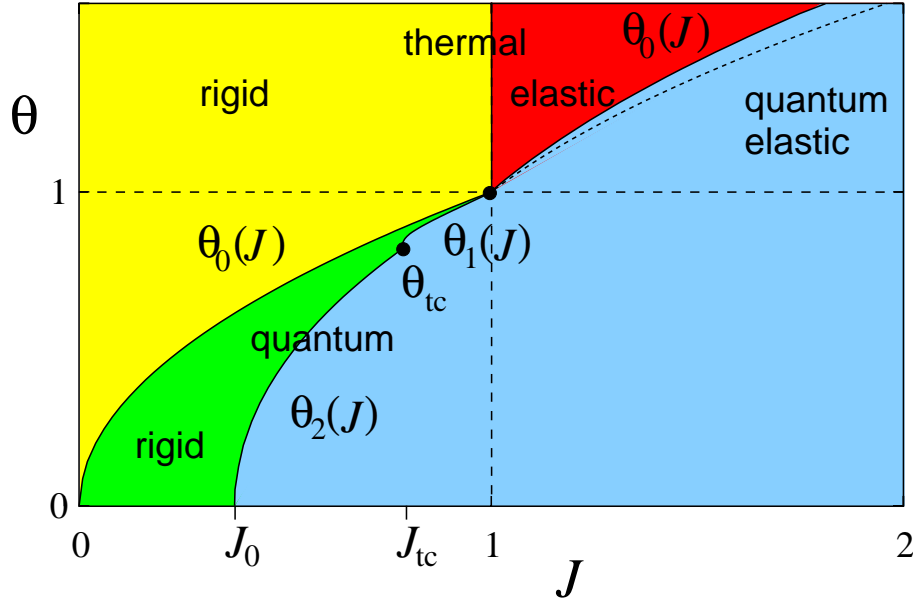


Figure 2.11: The decay diagram for $N = 3$ degrees of freedom in terms of the dimensionless current $J = \{3U_B\Delta/[2\kappa r^2 \sin^2(\pi/2N)]\}^2$ and the dimensionless temperature $\theta = \pi\eta k_B T/[2\hbar\kappa \sin^2(\pi/2N)]$. Criticality $I = NI_c$ corresponds to $J = 0$. Above $\theta_0(J)$ the system is in the thermal regime, and at $J = 1$ a second-order crossover from rigid to elastic thermal decay occurs. At $\theta_0(J)$ a second-order crossover from thermal to quantum decay takes place. The quantum regime $\theta < \theta_0$ is again separated into rigid and elastic decay. For $J_0 < J < J_{tc}$ the crossover from rigid to elastic decay at $\theta_2(J)$ is of second order. For $J_{tc} < J < 1$ the crossover indicated by $\theta_1(J)$ is first-order like. Though the diagram is similar for different N , the temperatures θ_{tc} , $\theta_1(J)$, and $\theta_0(J > 1)$ are altered. For comparison, the dashed curve shows $\theta_0(J > 1)$ for a dc SQUID ($N = 2$).

takes place [6]. Two characteristic currents, $J_0 = 0.3820$ and J_{tc} as given in Table 2.1 become important in the quantum regime. Below J_0 , the system preferably decays via the single instanton or rigid quantum saddle-point solution. For $J > J_0$ a transition from the rigid to the elastic quantum decay regime becomes possible. For $J_0 < J < J_{tc}$, the crossover is of second order and is caused by a saddle-point bifurcation of the Euclidean action occurring at $\alpha = \alpha_c$. The dimensionless crossover temperature is then given by

$$\theta_2 = (J + \sqrt{J} - 1)^{1/2}. \quad (2.155)$$

For $J_{tc} < J < 1$, the crossover is of first order. The transition occurs at $\alpha = \alpha_1$. Near θ_{tc} , we approximate $\delta \approx \delta'(\theta_{tc}/\theta_0)[(\theta - \theta_{tc})/\theta_0]$ and find that in this limit the crossover line is given by

$$\theta_1 = \theta_{tc} + \frac{2\gamma^{1/2}\theta_0}{\delta'(\theta_{tc}/\theta_0)}(\alpha - \alpha_c)^{1/2}. \quad (2.156)$$

The numerical values for γ , θ_{tc} , and $\delta'(\theta_{tc}/\theta_0)$ are given in Table 2.1. Note that since $\partial_\alpha\theta_1$ diverges as $\alpha \rightarrow \alpha_c$, the slope of $\theta_1(J)$ is infinite at the tricritical point. For $J > 1$ the

transition from the thermal to the quantum elastic region is again of second order. The crossover temperature is then given by $\theta_0(J > 1)$ [see Eq. (2.132)]. The decay diagram of an overdamped JJ array with $N = 3$ junctions presented here is similar to that of the dc SQUID with $N = 2$. Qualitatively, the diagrams exhibit the same features for all N . The reason is that for $J < 1$, the transition lines $\theta_0(J)$ and $\theta_2(J)$ are determined by the long-wavelength modes $q_0^{(0)}$ and \tilde{q}_1 , respectively, and hence are independent of N . However, there is a difference between the diagrams on a quantitative level, since θ_{tc} , $\theta_1(J)$ and $\theta_0(J > 1)$ are parametrized by N . For example, compared to the dc SQUID, the first-order transition region is enlarged for $N > 2$ and is the largest for $N = 3$.

It remains to discuss the decay rate $\Gamma \sim \exp(-S_B/\hbar)$ in the four regimes. To exponential accuracy, Γ is determined by the extremal of the action S_B , which is given by the Euclidean action S_E evaluated at the relevant saddle-point configuration \mathbf{x}_s , $S_B(J, \theta) = S_E[\mathbf{x}_s]$. The behavior of the rate in the thermal regime was discussed in Ref. [77]. Since the thermal saddle points \mathbf{x}_{ts} are independent of imaginary time, $S_B = \hbar V(\mathbf{x}_s)/T$ and the rate reduces to the classical Arrhenius form, $\Gamma \sim \exp(-V(\mathbf{x}_s)/T)$. In the thermal rigid regime S_B is given by

$$S_{tr} = \frac{2S_0}{3} \frac{\sqrt{J}}{\theta}, \quad J < 1. \quad (2.157)$$

Realizing that in the thermal regime $\delta = -(2/\lambda_0^{rs} + 1/\lambda_2^{rs})/(2\pi)$ and recalling that $\alpha = 1/\sqrt{J}$, one finds, with the help of Eq. (2.86), the thermal elastic result,

$$S_{te} = S_{tr} - g \frac{(\alpha - 1)^2}{4\delta}, \quad J \gtrsim 1. \quad (2.158)$$

In the rigid quantum regime, the action S_{qr} is given by Eq. (2.134). Inserting Eq. (2.154) into Eq. (2.152) we find the extremal action in the quantum elastic regime for $J < 1$,

$$S_{qe} = S_{qr} - \frac{g}{27\gamma^2} \left\{ 9\delta\gamma(\alpha - \alpha_c) - 2\delta^3 + 2[\delta^2 - 3\gamma(\alpha - \alpha_c)]^{3/2} \right\}, \quad (2.159)$$

where $\delta(\theta/\theta_0)$ is given by Eq. (2.151) and $\gamma(\theta/\theta_0)$ was calculated numerically using Eq. (2.153). The rates for various currents J are displayed in Fig. 2.12 as a function of temperature. For $J < J_0$ the system is in the rigid regime for all temperatures θ (see Fig. 2.11). For $\theta/\theta_0 > 1$ the thermal rigid result (2.157) applies. In the rigid quantum regime $\theta/\theta_0 < 1$, in comparison with the purely thermal result, the rate is increased due to quantum fluctuations according to Eq. (2.134). In the chosen representation S_{qr} is independent of system-specific parameters. Experimentally measured decay rates of rigid systems should thus collapse onto one curve. For $J > J_0$ tunneling of nonuniform instantons becomes possible and $B = S_{qe}$ is reduced further compared to S_{qr} . In Fig. 2.12 we displayed B for a system with $N = 3$ degrees of freedom. As an example for the behavior of the rate close to a second-order crossover to the split-instanton regime we chose $J = 0.6 < J_{tc}$. The

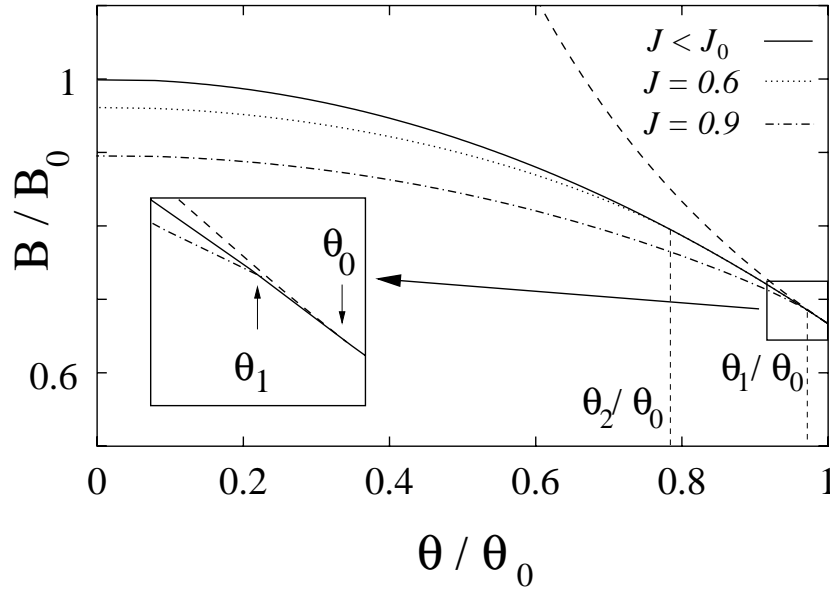


Figure 2.12: The extremal of the action B as a function of temperature θ for various normalized currents J . The dashed line shows the purely thermal behavior in the rigid regime. The rigid quantum result is represented by the solid line. The dotted and the dashed-dotted lines display B of a system with $N = 3$ degrees of freedom for $J = 0.6$ and $J = 0.9$, respectively. For $J = 0.6$ a second-order crossover to the split-instanton regime occurs at $\theta_2 = 0.790\theta_0$. A first-order crossover takes place for $J = 0.9$ at $\theta_1 = 0.975\theta_0$. The inset shows the cusplike shape of B close to θ_1 .

crossover occurs at $\theta_2 = 0.790\theta_0$. For $J = 0.9 > J_{tc}$, the behavior of the rate is different. The slope of S_{qe} changes abruptly at $\theta_1 = 0.975\theta_0$, which indicates the occurrence of a first-order crossover.

2.4.7 Discussions

In the present work, we studied the decay of metastable states in current-driven parallel coupled one-dimensional Josephson-junction arrays at zero voltage in the overdamped limit. We model this system by N elastically coupled degrees of freedom trapped in the minimum of the single-particle potential and interacting with a bath of harmonic oscillators. The escape from the trap can be induced by thermal or quantum fluctuations. Three energy scales determine the decay behavior of the system; the temperature, the barrier height of the trap and the interaction between the particles. Accordingly, one finds four different regimes for the decay rate which we summarized in a decay diagram in Fig. 2.11. To calculate the decay rate we use the thermodynamic method. In the saddle-point approximation, the decay is then determined by the most probable configurations leading to an escape from the trap which are given by the saddle points of the Euclidean action. In the thermal regime the saddle-point solutions are independent of the imaginary time and

identical to the saddle points of the potential energy [77]. If the interaction between the degrees of freedom is strong compared to the barrier energy, rigid configurations dominate the decay. Reducing the bias current, the barrier becomes larger and above a critical value the system preferably decays via an elastic configuration. On the other hand, starting in the rigid thermal regime and lowering the temperature, quantum fluctuations become important and the decay most probably occurs via the rigid quantum saddle-point or single-instanton solution of the Euclidean action [6]. Inside the quantum region, an elastic regime can again be entered by increasing the barrier above a critical value. In order to determine the nonuniform instanton solutions of the quantum elastic regime, we worked out an iterative perturbation procedure. We performed the calculations close to the crossover from rigid to elastic quantum decay analytically up to second order and realized the third-order calculation numerically. We were then able to give quantitative results for the decay rate including the quantum elastic regime. The behavior of the decay rate is similar for SQUID's, DJTL's, and long JJ's. In the rigid regime the decay occurs via a saddle point that is uniform in space and hence, the qualitative nature of thermal or quantum decay is not sensitive to the number of degrees of freedom. Further, the crossover from rigid to elastic decay is caused by the excitation of long-wavelength normal modes of the system, which are equivalent in the three physical systems discussed here.

We want to emphasize that although our conclusions are drawn for overdamped systems, the reasoning and the procedure also apply for the underdamped case. Indeed, on a qualitative level, the understanding of the quantum rigid-to-elastic crossover in underdamped DJTL's and long JJ's can be obtained on the basis of the theoretical work on SQUID's (Ref. [70]). However, in order to have quantitative results, one has to extend the theory following the scheme proposed here.

One interesting aspect of the quantum rigid-to-elastic crossover is that depending on the current, it can be either of first or second order, whereas all other crossovers that we discussed are of second order. Even more fascinating is the fact that this crossover is an intrinsic *quantum* property and can be regarded as one further evidence for macroscopic quantum tunneling, if measured. Experimental verifications of the predicted enhancement of the decay rate due to the elastic properties (see Fig. 2.12) are thus highly desirable. An experimental detection of the first-order-like crossover would be challenging, but seems to be difficult, because the cusplike behavior of the rate at the crossover is not very pronounced and occurs in a small current interval. In standard experiments, the rate is obtained from the switching current histogram. The current intervals of the histogram have to be much smaller than $\pi^4(1 - J_{tc})E_J^2/(2N^3L^2I_c)$ with $J_{tc} < 0.85$. Further, the number of events per interval has to be large in order to resolve the cusplike feature. It would be convenient to perform the measurements on systems with $N = 3$ degrees of freedoms since in this case the first-order region is the largest (see Fig. 2.11).

In sum, we calculated the decay rate of overdamped current-biased one-dimensional Josephson-junction arrays at zero voltage (including SQUID's, DJTL's, and long JJ's) analytically and numerically in several distinct decay regimes. An experimental observation of the predicted enhancement of the decay rate in the elastic quantum regime would give further evidence for macroscopic quantum tunneling in these systems.

Chapter 3

Plastic depinning transition in artificial vortex channels

In the last chapter we have studied thermal and quantum escape processes of driven interacting particles from a metastable state. The only way for the particles to leave the trap is to overcome the energy barrier that hampers their motion. When the drive is increased up to a certain threshold value, the barrier vanishes and metastability ceases to exist. This transition from a pinned to a moving state is called depinning transition. Depinning transitions occur in many physical systems and in various kinds of manners. In systems consisting of driven particles that interact with one another, the depinning transition becomes rather complex when disorder is present and is considered as a fundamental problem in non-equilibrium statistical mechanics.

A prominent physical system displaying a depinning transition is the vortex lattice in type-II superconductors. One can roughly distinguish between two types, namely elastic and plastic depinning. Whereas the former takes place via elastic deformations without destroying the topological order of the vortex lattice, in the latter case topological defects are formed which start to flow at the transition. In the past, a lot of research has been devoted to elastic depinning [36]. However, plastic depinning became a hot topic only recently [37, 38, 78]. Plastic depinning occurs in low dimensional samples. In the particular case of vortices in a two-dimensional (2d) strongly disordered superconductor, plastic depinning was observed in the form of quasi-1d filaments flowing through a static environment of pinned vortices [43, 45]. The formation of natural flow channels is typical for the plastic depinning process.

To obtain a more detailed understanding of the depinning process in disordered superconducting films, experimentalists fabricated *artificial* vortex channels [47, 48]. Investigations of these devices revealed that the critical current measured as a function of magnetic field displays oscillations that were not observed in natural channels. These features have been interpreted qualitatively in terms of commensurability effects between the vortex lattice in the channel and the lattice of the environment neglecting the effect of *disorder* [49]. In this chapter we study the effect of system boundaries and disorder on the depinning transition in the flow channels, but neglect *thermal* or *quantum* fluctuations that were

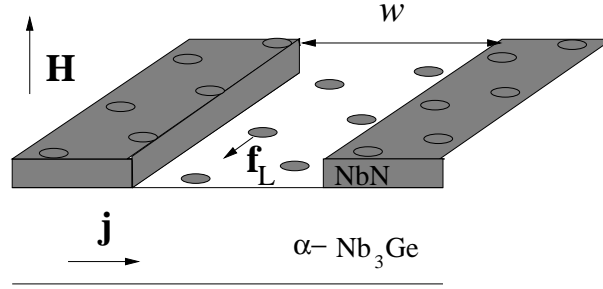


Figure 3.1: Schematic plot of the artificial flow channel geometry. The channels are manufactured by etching away the strongly pinning top layer material (grey area) in stripes of width w . Applying a magnetic field \mathbf{H} generates vortices. In the strong pinning area the vortices are static. Vortices in the weakly pinning channel are mainly pinned due to the interaction with the strongly pinned ones in the channel edges (grey area). In presence of a current density \mathbf{j} a Lorentz force \mathbf{f}_L acts on the vortices. At the depinning transition the channel vortices start to flow whereas the strongly pinned vortices in the channel environment remain static.

studied in the previous chapters. Since the London description of a vortex flow channel and its static environment is quite complex we were motivated to construct a simplified one-dimensional model which captures the essential physics of thin artificial vortex flow channels: we relate the London picture of a channel and its environment to a generalized disordered Frenkel-Kontorova model [50]. The characteristics of the model are studied partly analytically, but partly numerically and the above mentioned experimental results are compared to our theoretical findings.

3.1 Motivation

Let us now give a short overview about artificial vortex channels. A sketch of a typical device is presented in Fig. 3.1. The devices are manufactured by first absorbing a thin strongly pinning layer on top of a weakly pinning film and then etching away a few hundred channels of width w from the top layer. In the experiments cited above, the strongly pinning material is NbN and the weakly pinning one amorphous Nb₃Ge. To measure the effect of a single vortex lattice plane in the channel, the vortex lattice spacing, $a_0 = (4/3)^{1/4}(\Phi_0/B)^{1/2}$, is chosen to be of the order of the width w . Here, $a_0 \sim w \sim 100$ nm and the distance between the channels is 10 μm . Due to the material steps at the channel edges screening currents flow along the surface which interact with the vortices in the channels. As a consequence, the first rows of strongly pinned vortices near the channel edges are lined up at fairly straight along the channel, such that transversal shifts are negligible [79, 80]. The first rows along the channel edge opposite to each other have a distance $w + b_0 f_e(B/B_{c2})$, where $b_0 = a_0\sqrt{3}/2$ [see Fig. 3.2(a) for $f_e = 1$], $f_e(B/B_{c2}) \sim 1$ expresses the contribution of screening currents [79, 80], and B_{c2} is the upper critical mag-

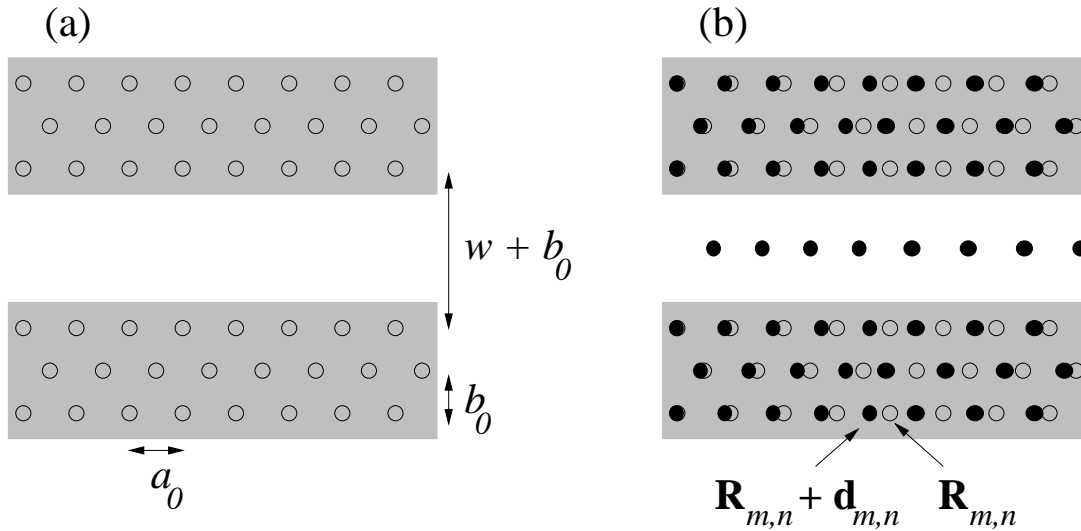


Figure 3.2: (a) Easy flow channel environment (shaded) in the absence of disorder. Vortex positions in the environment are marked by open circles. (b) Immobile vortices (dots) in the environment in the presence of weak disorder and one row of mobile vortices in the flow channel.

netic induction. Though transverse shifts of vortices in the strongly pinning neighborhood of the channel edge are suppressed due to screening currents, longitudinal displacements may occur due to thermal fluctuations or due to the presence of impurities in the superconducting material [see Fig. 3.2(b)]. In the channel pinning due to impurities is very weak. Below the depinning threshold, vortices in the channel are localized due to the interaction with the vortices in the static environment. In the presence of a current density \mathbf{j} , a Lorentz force \mathbf{f}_L acts on the vortices. As long as the vortices are pinned, the supercurrent is flowing dissipation-less through the sample. At a threshold force f_c the channel vortices depin and start to move. The vortex motion causes dissipation of energy and a voltage drop occurs across the sample boundaries. Hence, a well-defined critical current density j_c can be determined by measuring the current-voltage characteristics of the sample. Fig. 3.3 shows shear force density data deduced from current-voltage measurements by the Leiden group [81]. The oscillations in the shear force density F_s as a function of B are related to the (in)commensurability of the vortex lattice with channel width w . The maxima of F_s occur at integer values of the ration w/b_0 , where the vortex lattice spacing inside the channel is commensurate with the width of the channel. Compared to these values, F_s is reduced for non-integer w/b_0 . This can qualitatively be explained by the development of misfit dislocations along the channel edges [47, 48]. To obtain a quantitative description, let us now investigate a London type model for vortices inside and outside the channel.

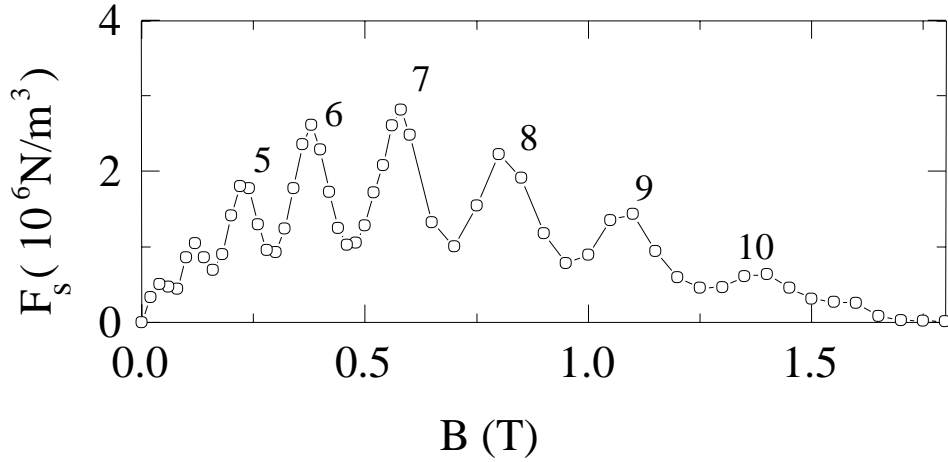


Figure 3.3: The critical shear force density F_s versus magnetic field B for a channel sample with $w \approx 330$ nm measured by the Leiden group [81]. The indices of the peaks indicate the number of mobile vortex rows in the channel.

3.2 A model for artificial vortex channels

Starting from a London description of vortices in a type-II superconductor, we now derive a simplified 1d model for vortices in an artificial easy-flow channel.

3.2.1 Channel with a perfect vortex lattice in the environment

Let us first consider a row of straight vortices that are aligned along the x -axis at positions $ma_0\mathbf{e}_x$, where m is an integer, a_0 the distance between adjacent vortices and \mathbf{e}_x the unit vector in the x -direction. In a type-II superconductor within London theory the interaction energy between two straight vortices of length l at \mathbf{r} and $\mathbf{0}$ is $U(\mathbf{r}) = U_0 K_0(r/\lambda)$, where $U_0 = \Phi_0^2 l / (8\pi^2 \lambda^2)$. Here λ is the penetration depth, $\Phi_0 = hc/2e$ is the flux quantum, and $l \gg \lambda$ the sample thickness. Then the potential energy $E_n^o(\mathbf{r})$ that is felt by a test vortex at position $\mathbf{r} = (x, y)$ interacting with a row of vortices placed at $nb_0\mathbf{e}_y$ is

$$E_n^o(\mathbf{r}) = \sum_m U(\mathbf{r} - \mathbf{R}_{m,n}) \quad (3.1)$$

where we introduced the lattice vectors $\mathbf{R}_{m,n} = ([m + n/2]a_0, nb_0)$ of a hexagonal lattice with $b_0 = \sqrt{3}a_0/2$. Fourier transforming and using the Poisson sum rule the latter can be recast into

$$E_n^o(\mathbf{r}) = \sum_\nu \frac{\cos[q_\nu(x - na_0/2)]}{2\pi a_0} \int dk_y e^{ik_y(y - nb_0)} \tilde{U}(q_\nu, k_y), \quad (3.2)$$

where $q_\nu = 2\pi\nu/a_0$ with integer ν and the Fourier transform of the potential is given by

$$\tilde{U}(q_\nu, k_y) = \frac{2\pi U_0}{q_\nu^2 + k_y^2 + \lambda^{-2}}. \quad (3.3)$$

Performing the integral over k_y leads to

$$E_n^o(\mathbf{r}) = \sum_{\nu} B_{\nu}(|y - nb_0|) \cos[q_{\nu}(x - na_0/2)], \quad (3.4)$$

where

$$B_{\nu}(y) = \frac{\pi U_0}{a_0 q'_{\nu}} e^{-q'_{\nu} y} \quad (3.5)$$

and $q'_{\nu} = \sqrt{q_{\nu}^2 + \lambda^{-2}}$.

We construct an easy flow channel by building a two dimensional vortex lattice, but leaving a region of width w along the x -axis empty (see Fig. 3.2).

If we consider a hexagonal vortex lattice in the channel environment, the potential in the channel is

$$E_{oc}(\mathbf{r}) = \sum_{n=1}^{\infty} [E_n^o(\mathbf{r} - \mathbf{b}/2) + E_{-n}^o(\mathbf{r} + \mathbf{b}/2)], \quad (3.6)$$

where $\mathbf{b} = (w - b_0)\mathbf{e}_y$. Summing over the vortex rows n one finds

$$E_{oc}(\mathbf{r}) = \sum_{\nu} A_{\nu}(y) \cos(q_{\nu} x), \quad (3.7)$$

the Fourier coefficients $A_{\nu}(y)$ read

$$A_{\nu}(y) = \frac{2 \cosh(q'_{\nu} y) B_{\nu}\left(\frac{w-b_0}{2}\right)}{(-1)^{\nu} e^{q'_{\nu} b_0} - 1}. \quad (3.8)$$

Since the magnetic inductions B used in the experiments cover the entire range up to the upper critical one B_{c2} , a more general expression for A_{ν} than the London limit that has been discussed until now is needed. However, the theory presented here can easily be extended to larger magnetic inductions. First one takes into account the finite diameter of the vortex core which is of the order ξ in the vortex-vortex interaction potential, $V \rightarrow U_0[K_0(r/\lambda) - K_0(r/\xi)]$. Second, one replaces $\lambda \rightarrow \lambda' = \lambda/(1 - B/B_{c2})^{1/2}$ and $\xi \rightarrow \xi' = \xi/(2 - 2B/B_{c2})^{1/2}$ to take into account the reduction of the superconducting order parameter at large magnetic fields [82]. We then obtain

$$A_{\nu}(y) = \frac{\pi U_0(1 - B/B_{c2})}{a_0} \left[\frac{2 \cosh(q'_{\nu} y) e^{-q'_{\nu} y(w-b_0)/2}}{q'_{\nu} [(-1)^{\nu} e^{q'_{\nu} b_0} - 1]} - \frac{2 \cosh(q''_{\nu} y) e^{-q''_{\nu} y(w-b_0)/2}}{q''_{\nu} [(-1)^{\nu} e^{q''_{\nu} b_0} - 1]} \right], \quad (3.9)$$

where now $q'_{\nu} = \sqrt{q_{\nu}^2 + (\lambda')^{-2}}$ and $q''_{\nu} = \sqrt{q_{\nu}^2 + (\xi')^{-2}}$.

3.2.2 Equation of motion

The overdamped dynamics of a vortex with index m at position \mathbf{r}_m inside the channel is described by

$$\eta \dot{\mathbf{r}}_m = f \cdot \mathbf{e}_x - \nabla E_{oc}(\mathbf{r}_m) - \sum_{n \neq m} \nabla U(\mathbf{r}_m - \mathbf{r}_n), \quad (3.10)$$

where $f = j\Phi_0/c$ is the magnitude of the Lorentz force that drives the vortices in presence of a current density j . The viscous drag coefficient η is related to the flux flow resistivity ρ_{ff} by $\eta = B\Phi_0/[c^2\rho_{ff}(B)]$. The sum is taken over the positions n of all other vortices inside the channel.

In the simplest case the channel width is $w \approx b_0$ such that only a single vortex row is inside the channel. Then the motion of the mobile vortices in the y -direction is essentially guided by the channel potential, whereas the interaction between vortices in the channel does not contribute significantly to the motion in the y -direction, $\eta\dot{y}_m \approx -\partial_y E_{oc}(\mathbf{r})$. However, the motion in the x -direction is determined by both the interactions between mobile vortices and the gradient of the channel potential. To simplify matters, we neglect the motion in the y -direction, $y_m = 0$, such that the equation of motion can be simplified to a one-dimensional one. Further, we restrict our considerations to $\lambda \gtrsim a_0$ as in a typical experiment. Then, the amplitudes $A_\nu(0)$ fall off exponentially fast, $A_\nu(0) \sim U_0 \exp(-\pi\sqrt{3}\nu)$, and the approximation to consider only the first harmonic $q = q_1 = 2\pi/a_0$ of the channel potential is a good one. Introducing $\mu = 2q|A_1(0)|$, and restricting the interaction between vortices in the channel to next-neighbor spring-like forces, the equation for the overdamped longitudinal motion reads

$$\eta\dot{x}_m = -\frac{\partial V}{\partial x_m}, \quad (3.11)$$

where the potential energy of the vortices in the channel is given by

$$V = \sum_m \left\{ \frac{\mu}{q} [1 - \cos(qx_m)] - fx_m + \sum_n \frac{\kappa_n}{2} (x_{m+n} - x_m - na)^2 \right\}. \quad (3.12)$$

It has the form of a generalized Frenkel-Kontorova model (FKM) [50]. The interactions between vortices inside the channel are approximated by Hookian springs with spring constants $\kappa_n = (U_0/\lambda^2)K_0''(na/\lambda)$, where the double prime denotes the second derivative. Here, $a = \Phi_0/(wB)$ is the preferred distance of vortices in the channel, which is a function of the channel width w and the magnetic induction B . This is not to be mixed with the true average vortex spacing inside the channel which we denote \tilde{a} and which is a function of a .

The FKM has been intensively studied close to equilibrium, $f \sim 0$, see Ref. [83]. The reduced dimensionless elasticity

$$g = \frac{1}{q\mu} \sum_{n=1}^{\infty} n^2 \kappa_n \approx \frac{e^{\pi\sqrt{3}} \lambda}{8\pi} \frac{1}{a} \gg 1 \quad (3.13)$$

together with the winding number $\tilde{\Omega} = \tilde{a}/a_0$ crucially determine the behavior of the model. For rational $\tilde{\Omega}$ the vortex chain is commensurate with the periodic channel potential whereas for irrational $\tilde{\Omega}$ it is in an incommensurate state. The transition from a commensurate to an incommensurate state is called commensurate-incommensurate transition (CIT). It is a continuous transition that occurs at finite mismatches $\chi = (a - a_0)/a_0$, since the creation of discommensurations costs energy.

Since we are most interested in the regime $g \gg 1$, it is convenient to study the model in the continuum limit. Further, we take into account the finite length of the system and consider open boundary conditions. Rewriting Eq. 3.12 in terms of the displacements of the vortices from the lattice positions, $u_m = x_m - ma_0$ and substituting $ma_0 \rightarrow x$, $u_m \rightarrow u(x)$, $(u_{m+n} - u_m)/(na_0) \rightarrow \partial_x u(x)$, $\sum_m \rightarrow \int dx/a_0$, we obtain the continuum equation of motion

$$\eta \dot{u}(x) = -a_0 \frac{\delta V[u]}{\delta u(x)} = \tilde{\kappa} \frac{\partial^2 u(x)}{\partial x^2} - \mu \sin[qu(x)] + f + \tilde{\kappa} \chi [\delta(x-L) - \delta(x)], \quad (3.14)$$

where we have introduced $\tilde{\kappa} = 2\pi a_0 \mu g$ and the last term is an effective surface force that arises at the open sample boundaries in the presence of frustration. The energy functional reads

$$V[u] = a_0^{-1} \int_0^L dx \left\{ \frac{\tilde{\kappa}}{2} \left(\frac{\partial u}{\partial x} - \chi \right)^2 + \frac{\mu}{q} [1 - \cos(qu)] - fu \right\}. \quad (3.15)$$

It can be decomposed into

$$V = V_{SG} + V_\chi + V_0, \quad (3.16)$$

where

$$V_{SG}[u] = a_0^{-1} \int_0^L dx \left\{ \frac{\tilde{\kappa}}{2} \left(\frac{\partial u}{\partial x} \right)^2 + \frac{\mu}{q} [1 - \cos(qu)] - fu \right\} \quad (3.17)$$

is the energy functional of the Sine-Gordon model (SGM),

$$V_\chi[u] = -a_0^{-1} \tilde{\kappa} \chi [u(L) - u(0)] \quad (3.18)$$

is the frustration energy due to the mismatch χ determined by the values of the displacement field $u(0)$ and $u(L)$ at the boundaries, and V_0 is an irrelevant offset that is omitted in the following.

3.2.3 Commensurate-Incommensurate Transition

We now shortly review the CIT. Then we extend the picture to discuss the role of edge barriers for defects in finite systems, which is crucial to understand how discommensurations penetrate a sample in the absence of thermal or quantum fluctuations.

The extrema of $V[u]$ are found solving the variational problem $\delta V/\delta u = 0$. In the absence of frustration, $\chi = 0$, for $f < \mu$ uniform static solutions exist. They are the stable and unstable solutions of the SGM [84]

$$u_{s,n} = a_0 n + q^{-1} \arcsin(f/\mu) \quad (3.19)$$

and

$$u_{u,n} = \frac{(2n+1)a_0}{2} - q^{-1} \arcsin(f/\mu), \quad (3.20)$$

respectively. The non-trivial solutions of the SGM are kinked. In absence of the driving force $f = 0$ the one-kink solution centered at x_c reads

$$u_{k,n}(x; x_c) = u_{s,n} + \frac{4}{q} \arctan \left[\exp \left(\frac{x - x_c}{l_d} \right) \right], \quad (3.21)$$

where $l_d = a_0 \sqrt{g}$ is the width of the kink. The corresponding anti-kink solution reads $u_{a,n}(x; x_c) = u_{k,n}(-x; -x_c)$. The CIT is a transition that occurs in equilibrium ($f = 0$) when it becomes energetically favorable to have a finite density of discommensurations in the system. Neglecting effects of system boundaries, the mismatch χ_{ci} at which the CIT takes place is then quickly found by comparing the energy of the kinked solution with the energy of the stable homogeneous one $V[u_{k,n}] - V[u_{s,n}] = (4/\pi)(\tilde{\kappa}\mu/q)^{1/2} - \tilde{\kappa}\chi = 0$,

$$\chi_{ci} = \frac{4}{\pi} \left(\frac{\mu}{q\tilde{\kappa}} \right)^{1/2} = \frac{2}{\pi^2 \sqrt{g}}. \quad (3.22)$$

Though at the CIT $u_{k,n}$ or $u_{a,n}$ have the same energy as $u_{s,n}$, a barrier has to be overcome in order to make the transition from $u_{s,n} \rightarrow u_{k,n}$ or $u_{s,n} \rightarrow u_{a,n}$. In the absence of fluctuations, as considered here, discommensurations can only enter the system when this barrier vanishes. In general, the barrier vanishes at a sufficiently strong frustration or driving force. We therefore define a threshold frustration $\chi_c(f)$, which is a function of the driving force f . Finite driving forces $f > 0$ are considered in Section 3.2.4, where depinning is studied. In the following we investigate how (anti-)kinks enter the system at equilibrium $f = 0$ and determine the zero-force threshold $\chi_c(0)$.

Let us first determine the energy that is needed to deform a uniform state into a kinked one. We note that due to frustration kinks can only be created spontaneously at the system boundaries, $x = 0$ or $x = L$. Of course, in the presence of thermal fluctuations, quantum fluctuations, or quenched disorder, deep in the bulk kinks can in principle be created in the form kink-anti-kink pairs. However, in the absence of fluctuations as considered here this is not possible. The reason is that kink-anti-kink pairs cannot gain frustration energy for a spontaneous kink emergence, since $u(0) = u(L) = u_{s,n}$ and hence $V_\chi = 0$. Thus, (anti-)kinks can only enter the system at $x = 0$ and $x = L$. In the following we discuss the penetration of an anti-kink at $x = 0$, having in mind that the same holds for $x = L$ and for kinks. Note that in a finite system with boundaries at $x = 0$ and $x = L$ one has $\lim_{x_c \rightarrow -\infty} u_{a,n}(0; x_c) = u_{s,n}$. Hence, a deformation from $u_{s,n}$ to $u_{a,n}$ can be achieved by pushing an anti-kink centered at x_c from $x_c = -\infty$ to $x_c > 0$. The energy of the anti-kink solution relative to the uniform one as a function of center coordinate x_c is then

$$\begin{aligned} \Delta V(x_c) &= V[u_{a,n}(x; x_c)] - V[u_{s,n}(x)] \\ &= a_0^{-1} \tilde{\kappa} \left\{ \chi[u_{a,n}(0; x_c) - u_{a,n}(L; x_c)] + \int_0^L dx \left[\frac{\partial u_{a,n}(x; x_c)}{\partial x} \right]^2 \right\} \end{aligned}$$

Since the tail of the kink falls off exponentially, we can neglect the influence of the boundary

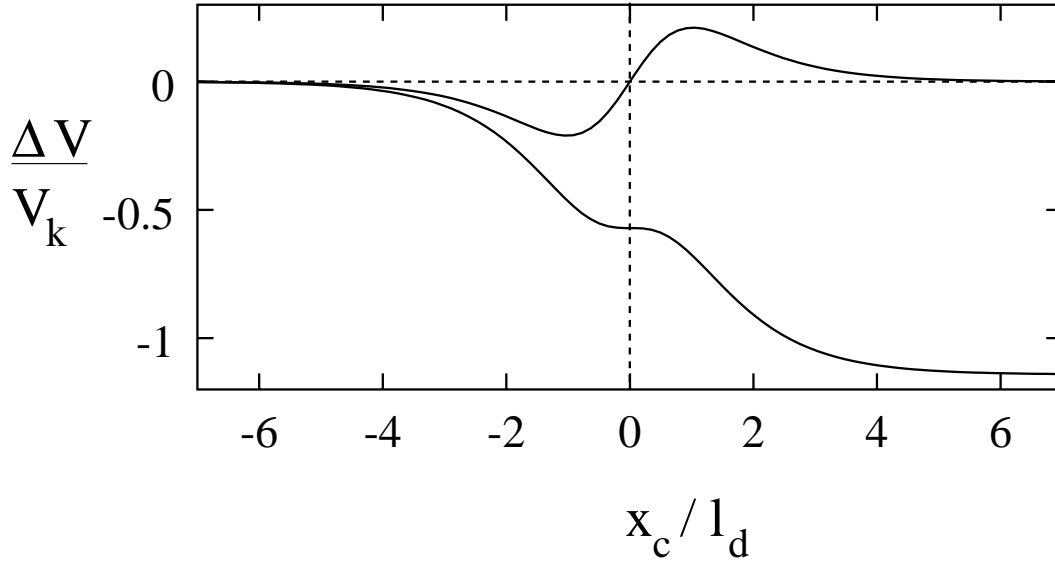


Figure 3.4: Potential energy of an (anti-)kink ΔV in units of $V_k = \tilde{\kappa}\chi_{ci}/2$ as a function of the (anti-)kink center x_c . Displayed are values close to the system boundary at $x = 0$ for frustration parameters $|\chi| = \chi_{ci}$ (upper curve) and $|\chi| = \chi_c(0)$ (lower curve). At the classical CIT, where $|\chi| = \chi_{ci}$, an entry barrier has to be overcome with the help of fluctuations to make a transition from $u_{s,n}$ to $u_{k,n}$ or $u_{a,n}$. The entry barrier vanishes at $|\chi| = \chi_c(0)$ where (anti-)kinks can penetrate the system.

at $x = L \gg l_d$. For simplicity, we then consider a semi-infinite system, $L \rightarrow \infty$, and obtain

$$\Delta V(x_c) = \frac{\tilde{\kappa}\chi_{ci}}{2} \left\{ \frac{4}{\pi} \frac{\chi}{\chi_{ci}} \arctan \left[\exp \left(\frac{x_c}{l_d} \right) \right] + 1 + \tanh \left(\frac{x_c}{l_d} \right) \right\}. \quad (3.23)$$

Minimizing ΔV with respect to x_c we find a minimum at

$$x_{c,1} = l_d \ln \left(-\frac{\pi\chi_{ci}}{2\chi} - \sqrt{\frac{\pi^2\chi_{ci}^2}{4\chi^2} - 1} \right) \quad (3.24)$$

and a maximum at

$$x_{c,2} = l_d \ln \left(-\frac{\pi\chi_{ci}}{2\chi} + \sqrt{\frac{\pi^2\chi_{ci}^2}{4\chi^2} - 1} \right). \quad (3.25)$$

At the frustration

$$\chi = -\chi_c(0) = -\frac{\pi}{2}\chi_{ci} = -\frac{1}{\pi\sqrt{g}}, \quad (3.26)$$

the minimum and the maximum merge into a saddle point at $x_c = 0$ where the entry barrier vanishes and an anti-kink flows freely into the system. It is interesting to note that for $\chi < 0$ the minimum of the anti-kink energy relative to the uniform solution is always

negative, $\Delta V(x_{c,1}) < 0$. This means that in a frustrated system the uniform solution $u_{s,n}$ is unstable in the presence of a boundary. Instead, the stable solution is a virtual anti-kink with a center x_c localized outside the system at $x_{c,1} < 0$. At the boundary, the chain thus tries to adapt optimally to the frustration to reduce its energy. For $\chi = -\chi_c(0)$ one finds $x_c = 0$, which means that half of the kink is already inside the system and that it can gain more energy by sliding towards the center of the system. The scenario is the same for an anti-kink entering the system at $x = L$. For a kink the description given above is identical except that $\chi > 0$. The kink entry barrier vanishes at $\chi = \chi_c(0)$.

The picture of the CIT is thus drastically modified in the presence of system boundaries when there are no physical mechanisms like thermal or quantum fluctuations that are needed to cross the edge-barrier. In fact, since in the absence of fluctuations a system with boundaries remains commensurate for $|\chi| < \chi_c(0)$, we identify the threshold at $|\chi| = \chi_c(0)$ with the CIT of a finite, purely mechanical system.

3.2.4 Depinning in the presence of boundaries

In the following we investigate how the chain inside the channel actually depins in presence of a driving force, $f > 0$. In the simplest case, for $w = b_0$, we have a commensurate state without frustration, $\tilde{a} = a = a_0$ and $\chi = 0$. The chain locks perfectly to the potential and the threshold depinning force as a function of χ is

$$f_c(0) = \mu. \quad (3.27)$$

If the system is frustrated, $b_0 \neq w$, depinning occurs via mobile discommensurations which in the SGM are represented by kinks or anti-kinks. As in the equilibrium case, for finite driving forces discommensurations enter the system when their entry barrier vanishes. Whether they are mobile or not depends on further barriers that may exist in the bulk.

In the continuous limit as discussed here, the defective state is not pinned. Hence, in the continuum model the threshold $\chi_c(0)$ indicates the change from a static equilibrium ground state ($u_{s,n}$) to a mobile one ($u_{k,n}$ or $u_{a,n}$). However, if the discreteness of the chain is taken into account, Peierls-Nabarro barriers may exist. The Peierls-Nabarro is the energy barrier that has to be overcome for a translation, $x_m \rightarrow x_{m+1}$. Whereas this barrier is always finite for rational $\tilde{\Omega}$, it may vanish in the incommensurate state: if g is lower than a critical value, $g_c(a/a_0)$, the incommensurate state is pinned, however, for $g > g_c(a/a_0)$, the Aubry transition to a sliding state with truly vanishing critical force takes place [85]. For pinned defective configurations the Peierls-Nabarro barrier, which determines the corresponding pinning force f_{PN} , depends on g . Large $g \gg 1$ imply that an isolated defect having a size $\sim l_d$ extends over several lattice constants. Then, the Peierls-Nabarro barrier is nearly vanishing [83] and the pinning force is

$$f_{PN} \approx 64\pi^2 g \mu \exp(-\pi^2 \sqrt{g}). \quad (3.28)$$

Since $f_{PN} \ll 10^{-4} \mu$ we neglect it in the following.

Note that an exit barrier exists for a *single* kink at the other boundary (imagine the mirror image of the entry barrier as shown in Fig 3.4 at the other end of the system). However, the exit barrier becomes irrelevant in the presence of further kinks. This can be easily understood by the following argument. Suppose a kink enters the system, freely flows to the other end, and then becomes trapped by the exit barrier. Then a second kink follows and interacts with the first one. If it would move “adiabatically” it would become trapped by the interaction with the first kink, which mediates the pinning force. However, the first kink would experience the interaction of the second kink, too. The resulting interaction force is of the same magnitude as the pinning force, but of opposite sign. Hence, the total force is zero and the first kink is released. The second becomes pinned for a while until released by the third and so forth. For non-adiabatically moving kinks, the successor does not even become pinned by the predecessor, it only lowers its velocity before the predecessor escapes due to the kink-kink interaction and the successor becomes pinned at the boundary.

So far we have determined the frustration strength $\chi_c(0)$ above which discommensurations enter the system in the absence of a driving force, $f = 0$. In the presence of a driving force f , we can roughly distinguish between the regime above equilibrium threshold, $|\chi| > \chi_c(0)$, and below equilibrium threshold $|\chi| < \chi_c(0)$.

Above equilibrium threshold, $|\chi| > \chi_c(0)$, depending on the sign of χ , kinks or anti-kinks are present in the system, since the entry barrier for discommensurations has vanished. Neglecting the effects of the Peierls-Nabarro barriers, the threshold force has basically vanished,

$$f_c \approx 0. \quad (3.29)$$

For $|\chi| < \chi_c(0)$ there are no kinks present in the system at equilibrium due to the finite entry barrier. However, at a sufficiently large driving force, the entry barrier vanishes, too. Then discommensurations enter the system at one boundary, freely flow through it and exit at the other boundary. In presence of a force the formation of kinks is similar to the kink-penetration at equilibrium we discussed in Section 3.2.3. Of course, the extremal solutions which determine the energy barrier for kink formation are different.

For frustrations close to the equilibrium threshold frustration, $\chi_c(0) - |\chi| \ll \chi_c(0)$, the depinning threshold force is small, $f_c \ll \mu$. Let us study the depinning of an anti-kink at the left boundary $x = 0$ for negative frustrations, $\chi < 0$, in the presence of a small force, $0 < f \ll \mu$. In the low-force limit, we can neglect the deformation of the anti-kink due to the force. The energy of the driven anti-kink relative to the uniform solution as a function of the anti-kink center x_c is then

$$\Delta V(x_c) \approx \frac{\tilde{\kappa}\chi}{a_0} [u_{a,n}(0; x_c) - u_{a,n}(L; x_c)] + \frac{1}{a_0} \int_0^L dx \left\{ \tilde{\kappa} \left[\frac{\partial u_{a,n}(x; x_c)}{\partial x} \right]^2 - f u_{a,n}(x; x_c) \right\}$$

If we neglect the presence of the other boundary at $x = L$, the derivative of the potential with respect to x_c is

$$\frac{d}{dx_c} \Delta V(x_c) \approx -\frac{\tilde{\kappa}}{a_0} \frac{\partial u_{a,n}(0; x_c)}{\partial x_c} \left[\chi + \frac{\partial u_{a,n}(0; x_c)}{\partial x_c} \right] + \frac{f}{a_0} u_{a,n}(0; x_c) \quad (3.30)$$

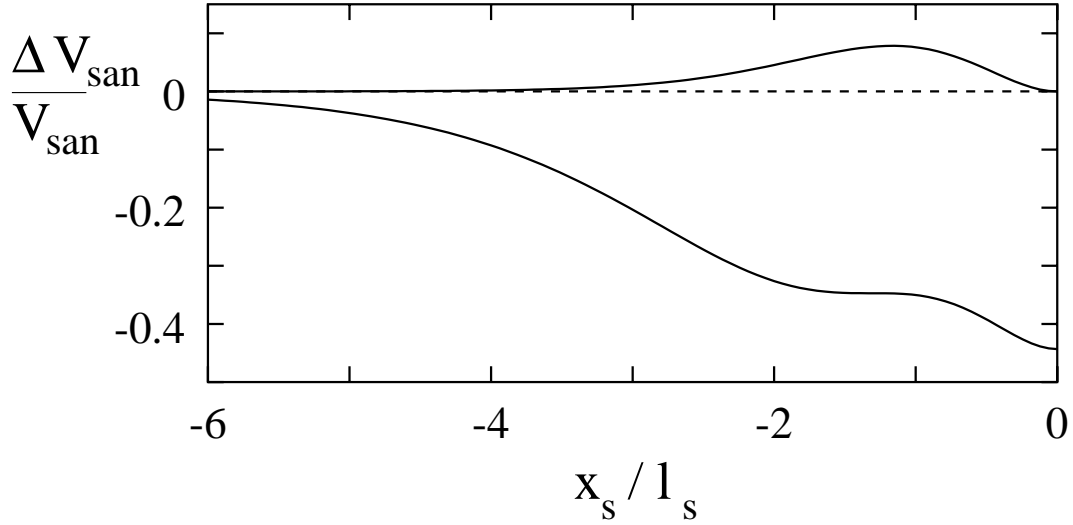


Figure 3.5: Potential energy of a small amplitude nucleus ΔV_{san} in units of $V_{san} = 4\tilde{\kappa}a_s^2/15a_0l_s$ as a function of the position x_s of the maximum amplitude. Shown are values close to the system boundary at $x = 0$ for frustration parameters $\chi = -2\sqrt{3}\chi_c(f)/5$ (upper curve) and $\chi = \chi_c(f)$ (lower curve), where the barrier vanishes.

The anti-kink depins at the left boundary when the maximum slope of the potential at $x_c = 0$ vanishes. This occurs at the threshold force

$$f_c = \frac{4\mu}{\pi} \left[1 - \frac{|\chi|}{\chi_c(0)} \right], \quad (3.31)$$

which is easy to show realizing that $u_{a,n}(0;0) = a_0/2$, $\partial_{x_c} u_{a,n}(0;0)/\partial x_c = \chi_c(0)$, and $\mu = \pi\tilde{\kappa}\chi_c^2(0)/(2a_0)$. The same result is found for kink depinning at the other boundary, $x = L$, for positive frustration, $\chi > 0$.

At low frustration, $|\chi| \ll \chi_c(0)$, the depinning threshold f_c is close to μ . One thus has to consider the large force regime, $\mu - f \ll \mu$, where the lowest energy saddle-point solution of the SGM $u_{san,n}(x; x_s) = u_{s,n} + \Delta u(x; x_s)$ has a small amplitude and hence is called small amplitude nucleus (SAN). It can be calculated by approximating the tilted cosine potential by a cubic parabola (see in Section 2.2),

$$\Delta u(x; x_s) = a_s \cosh^{-2} \left[\frac{x - x_s}{2l_s} \right], \quad (3.32)$$

with center x_s , amplitude $a_s = 3q^{-1}[2(1 - f/\mu)]^{1/2}$, and width $l_s = l_d[2(1 - f/\mu)]^{-1/4}$.

Let us now consider the penetration of an anti-kink for $\chi < 0$ at the boundary $x = 0$. The energy difference $\Delta V_{san} = V[u_{san,n}] - V[u_{s,n}]$ as a function of $x_s \leq 0$ is

$$\Delta V_{san}(x_s) = \frac{4\tilde{\kappa}a_s^2}{15a_0l_s} \left\{ - \left[\frac{3\Delta u(0, x_s)}{2a_s} + 1 \right] \left[1 - \frac{\Delta u(0, x_s)}{a_s} \right]^{3/2} + 1 + \frac{5}{2\sqrt{3}} \frac{\chi}{\chi_c(f)} \frac{\Delta u(0, x_s)}{a_s} \right\},$$

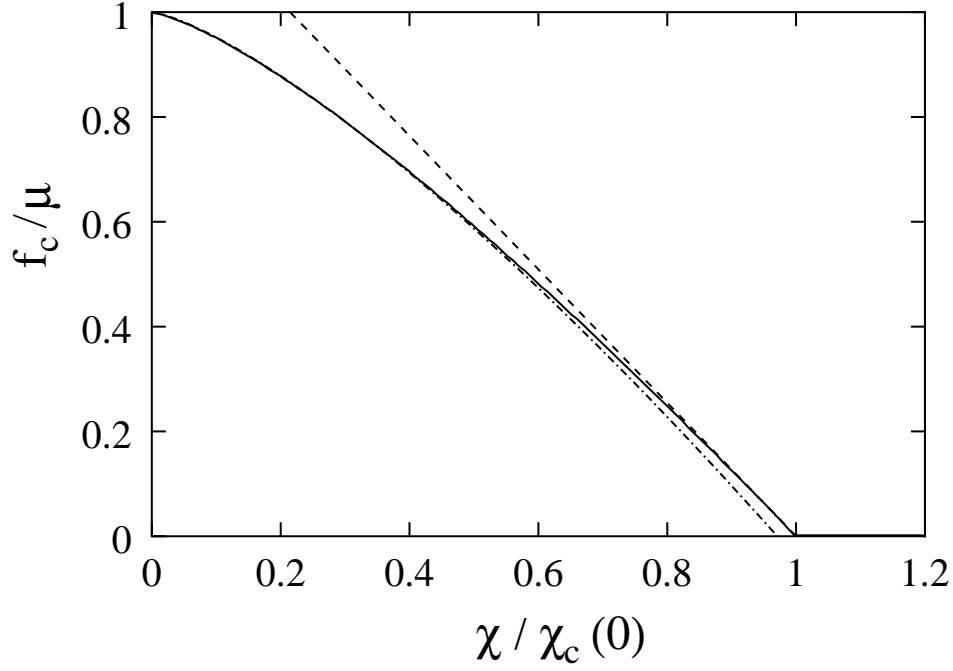


Figure 3.6: Critical force f_c as a function of the mismatch parameter χ . Shown are the numerical integration results (solid line), high force approximation $f_c - \mu \ll \mu$ (dashed-dotted line) and the low force approximation $f_c \ll \mu$ (dashed line).

where

$$\chi_c(f) = \frac{\pi \chi_{ci}}{2\sqrt{3}} \left[2 \left(1 - \frac{f}{\mu} \right) \right]^{3/4}. \quad (3.33)$$

As shown in Fig. 3.5, the SAN potential $\Delta V_{san}(x_s)$ has a barrier which vanishes at $\chi = -\chi_c(f)$. This can be seen by analyzing the zeros of the derivative

$$\frac{d}{dx_s} \Delta V_{san}(x_s) = \frac{\tilde{\kappa} a_s}{a_0 l_s} \frac{\partial \Delta u(0, x_s)}{\partial x_s} \left\{ \frac{\Delta u(0, x_s)}{a_s} \left[1 - \frac{\Delta u(0, x_s)}{a_s} \right]^{1/2} + \frac{2}{3\sqrt{3}} \frac{\chi}{\chi_c(f)} \right\}. \quad (3.34)$$

One zero is given by $x_s = 0$, where the partial derivative $\partial \Delta u(0, x_s) / \partial x_s$ vanishes. The others can in principle be found by studying the term in the curly brackets which becomes zero if

$$\left[\frac{\Delta u}{a_s} \right]^2 \left[1 - \frac{\Delta u}{a_s} \right] = \frac{4}{27} \left[\frac{\chi}{\chi_c(f)} \right]^2. \quad (3.35)$$

However, to find the threshold condition, we do not need to calculate x_s explicitly, it is sufficient to determine $\Delta u(0; x_s)$. Equation (3.35) has got at most three roots, depending on the value of $\chi^2 > 0$. One of the roots is negative, which is no solution, since $0 < \Delta u \leq a_s$ [see Eq. (3.32)]. For $-\chi_c(f) < \chi < 0$ there are two positive roots, which indicate the existence of two extrema of ΔV_{san} , a minimum and a maximum. Calculating the extrema

of Eq. (3.35) with respect to Δu , one sees that at $\chi = -\chi_c(f)$ the positive roots of Eq. (3.35) become degenerate, which means that the minimum and the maximum merge into a saddle point of ΔV_{san} . Hence, the entry barrier of the SAN vanishes. At this value, $\Delta u = 2a_s/3$. Thus, two thirds of a SAN are localized at the left boundary, $x = 0$, but are unstable against small perturbations. Increasing either χ or f depins the SAN which then evolves into a full anti-kink. Finally, from $\Delta u(0; x_s) = 2a_s/3$ we find $x_s = l_s \ln(2 - \sqrt{3})$.

To summarize, for low frustrations $|\chi| \ll \chi_c(0)$ and for frustrations close to the equilibrium threshold $\chi_c(0) - |\chi| \ll \chi_c(0)$ the threshold force f_c is given by

$$f_c \approx \begin{cases} \mu \left\{ 1 - \frac{3^{2/3}}{2} \left[\frac{|\chi|}{\chi_c(0)} \right]^{4/3} \right\} & |\chi| \ll \chi_c(0) \\ \frac{4}{\pi} \mu \left[1 - \frac{|\chi|}{\chi_c(0)} \right] & \chi_c(0) - |\chi| \ll \chi_c(0) \\ 0 & |\chi| \gtrsim \chi_c(0). \end{cases} \quad (3.36)$$

For completeness, we calculated the threshold force for arbitrary frustration by numerical integration. To calculate the static and dynamic solutions of Eq. (3.14), we use a standard numerical integration procedure. Starting with a flat initial configuration, $u_m = 0$, we iterate

$$u_m(t + \delta t) = u_m(t) + \delta t v_m(t), \quad (3.37)$$

with

$$v_m(t) = f + \sin[2\pi u_m(t)] + 2\pi g[u_{m+1}(t) + u_{m-1}(t) - 2u_m(t) + \delta_{m,M} - \delta_{m,1}]$$

where length is measured in units of a_0 , time in units of $t_0 = a_0\eta/\mu$, and force in units of μ . The length of the system is $M = L/a_0$. Recalling that the vortex-vortex interaction energy falls off exponentially fast for distances between vortices larger than λ , we take only the $N = [5\lambda/a_0]$ next neighboring vortices into account in the sum over channel vortices. The channel has a length of L . At its ends, we apply boundary conditions taking into account the frustration, χ . For a given force, Eq. (3.37) is iterated until a fairly steady state is reached, $[v_m(t + \delta t) - v_m(t)]/\delta t < 10^{-4}$. Channel vortices are defined to be static, if $v_m < 10^{-8}$. The calculated $u_m(t)$ and $v_m(t)$ are recorded for several forces. In addition we can record the particle trajectories $x_m(t)$ to visualize the dynamical behavior of the channel vortices close to the depinning transition. The numerical results and the analytical limits for $f_c(\chi)$ are shown in Fig. 3.6.

The numerical integration also allows to determine the velocity averaged over time and space,

$$v = \frac{a_0}{L} \sum_{m=1}^L \int_0^T \frac{dt}{T} \dot{u}_m(t), \quad (3.38)$$

as a function of the force f as shown in Fig. 3.7.

Above $\chi_c(0)$ where the entry barrier has vanished the topological defects move freely through the sample. The linear force-velocity characteristics resembles to the one of a

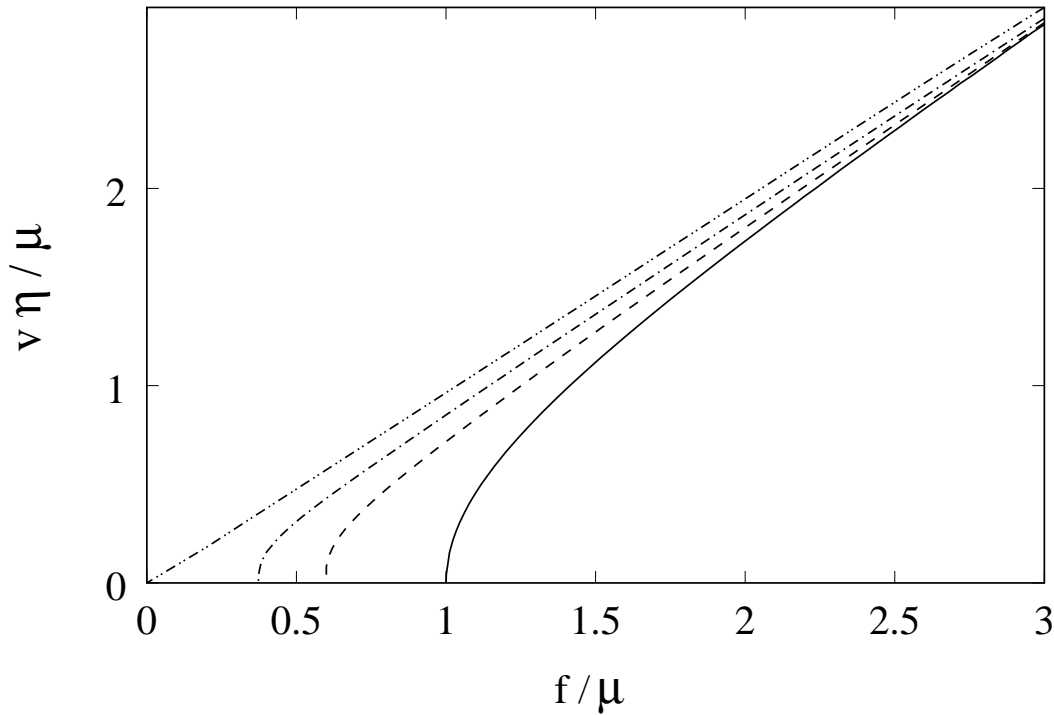


Figure 3.7: Typical $f - v$ curves computed for systems with $L = 1000a_0$ and $\lambda = a_0$. The result for the unfrustrated commensurate case, $\chi = 0$ (solid line), is identical to the curve of a single particle in a sinusoidal potential, $v \sim (f - \mu)^\nu$ with $\nu = 1/2$. Frustration lowers the threshold force f_c , but does not alter the exponent ν in the commensurate regime. However, in the incommensurate state, $|\chi| > \chi_c(0)$, the $f - v$ curve becomes linear, $v \sim f$. Shown are the $f - v$ characteristics for frustrated systems with $\chi = \chi_c(0)$ (dash-dot-dotted), $0.7 \chi_c(0)$ (dash-dotted), and $0.5 \chi_c(0)$ (dashed).

single free particle with dissipative dynamics, $v = f/\eta$. The velocity of the entire chain is determined by the velocity of the defects that enter the system at the boundary. At $|\chi| = \chi_c$, where the entry barrier for defects has vanished, $\partial_x^2 u(x=0, L) = 0$. This means that close to the maximum of the sinusoidal potential, where the chain bead spends most of the time, it effectively behaves like a single particle which is driven by a force f . For $|\chi| > \chi_c$ a similar argument can be given. At $f = 0$ the effective force at the system boundary pushes defects into the channel until their density is so high, that their repulsion prevents new defects to flow in. Effectively, the chain bead at the boundary reaches an unstable equilibrium. Driving the system now with a non-zero force $f > 0$ results in the same motion for the bead at the boundary as for $|\chi| = \chi_c$.

For $\chi < \chi_c(0)$ the entry barrier for the defects becomes relevant and the force-velocity characteristics shows the behavior typical for quasi-particles with a vanishing saddle-point barrier with $v \sim [f - f_c(\chi)]^{1/2}$ for $f \rightarrow f_c$. Finally, in the absence of frustration the particles depin instantly and $v = (f_c/\eta)(2f/f_c - 2)^{1/2}$ like a single particle in a sinusoidal potential.

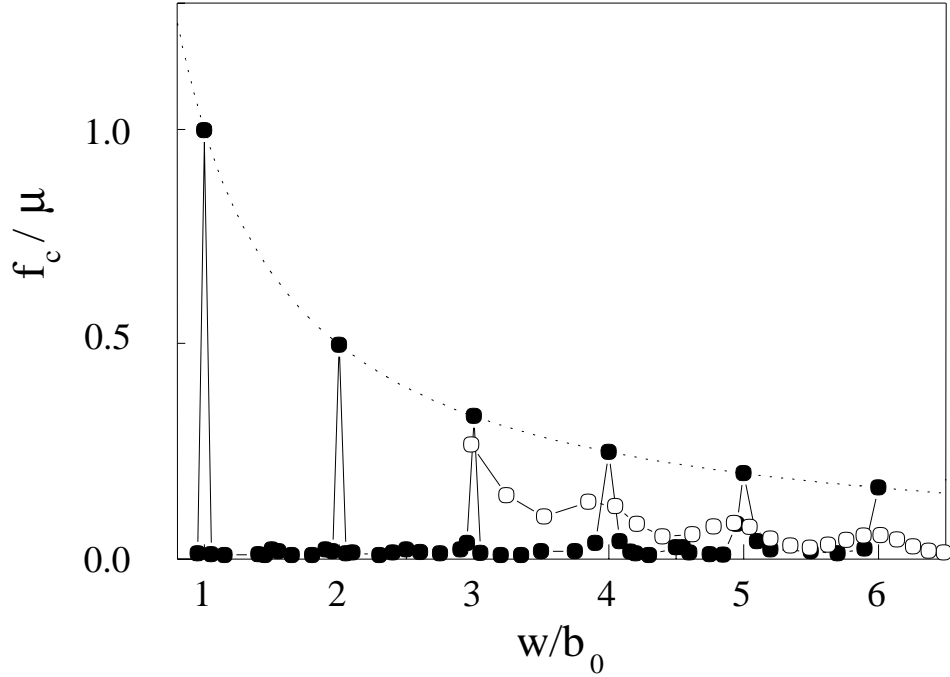


Figure 3.8: Depinning force f_c as a function of the ratio of channel width and vortex lattice plane distance, w/b_0 taken from Ref. [49]. The dashed line shows the maximum shear force $f_s = \mu b_0/w$ calculated within a continuum approximation for the vortex lattice. The dots display the oscillations of f_c due to transitions from a topologically ordered to a defective state determined from molecular dynamics simulations of channels with perfect vortex lattices in the channel edges. The open circles are the shear force data from Ref. [81] shown in Fig. 3.3.

3.2.5 Preliminary comparison with experimental data

Let us now compare these theoretical findings with experimental and numerical data [49]. Clearly, the generalized Frenkel-Kontorova model predicts a nearly vanishing depinning force $f_c \approx 0$ in the defective state. In the commensurate state, the depinning threshold f_c is finite, but decreases monotonously with increasing frustration and vanishes at the CIT, where the critical mismatch is reached, $\chi = \chi_c(0)$. In the artificial vortex channel experiments discussed in Section 3.1 one has $\lambda \sim 3a_0$. From Eq. (3.13) we find $g \sim 28$ and hence Eq. (3.26) yields $\chi_c(0) \sim 0.06$. Since $\chi = (b_0/w) - 1$, one expects a sharp spike in the threshold force around the magnetic induction with a vortex lattice plane distance $b_0 = w$.

In Fig. 3.8 data obtained in numerical simulations and in measurements by the Leiden group are shown [49]. Here, the critical force f_c is plotted as a function of w/b_0 . The dashed curve is the maximum shear force $f_s = \mu b_0/w$ calculated within a continuum approximation. The black dots are depinning force data computed in a molecular dynamics simulation of vortices in channels with a perfect vortex lattice in the channel edges. These

data show spikes of magnitude $f_c = \mu b_0/w$ at integer values of w/b_0 . The peak at $w/b_0 = 1$ corresponds to the scenario described within the Frenkel-Kontorova model in the previous section. The depinning force at non-integer values of w/b_0 is orders of magnitudes smaller than for integer values. Similar to the case described above for $w/b_0 \sim 1$, topological defects are present in channels of wider non-integer width. There, topological defects occur in the form of edge dislocations. The dislocations are only weakly pinned due to the lattice discreteness causing a nearly vanishing depinning force.

The experimental data that were previously shown in Fig. 3.3 are represented by open circles in Fig. 3.8 for comparison. The maximum shear force $f_s = F_s a_0 b_0$ is normalized to μ . In Fig. 3.8 which is taken from Ref. [49], μ has been related to the shear modulus, $\mu = 2a_0 c_{66}/(\sqrt{3}\pi)$. The shear modulus of the vortex lattice has been evaluated in the entire field range by Brandt [86],

$$c_{66} = \frac{B_{c2}\kappa^2}{32\pi\kappa_1^2\kappa_2^2} B \left(1 - 0.29 \frac{B}{B_{c2}}\right) \left(1 - \frac{B}{B_{c2}}\right)^2, \quad (3.39)$$

where κ , κ_1 , and κ_2 are the Ginzburg-Landau and the Maki parameters, the latter for the dirty limit.

This representation suggests that the position of the maxima in the experimentally determined f_c can be explained in terms of transitions from topologically ordered to defective phases. However, they are lower and of larger width than the “spikes” expected from the FKM. The simultaneous decrease of the depinning threshold in the topologically ordered case and the drastic enhancement of the critical force in the defective case can not be explained solely in terms of thermal or quantum fluctuations: They would lead to an effective reduction of the pinning barrier in both cases. This motivates us to study the influence of quenched disorder, which is present in the experimental situation. It is generally understood, that quenched disorder leads to pinning of vortices [36] or topological defects of the vortex lattice, which would explain the increased critical force in the defective state. It remains to understand how disorder leads to a reduction of pinning barriers in the commensurate regime.

3.2.6 Channel with a distorted vortex lattice in the environment

In a realistic sample the static nature of the channel environment is caused by some sort of pinning which may distort the vortex lattice. In the following we consider a device, where the vortices outside the channel are pinned by quenched disorder. The pinning in the channel environment is strong enough to guarantee that it remains pinned at all considered current densities whereas inside the channel pinning by quenched disorder is orders of magnitudes lower and can be entirely neglected. In a typical experiment the magnetic inductions are so large that the interaction between the vortices is much stronger than the pinning. Further, we assume that the vortex lattice in the channel environment is free of dislocations. Then it is natural to treat the vortex lattice in its elastic limit. In a weakly pinned vortex lattice, distortions of the order of the coherence length ξ due to

the disorder occur on average on a length l_c in the direction of the magnetic field and on a length R_c transverse to it. Here, we consider two-dimensional collective pinning where $l_c \gg l$ such that the approximation of straight vortex lines remains valid.

With quenched disorder in the environment of the channel, the interaction energy of a single vortex with the vortex row becomes

$$E_n(\mathbf{r}) = \sum_m U(\mathbf{r} - \mathbf{R}_{m,n} - \mathbf{d}_{m,n}), \quad (3.40)$$

where $\mathbf{d}_{m,n}$ are the displacements from the ordered positions $\mathbf{R}_{m,n}$. It is convenient to rewrite the row potential in terms of the vortex density

$$E_n(\mathbf{r}) = \int d^2 r' U(\mathbf{r} - \mathbf{r}') \rho_n(\mathbf{r}'), \quad (3.41)$$

where

$$\rho_n(\mathbf{r}') = \sum_m \delta(\mathbf{r}' - \mathbf{R}_{m,n} - \mathbf{d}_{m,n}). \quad (3.42)$$

We introduce a continuous displacement field

$$\mathbf{d}(\mathbf{r}) = \frac{a_0^2}{4\pi^2} \int_{BZ} d^2 k e^{i\mathbf{k}\mathbf{r}} \sum_{m,n} e^{-i\mathbf{k}\mathbf{R}_{m,n}} \mathbf{d}_{m,n}, \quad (3.43)$$

where BZ indicates that the integration is restricted to the first Brillouin zone. Note that $\mathbf{d}(\mathbf{R}_{m,n}) = \mathbf{d}_{m,n}$. Further, we define a relabeling field [87],

$$\Phi(\mathbf{r}) = \mathbf{r} - \mathbf{d}[\Phi(\mathbf{r})] \quad (3.44)$$

with

$$\Phi[\mathbf{R}_{m,n} + \mathbf{d}(\mathbf{R}_{m,n})] = \mathbf{R}_{m,n}.$$

In terms of these continuous fields, the vortex density reads

$$\rho_n(\mathbf{r}') = \det[\partial_i \Phi_j] \sum_m \delta[\Phi(\mathbf{r}') - \mathbf{R}_{m,n}] \quad (3.45)$$

and the vortex row potential becomes

$$E_n(\mathbf{r}) = a_0^{-1} \int d^2 r' U(\mathbf{r} - \mathbf{r}') \det[\partial_i \Phi_j] \sum_\nu \cos[q_\nu(\Phi_x(\mathbf{r}') - na_0/2)] \int \frac{dk_y}{2\pi} e^{ik_y[\Phi_y(\mathbf{r}') - nb_0]}.$$

At first sight, it seems that we have not gained much by performing the above transformations. However, as one expects, it has similarities with Eq. (3.2) and converges to the latter in the limit $\mathbf{d} \rightarrow 0$. In order to derive a simplified one-dimensional model as in the ordered case, we make use of a few approximations. Since we consider the vortex lattice to be in the elastic limit,

$$|\nabla \cdot \mathbf{d}| \sim \xi/R_c \ll 1, \quad (3.46)$$

we can approximate $\det[\partial_i \Phi_j] \approx 1 - \nabla \cdot \mathbf{d}$. Next, since the vortex potential falls off exponentially fast for $|\mathbf{r} - \mathbf{r}'| > \lambda$, the channel environment is mainly probed within $|\mathbf{r} - \mathbf{r}'| < \lambda$, where one can estimate $|\mathbf{d}(\mathbf{r}') - \mathbf{d}(\mathbf{r})| \lesssim \lambda \xi / R_c$ using Eq. (3.46). For $\lambda \xi / R_c \ll a_0/2$ it is then reasonable to expand the displacements $\mathbf{d}(\mathbf{r}')$ in the integral,

$$\mathbf{d}(\mathbf{r}') = \bar{\mathbf{d}}(\mathbf{r}) + \mathcal{O}\left(\frac{\lambda \xi}{R_c}\right). \quad (3.47)$$

Here, we have introduced the coarse grained displacement field

$$\bar{\mathbf{d}}(\mathbf{r}) = (2\pi U_0)^{-1} \lambda^{-2} \int d^2 r' U(\mathbf{r} - \mathbf{r}') \mathbf{d}(\mathbf{r}'), \quad (3.48)$$

which is smooth on the scale λ . Up to terms of the order $\mathcal{O}(\lambda \xi / R_c)$, we obtain

$$E_n(\mathbf{r}) = E_n^o[\mathbf{r} - \bar{\mathbf{d}}(\mathbf{r})] \quad (3.49)$$

for the collectively pinned vortex row potential.

To calculate the effective channel potential for a channel of width $w \sim b_0$, we perform the summation over pinned vortex rows E_n as in the ordered case. Further, since the influence of point-like disorder at the edge is much weaker than the re-ordering due to the edge currents, we may well take $\bar{d}_y(\mathbf{r}) = 0$. Then, the interaction of a single vortex in the channel with the disordered environment reads

$$E_{dc}(\mathbf{r}) = \sum_{\nu} A_{\nu}(y) \cos \left\{ q_{\nu} [x - \bar{d}_x(\mathbf{r})] \right\}, \quad (3.50)$$

For the partial derivatives of the channel potential one finds

$$\begin{aligned} \partial_x E_{dc}(\mathbf{r}) &= - \sum_{\nu} q_{\nu} A_{\nu}(y) \sin \left\{ q_{\nu} [x - \bar{d}_x(\mathbf{r})] \right\} + \mathcal{O}\left(\frac{\lambda \xi}{R_c}\right), \\ \partial_y E_{dc}(\mathbf{r}) &= \sum_{\nu} A'_{\nu}(y) \cos \left\{ q_{\nu} [x - \bar{d}_x(\mathbf{r})] \right\} + \mathcal{O}\left(\frac{\lambda \xi}{R_c}\right) \end{aligned} \quad (3.51)$$

As in the perfectly ordered case, we now consider the equation of motion. Substituting E_{oc} by E_{dc} in Eq. (3.10) and following similar arguments we derive an equation for the longitudinal motion. Introducing $\tilde{\varphi}(x) = q \bar{d}_x(x, 0)$ we obtain a generalized phase-disordered Frenkel-Kontorova model,

$$V = \sum_m \left\{ \frac{\mu}{q} \{1 - \cos [q x_m - \tilde{\varphi}(x_m)]\} - f x_m + \sum_n \frac{\kappa_n}{2} (x_{m+n} - x_m - n a)^2 \right\}. \quad (3.52)$$

The corresponding energy functional in the continuum limit is then

$$V[u] = a_0^{-1} \int_0^L dx \left\{ \frac{\tilde{\kappa}}{2} \left(\frac{\partial u}{\partial x} - \chi \right)^2 + \frac{\mu}{q} \{1 - \cos [q u - \tilde{\varphi}(x + u)]\} - f u \right\} \quad (3.53)$$

and the resulting equation of motion for the displacement fields $u(x, t)$ reads

$$\eta \dot{u} = f - \mu \sin [q u - \tilde{\varphi}(x + u)] + \tilde{\kappa} \frac{\partial^2 u}{\partial x^2} + \tilde{\kappa} \chi [\delta(x - L) - \delta(x)], \quad (3.54)$$

where $\partial_x \bar{d}_x$ -terms that are of order $\mathcal{O}(\lambda \xi / R_c)$ have been neglected.

3.2.7 Depinning in a channel with distorted environment

Up to now, we have not specified the disorder displacement field \bar{d}_x . To gain some basic understanding, we now consider the effect of a local distortion on the depinning properties. The field we choose is somewhat academic, but is convenient to understand the effect of a lattice distortion at the system boundary and in the bulk. The perturbation occurs around x_φ ,

$$\bar{d}_x(x, 0) = W(x - x_\varphi) \left[\theta(x - x_\varphi) - \frac{1}{2} \right]. \quad (3.55)$$

Here, $\theta(x)$ is the Heaviside function and $W > 0$ the distortion parameter. It is convenient to introduce transformed displacement fields $\tilde{u} = u - q^{-1}\tilde{\varphi}$. Neglecting terms of the order $(\partial_x \tilde{u})^2 \tilde{\varphi}'$ and $(\tilde{\varphi}')^2 \partial_x \tilde{u}$, the relevant \tilde{u} -dependent part of the energy functional reads

$$\tilde{V}[\tilde{u}] = V_{SG}[\tilde{u}] + V_\chi[\tilde{u}] + V_\varphi[\tilde{u}], \quad (3.56)$$

where

$$V_\varphi[\tilde{u}] = \frac{\tilde{\kappa}}{a_0} \int dx \frac{\partial \tilde{u}}{\partial x} \frac{\partial \bar{d}_x}{\partial x}. \quad (3.57)$$

In the following, we examine the effect of lattice distortions at the boundaries, $x_\varphi = 0, L$, and in the bulk, $x_\varphi = L/2$. To gain a basic understanding of the depinning process, we restrict the analysis to the large system limit, $L/2 \gg l_s$, where the system is so large that the depinning configurations at the weak spots $x_\varphi = 0, L$, and $x_\varphi = L/2$ do not interact with each other.

For $x_\varphi = 0$, the lattice is distorted homogeneously in the entire sample and the contribution of the distortion to the energy functional yields

$$V_\varphi[\tilde{u}] = \frac{\tilde{\kappa}W}{2a_0} [\tilde{u}(L) - \tilde{u}(0)]. \quad (3.58)$$

Physically, the distortion results in an additional frustration of the system, as can be immediately understood by comparing Eq. (3.58) with Eq. (3.18). This means that for the threshold force, one can use the results that were found in the absence of the distortion [see Eq. (3.36)], but the frustration has to be replaced by an effective frustration

$$\chi \rightarrow \chi - \frac{W}{2}. \quad (3.59)$$

The result is thus a simple shift of the $\chi - f_c$ -curve. Similarly, for $x_\varphi = L$, the $f - \chi$ -curve is shifted,

$$\chi \rightarrow \chi + \frac{W}{2}. \quad (3.60)$$

For $x_\varphi = L/2$, in addition to boundary depinning, bulk depinning at x_φ can occur. In large systems, $L/2 \gg l_s$ we can treat the effect of the distortions at the boundaries and in the bulk separately. At the boundaries, the threshold solution is then approximately given by the solution in absence of the defect, but with an increased effective frustration

$\chi + W/2$ in the left half and a lowered effective frustration $\chi - W/2$ in the right half of the system. The threshold force for boundary depinning is again given by Eq. (3.36) with the modulus of the frustration replaced by

$$|\chi| \rightarrow \left| |\chi| - \frac{W}{2} \right|. \quad (3.61)$$

To understand bulk depinning, we first restrict the considerations to $\chi = 0$ and then discuss the behavior in the presence of frustration.

For $L/2 \gg l_s$ we can neglect the influence of the boundaries and treat them as if they were shifted to $\pm\infty$. Then, the extremal threshold solution $\tilde{u}_\varphi(x; x_\varphi)$ can be constructed by joining two extremal solutions of V_{SG} . The matching condition is found from

$$\frac{\partial u(x - \varepsilon)}{\partial x} = \frac{\partial u(x + \varepsilon)}{\partial x} \quad (3.62)$$

such that the matching condition for the transformed field $\tilde{u}_\varphi(x; x_\varphi)$ reads

$$\frac{\partial \tilde{u}_\varphi(x_\varphi - \varepsilon; x_\varphi)}{\partial x} - \frac{\partial \tilde{u}_\varphi(x_\varphi + \varepsilon; x_\varphi)}{\partial x} = W \quad (3.63)$$

The mirror symmetry requires $\partial_x u(x_\varphi) = 0$, hence $\partial_x \tilde{u}(x_\varphi \pm \varepsilon) = \mp W/2$. At the threshold force f_c stable solutions cease to exist. In fact, it can be shown that at f_c the stable solution merges with an unstable one. This occurs, when the maximum of the tongue developing at x_φ reaches the maximum of the sinusoidal potential. From $\delta V/\delta u = 0$ follows that at the potential maximum the extremal solution has to fulfill $\partial_x^2 u(x_\varphi) = 0$, which holds if $\partial_x^2 \tilde{u}(x_\varphi \pm \varepsilon) \rightarrow 0$ for $\varepsilon \rightarrow 0$.

For weak distortions, $|W/2| \ll 1/(\pi\sqrt{g})$, the threshold force for bulk depinning is close to μ and the threshold solution $\tilde{u}_\varphi = \tilde{u}_s + \Delta\tilde{u}_\varphi$ can be found by merging two SAN solutions at $x_\varphi \pm x_a$, where $x_a = l_s \ln(2 + \sqrt{3})$,

$$\Delta\tilde{u}_\varphi(x; x_\varphi) = \begin{cases} \Delta u(x; x_\varphi + x_a) & x < x_\varphi \\ \Delta u(x; x_\varphi - x_a) & x \geq x_\varphi. \end{cases} \quad (3.64)$$

The maximum value of the tongue developing at x_φ is given by $\Delta\tilde{u}_\varphi(x_\varphi; x_\varphi) = 2a_s/3$. This implies

$$\frac{\partial \Delta\tilde{u}_\varphi(x_\varphi - \varepsilon; x_\varphi)}{\partial x} = \frac{2a_s}{3\sqrt{3}l_s} = \frac{W}{2}, \quad (3.65)$$

from which one obtains the bulk depinning threshold force in the presence of weak distortions,

$$\hat{f}_c = \mu \left[1 - \frac{1}{2} \left(\frac{\pi\sqrt{3g}}{2} W \right)^{4/3} \right]. \quad (3.66)$$

This formula becomes invalid for $2/(\pi\sqrt{g}) - |W| \ll 2/(\pi\sqrt{g})$. For strong distortions, $|W| \gtrsim 2/(\pi\sqrt{g})$, the threshold configuration can be constructed by merging a kink and an anti-kink

$$\tilde{u}_\varphi(x; x_\varphi) = \begin{cases} u_k(x; x_\varphi) & x < x_\varphi \\ u_a(x; x_\varphi) & x \geq x_\varphi \end{cases} \quad (3.67)$$

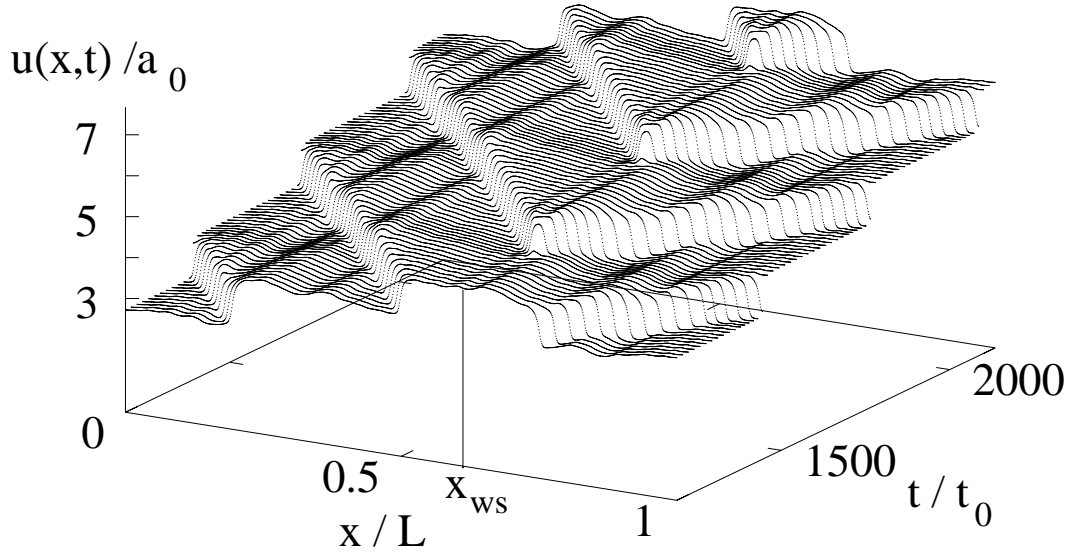


Figure 3.9: Time evolution of the displacements $u(x, t)$ in a system of length $L = 1000a_0$ for $\chi = 0$ and $W = 0.1$. Around the weak spot near $x_{ws} \sim 0.6L$, particles are unstable. First, a small tongue is formed, which represents a local variation in the particle density. Then, a vacancy-interstitial pair is fully developed. Vacancies (kinks) travel to the left, interstitials (anti-kinks) to the right. Periodically, new tongues are generated initiating new pair-production processes.

from which one obtains the bulk depinning threshold force in the presence of strong distortions,

$$\hat{f}_c = \frac{4\mu}{\pi} \left(1 - \frac{\pi\sqrt{g}}{2} W \right). \quad (3.68)$$

At $W = 2/(\pi\sqrt{g})$ stable saddle-point solutions cease to exist for all f and disorder induced mobile kink-anti-kink pairs are spontaneously formed even at equilibrium.

After having gained some understanding how pinning occurs at a weak spot in the bulk for $\chi = 0$, let us now consider the frustrated case, $|\chi| > 0$, where bulk depinning competes with boundary depinning. Comparing the bulk depinning threshold $\hat{f}_c(W)$ with the boundary threshold in presence of the defect, $f_c(|\chi| - W/2)$, we find that for $|\chi| < W$ the system depins in the bulk and for $|\chi| > W$ at one of the boundaries. Note that to lowest order, we can apply these results to distortions of this kind that are not necessarily centered at $x_\varphi = L/2$, as long as $l_s \ll x_\varphi \ll L - l_s$ holds.

3.2.8 Depinning in a channel with randomly displaced edge vortices

Opposed to the rather well behaved distortions of the previous paragraph, we now consider the effect of randomly displaced vortices in the channel edge. We mimic the disorder by

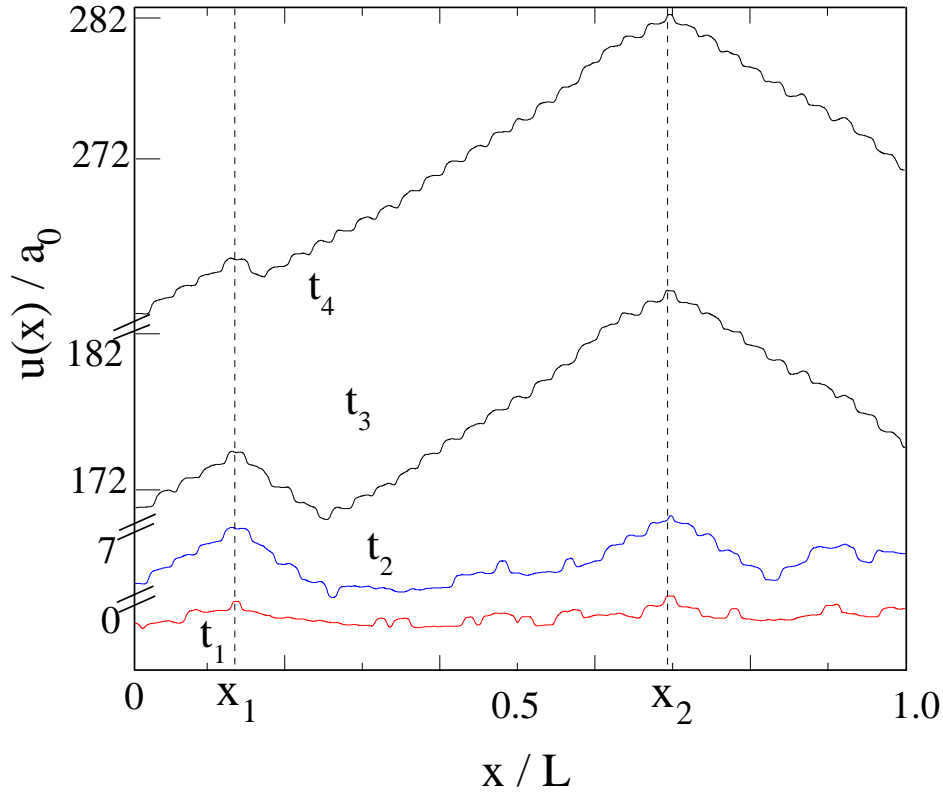


Figure 3.10: Transient response in a system of size $L = 3000a_0$ with $\chi = 0$ and $W = 0.1$. After the threshold \tilde{f}_c is exceeded, particles depin at several weak spots (e.g. x_1 and x_2) at $t = t_1$. The triangular shaped regions in the displacements $u(x, t)$ at $t = t_3$ correspond to domains of vacancies (positive slope) and interstitials (negative slope). After a time $t = t_4$ only the fronts which are generated at the weakest spot x_2 with the highest production rate of vacancy-interstitial pairs survives.

uncorrelated relative displacements $[\bar{d}_x(\mathbf{R}_{m+1,n}) - \bar{d}_x(\mathbf{R}_{m,n})]/a_0$. The latter are independent identically box-distributed random numbers within the interval $[-W/2, W/2]$,

$$P_W(\bar{d}_x) = \frac{1}{W} \left[\theta(\bar{d}_x + W/2) - \theta(\bar{d}_x - W/2) \right]. \quad (3.69)$$

The width of the box distribution W parameterizes the disorder strength. Then, $\tilde{\mu}$ and $\partial_x \tilde{\varphi}$ are random functions, which are smooth on the scale λ and bounded. Note that although $\partial_x \tilde{\varphi}$ is bounded, $\tilde{\varphi}$ is unbounded. Thus, long range order is lost along the channel direction. On length scales much larger than a_0 , the displacement field $\bar{d}_x(\mathbf{r})$ behaves like a random walk in 1d and the phase-phase correlator scales linearly with the distance, $\langle [\tilde{\varphi}(x) - \tilde{\varphi}(0)]^2 \rangle \propto x$.

First we consider the unfrustrated case, $\chi = 0$, where each vortex populates a minimum of the nearly periodic potential. In the following \tilde{f}_c denotes the threshold force of a single channel in the presence of a disordered channel environment. The evolution $u(x, t)$ upon

a stepwise force increase from $f(t = 0) < \tilde{f}_c$ to $\tilde{f}_c < f(t > 0) < \mu$ is plotted in Fig. 3.9 for $L = 1000a_0$. For $f < \tilde{f}_c$, the displacements $u(x, t) \ll a_0$ are small such that vortices are slightly adjusting to the disorder but remain locked to their potential well: the channel is topologically ordered. For $f > \tilde{f}_c$ the motion starts at a point of minimal stability where $u(x, t)$ increases locally with time. At this spot kinks of $\pm a_0$ in $u(x, t)$ are generated corresponding to the nucleation of vacancy-interstitial pairs in the channel. Thus the critical force \tilde{f}_c is identical to the nucleation threshold of a defect pair. The defects move under the applied force and a new nucleation at the "weak spot" occurs after a time t_{nuc} when the vortices in the neighborhood have moved approximately by a_0 . The nucleation process repeats periodically with a rate $\Gamma_{\text{nuc}} = t_{\text{nuc}}^{-1}$. The vortex row splits up in two parts: left of the instability vacancies travel to the left and right of the instability interstitials move to the right. Since the motion of the row is governed by the nucleation at the weak spot, its velocity is $v = a_0 \Gamma_{\text{nuc}}$.

If we again consider a stepwise force increase in a larger system of $L = 3000a_0$ we observe the following (see Fig. 3.10): initially nucleation sites x_m with a nucleation threshold force $f_{\text{nuc}}^{(m)}$ and rate $\Gamma_{\text{nuc}}^{(m)}$ are active. However, when two domains that were generated at weak spots, let us say x_1 and x_2 with rates $\Gamma_{\text{nuc}}^{(1)} > \Gamma_{\text{nuc}}^{(2)}$ "meet", their defects of opposite sign annihilate. Due to the higher defect density of domain 2, this region expands at the cost of domain 1 with the front in between them having a velocity $a_0(\Gamma_{\text{nuc}}^{(2)} - \Gamma_{\text{nuc}}^{(1)})$. This transient behavior shows that eventually the stationary state for all $f < \mu$ is governed by the nucleation site with the smallest threshold $\min\{f_{\text{nuc}}^{(m)}\}$ forming a domain with maximum defect density that spans the entire system. What also becomes clear is that depinning in the topologically ordered channel with weakly perturbed channel edges takes place from a static solution that is unique up to a global phase of 2π . The depinning considered here occurs at a saddle-node bifurcation of the energy functional: Below \tilde{f}_c all principal curvatures of the energy functional are positive, indicating a stable solution. At $f = \tilde{f}_c$ one of the principal curvatures becomes zero and negative for $f > \tilde{f}_c$. The dynamics close to the threshold is governed by the small curvature at the saddle node leading to a non-linear force-velocity characteristics, $v \sim (f - \tilde{f}_c)^{1/2}$, similar to the single particle result, but with a reduced threshold force.

In a typical vortex-flow channel experiment one studies samples with a few hundred channels. Hence, when measuring the current-voltage characteristics, one obtains an average signal generated by all active channels. The experimentally determined critical current is usually defined by a finite-voltage criterion, i.e. the depinning transition occurs, when the smallest measurable voltage is detected. In the literature the corresponding critical force F_c is given by the value, where the disorder ensemble-averaged velocity vanishes, $\langle v \rangle(f = F_c) = 0$.

Let us now study how the critical force F_c of the channel ensemble is related to the threshold forces \tilde{f}_c of the individual channels. For $\chi = 0$ we observed that in a channel of length L the threshold force \tilde{f}_c is given by the minimum force at which the first nucleation of a defect pair takes place. If two systems of length L with thresholds $\tilde{f}_{c1} < \tilde{f}_{c2}$ are joined, one obtains a merged system of length $2L$ with a threshold force $\tilde{f}_{c12} \approx \tilde{f}_{c1}$. Channels of length NL can be constructed by merging N channels which are randomly chosen from the

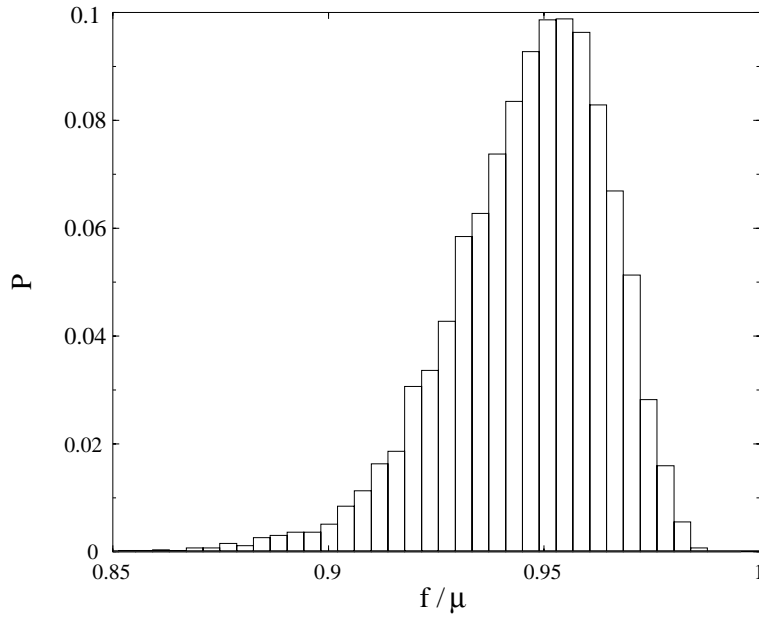


Figure 3.11: Numerically obtained distribution of threshold forces \tilde{f}_c for 10000 channels with $L = 100a_0$, $\lambda = a_0$, $W = 0.1$, and $\chi = 0$.

ensemble of disordered channels with length L . The longer the channel gets, the smaller is the threshold force.

With respect to the probability distribution $P_L(\tilde{f}_c/\mu)$ of threshold forces \tilde{f}_c in systems of length L we conclude that the low force tails determine the depinning behavior of the ensemble. We are thus interested in the statistical properties of the extremal values – namely the minima – rather than the most probable values of \tilde{f}_c . The shape of $P_L(\tilde{f}_c/\mu)$ depends on L : with increasing L the maximum of $P_L(\tilde{f}_c/\mu)$, which is the most probable value of \tilde{f}_c/μ , approaches the minimum value $\min\{\tilde{f}_c/\mu\}$ of the ensemble. This can be seen by studying the probability that channels of the ensemble have depinned, which is given by the cumulative distribution

$$\mathcal{P}_{<}^L(f/\mu) = \mu^{-1} \int_0^f d\tilde{f}_c P_L(\tilde{f}_c/\mu), \quad (3.70)$$

or by the probability that they remain static, which is given by

$$\mathcal{P}_{>}^L(f/\mu) = \mu^{-1} \int_f^\infty d\tilde{f}_c P_L(\tilde{f}_c/\mu). \quad (3.71)$$

Neglecting correlations between the segments of length L , the depinning probability of a system with length NL is then

$$\mathcal{P}_{<}^{NL}(f/\mu) = 1 - [\mathcal{P}_{>}^L(f/\mu)]^N. \quad (3.72)$$

Hence, as long as $\mathcal{P}_{<}^L > 0$, in the limit $N \rightarrow \infty$ the depinning probability $\mathcal{P}_{<}^{NL} \rightarrow 1$.

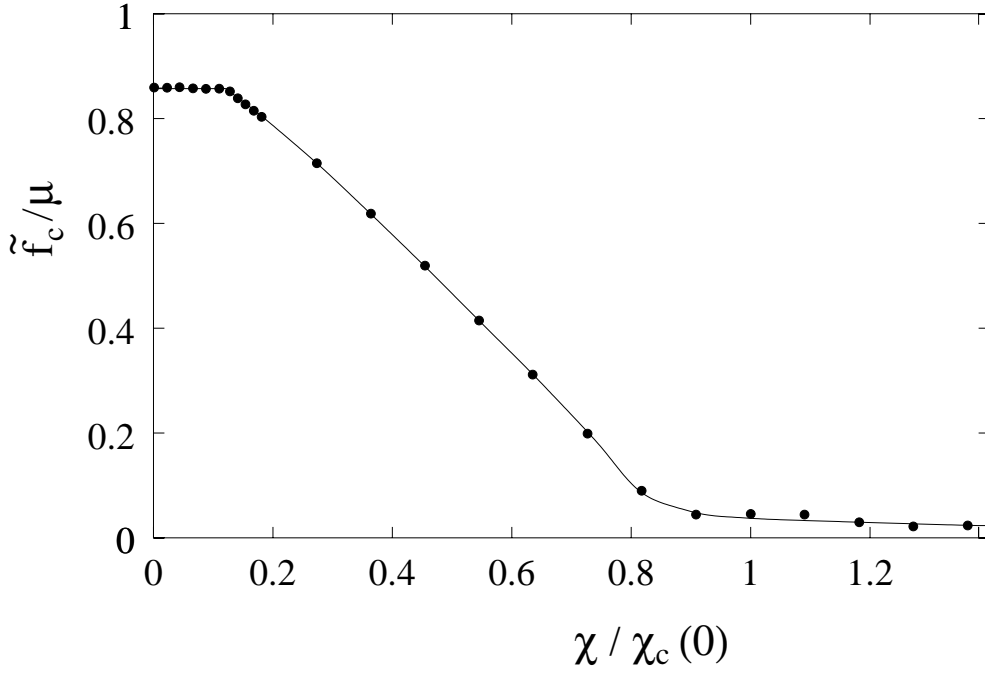


Figure 3.12: Numerically obtained minimum threshold force \tilde{f}_c as a function of frustration χ for 100 channels with $L = 100a_0$, $\lambda = a_0$, and $W = 0.1$.

In the model considered here $P_L(\tilde{f}_c/\mu)$ is bounded from above and for $W < 2/(\pi\sqrt{g})$ from below, $0 \leq \tilde{f}_{min} < \tilde{f}_c < \mu$. The upper bound can be understood from the fact that for weak disorder, where \tilde{f}_c is close to μ , weak lattice distortions still act as nucleation seeds which reduce the threshold slightly below μ . A finite lower bound $\tilde{f}_{min} > 0$ exists for $W < 2/(\pi\sqrt{g})$. For weak disorder, $W \ll 2/(\pi\sqrt{g})$, it is $\tilde{f}_{min} \approx \mu[1 - (1/2)(\pi\sqrt{3g}W/2)^{4/3}]$, and for $W \lesssim 2/(\pi\sqrt{g})$ it is $\tilde{f}_{min} \approx 4\mu(1/\pi - \sqrt{g}W/2)$. This lower bound arises from rare configurations similar to the ones that were discussed in Section 3.2.7. The existence of a lower bound is a peculiarity of bound disorder distributions as the box distribution that is used here. For $W > 2/(\pi\sqrt{g})$ or for unbound disorder distributions there is always a low, but finite probability that strong local distortions in the channel lead to nucleation of defects at equilibrium.

In Fig. 3.11 a numerically obtained probability distribution $P(\tilde{f}_c/\mu)$ of threshold forces \tilde{f}_c for 10000 channels of length $L = 100a_0$, penetration depth $\lambda = a_0$, disorder strength $W = 0.1$, and frustration $\chi = 0$ is shown. We find $\tilde{f}_{min} \approx 0.62$. The lowest value ~ 0.85 of \tilde{f}_c shown in the histogram suggests that in small systems there is an extremely low probability that values of the order of \tilde{f}_{min} are reached. However, according to our above discussion, the probability should increase exponentially with the system size, e.g. for $P_{<}^{100}(0.85) \sim 10^{-5}$ we have $P_{<}^{1000}(0.85) \sim 10^{-4}$, $P_{<}^{10000}(0.85) \sim 10^{-3}$ and so forth.

Let us now discuss the depinning scenarios in the presence of frustration, $|\chi| > 0$. In weakly frustrated systems, $|\chi| < W/2$, nucleation still occurs at a weak spot in the bulk.

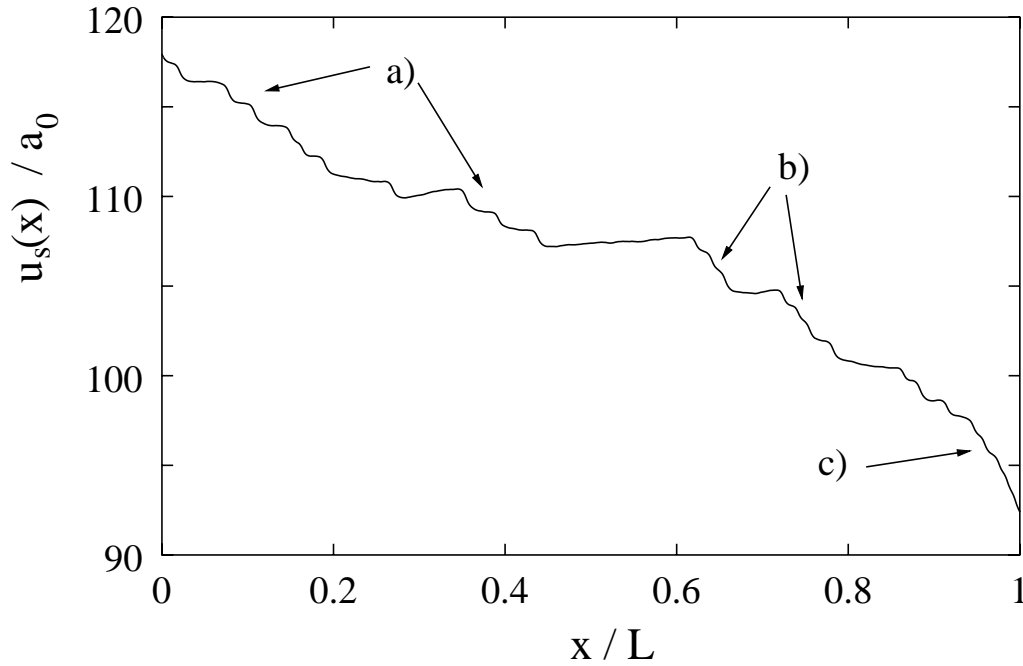


Figure 3.13: Static displacements $u_s(x)$ in a system of length $L = 1000a_0$ for $\chi = -\chi_c(0)$ in the pinned regime, $f < \tilde{f}_c$. a) Pinned single interstitials (kinks). b) Multiple pinned kinks at strong pinning sites. c) Kink accumulation at the end of the system, $x \lesssim L$, where in addition to disorder the exit barrier is present.

Hence, the depinning threshold \tilde{f}_c should be independent of the frustration χ . This can be indeed observed, see Fig. 3.12: the $\chi - \tilde{f}_c$ -curve has a plateau around $\chi \sim 0$, before at larger values of χ depinning takes place via the formation of defects at the boundary as in the ordered case. The threshold for boundary depinning is affected by lattice distortions at the sample edge as discussed in Section 3.2.7 resulting in an overall shift of the $\chi - \tilde{f}_c$ -curve to lower values of χ .

For intermediate frustration, $0 \ll \chi \ll \chi_c(0)$, a defect that entered the sample via the boundary cannot be pinned by disorder in the bulk. It moves freely to the other boundary, where it becomes pinned by the exit barrier until being released by the next defect that enters the channel and then travels freely to the exit.

For frustrations above $\chi_c(0) - W/2$ bulk pinning becomes possible since the boundary depinning threshold force becomes lower than the disorder induced pinning forces in the bulk. In Fig. 3.12 bulk pinning becomes relevant around $\chi \sim 0.8\chi_c(0)$. Indeed one can observe pinning of defects and bundles of defects in the numerical simulations in this regime. In Fig. 3.13 a static state in a system of length $L = 1000a_0$ for $\chi = -\chi_c(0)$ just below the depinning threshold $f \lesssim \tilde{f}_c$ is shown. One clearly sees single pinned kinks and a few multiple-pinned kinks (bundles). At the exit of the system kinks accumulate due to both bulk pinning and due to pinning at the presence of the exit barrier. When reaching the depinning threshold, a defect is formed at the entry on the channel and travels until

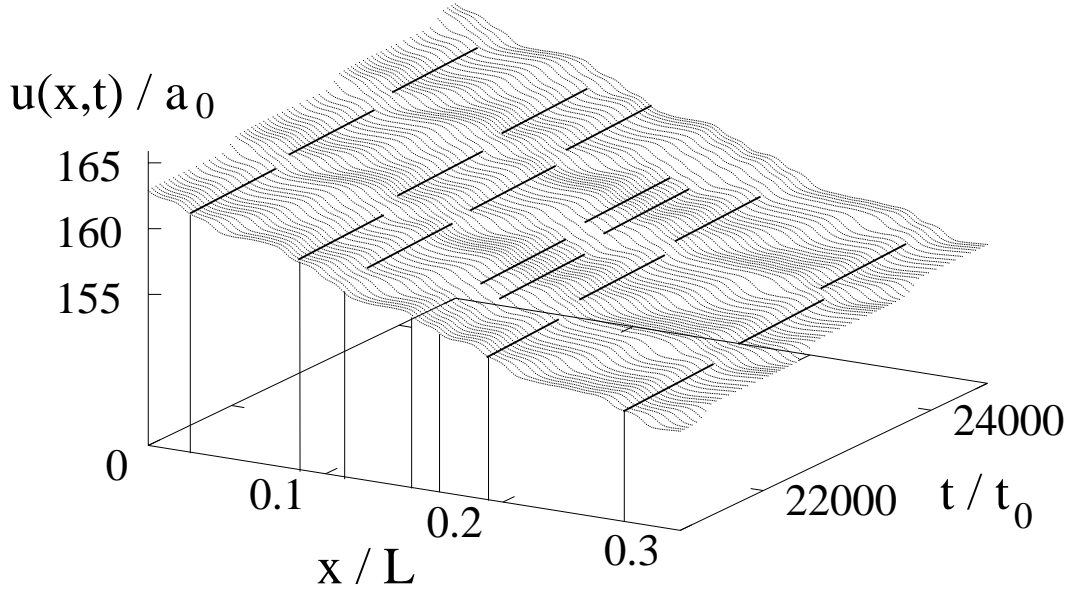


Figure 3.14: Time evolution of the displacements $u(x, t)$ in a system of length $L = 1000a_0$ for $\chi = -\chi_c(0)$ and $f > \tilde{f}_c$. Strong pinning sites are indicated by bars parallel to the time axis. Here, interstitials (anti-kinks) travel to the right. At strong pinning sites they collide with pinned kinks. The formerly pinned kinks are released while the previously moving ones become pinned.

it collides with a defect that is already pinned at a strong pinning site. While the latter becomes released, the former gets pinned. This scenario repeats until a mobile defect has reached the channel exit, see Fig. 3.14.

In contrast to the force-velocity curve of single systems, which behave as $v \sim (f - f_c)^\nu$ with $\nu = 1/2$, the functional form of the disorder averaged force-velocity curves for finite systems all show upward curvature for $f \gtrsim \tilde{f}_c$, which corresponds to $\nu > 1$, see Fig. 3.15. A crossover between exponents similar to the transition $\nu = 1/2 \rightarrow 1$ occurring in the ordered model at $\chi_c(0)$ can not be observed in the disordered case.

Until now we considered the weak disorder limit in agreement with the assumptions made in order to develop the disordered model. If we increase the disorder parameter W beyond the initially assumed limits, we can gain some insight into the depinning properties at large disorder. In Fig. 3.16 minimum threshold forces \tilde{f}_c as a function of disorder strength W for 100 channels with $L = 100a_0$, and $\lambda = a_0$ are shown for systems without frustration $\chi = 0$ and for frustrated systems with $\chi = \chi_c(0)$, where we expect the effect of the boundaries to become irrelevant. At $W = 0.5$ the disorder is so strong, that a distinction between a commensurate and an incommensurate system cannot be made. We speculate that this indicates a crossover to a depinning transition with true critical behavior as is reported for sandpile models or the Fukuyama-Lee-Rice model for charge density waves.

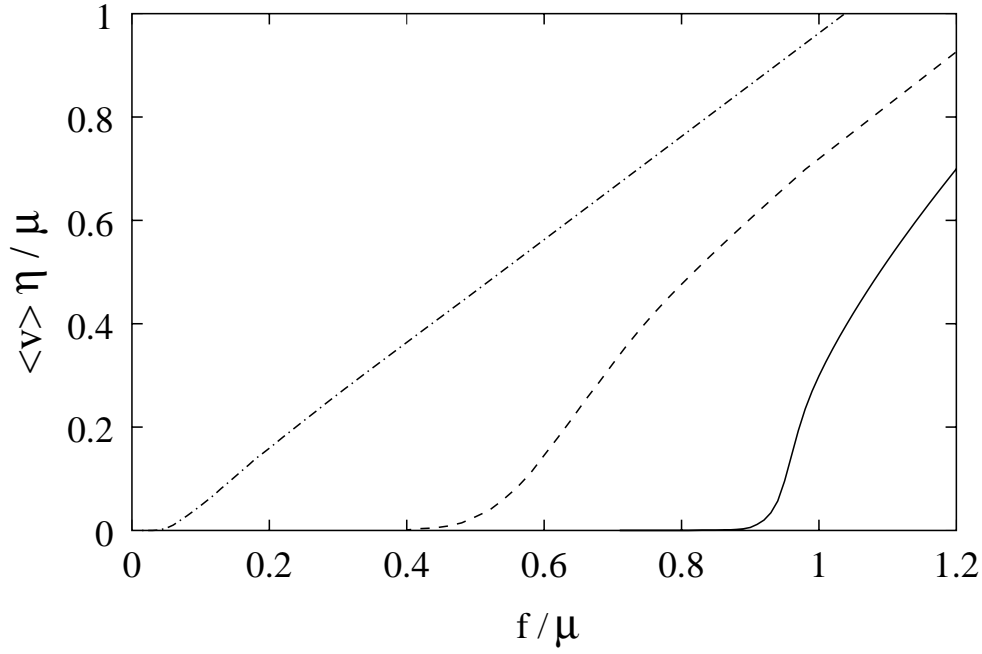


Figure 3.15: Disorder averaged $f - v$ curves computed for systems with $L = 100a_0$ and $\lambda = a_0$. Shown are the $f - v$ characteristics for systems with $\chi = \chi_c(0)$ (dash-dotted), $\chi = 0.5 \chi_c(0)$ (dashed), and $\chi = 0$ (solid).

3.3 Comparison with Experimental Data

Let us now compare our results with available experimental data [47–49, 88]. In artificial vortex-flow channels the current-voltage (I-V) characteristics have been measured following two different experimental procedures, the increasing-field (IF) measurement and the decreasing-field (DF) measurement. In the IF measurement, after the sample is zero-field cooled well below the lower critical temperature of the two superconducting materials, a finite magnetic field is applied and the I-V curve measured. Then the field is increased and the next I-V characteristics obtained. This procedure is repeated several times until the largest achievable magnetic fields are reached. The DF procedure starts with field-cooling the sample into the Meissner state. Then sets of I-V curves are measured as before, but for successively decreasing fields.

The I-V characteristics obtained by the two methods differ significantly. The DF data in Fig. 3.17 display a non-linear behavior $V \sim [I - I_c(H)]^\nu \propto (f - f_c)^\nu$ with $\nu > 1$, where $f_c \propto I_c(H)$ smoothly oscillates with the applied field H , as shown in Fig. 3.3. In the IF mode (see Fig. 3.18), below a characteristic current I_T an I-V curve consists of a fairly linear low-mobility regime, $V \sim [I - I_c(H)]^\nu$ with $\nu \sim 1$. Above I_T it becomes nonlinear with $V \sim [I - I_T(H)]^{\nu_T(H)}$. The exponent $\nu_T(H)$ changes its value at H_* from $\nu_T(H < H_*) < 1$ to $\nu_T(H > H_*) > 1$. In the IF measurement, oscillations of I_c with H are only observed for $H > H_*$.

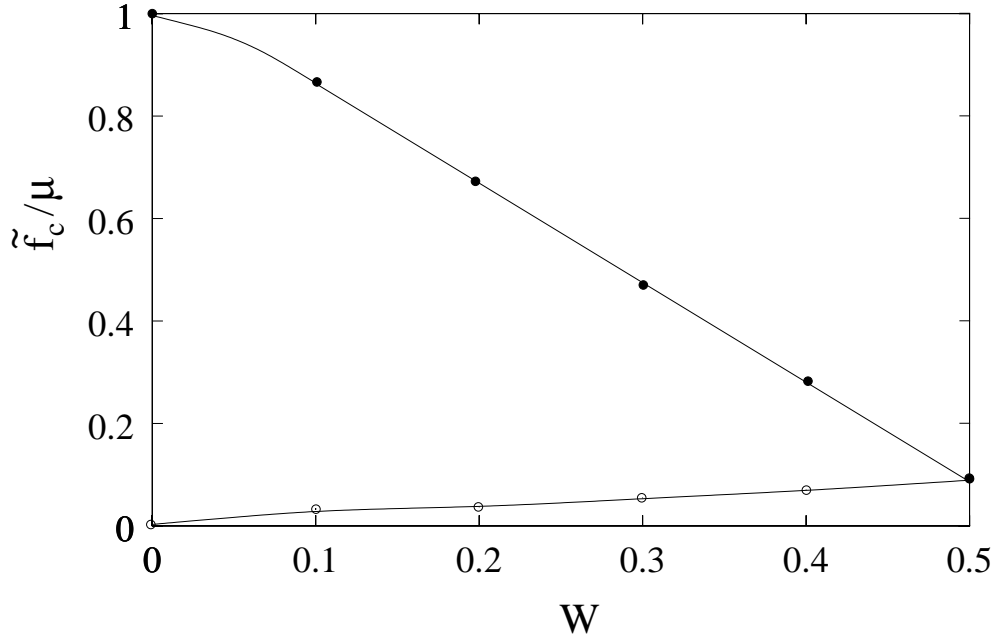


Figure 3.16: Numerically obtained minimum threshold force \tilde{f}_c as a function of disorder strength W for 100 channels with $L = 100a_0$, and $\lambda = a_0$. Upper curve: $\chi = 0$, lower curve $\chi = \chi_c(0)$.

It is interesting to note that even when one starts in the IF mode, as soon as H is decreased one immediately switches to the DF branch of $I_c(H)$, see Ref. [47]. Vice versa, when first performing a DF measurement, $I_c(H)$ jumps to the IF curve as soon as H is increased again. These features are attributed to currents that flow along the material steps of the channel edges in the IF measurement, but suddenly disappear when the magnetic field ramp is reversed.

Though the values of ν and ν_T have not been determined very accurately in the experiments, we attempt a rough comparison with our theoretical findings for weakly disordered ensembles, where we observe $\nu > 1$ very close to the depinning transition. In commensurate systems, $\nu_T = 1/2$ and in incommensurate systems $\nu_T = 1$.

The observed $\nu > 1$ measured in the DF procedure are comparable to what we see in the simulations of weakly disordered systems close to the depinning transition. However, in the experiments, this behavior occurs in a large current interval, whereas in the numerical simulations it is observed in a small current interval above the depinning transition. We suspect that due to the absence of channel edge currents in the FD measurements, the static vortex lattice in the environment is distorted both longitudinally and transversally to the channel. The transverse displacements lead to strong disorder which we have not treated. However, one may speculate that the current interval where $\nu > 1$ is much larger compared to the weakly disordered case.

Interestingly, the I-V characteristics of the IF measurements for $H < H_*$ have a regime

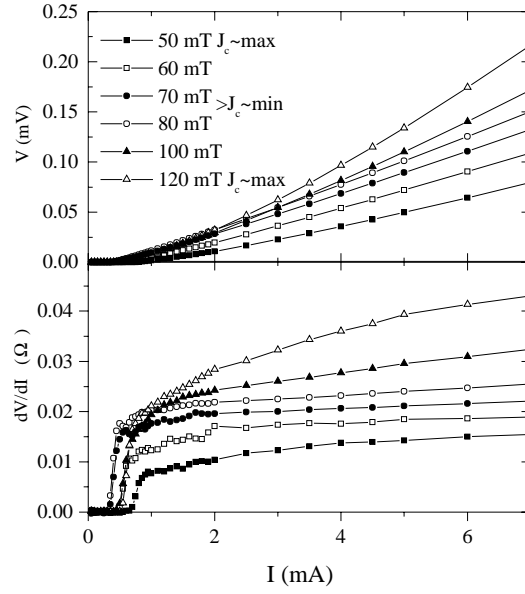


Figure 3.17: I-V curves and resistance data obtained by the Leiden group [88] from decreasing-field measurements.

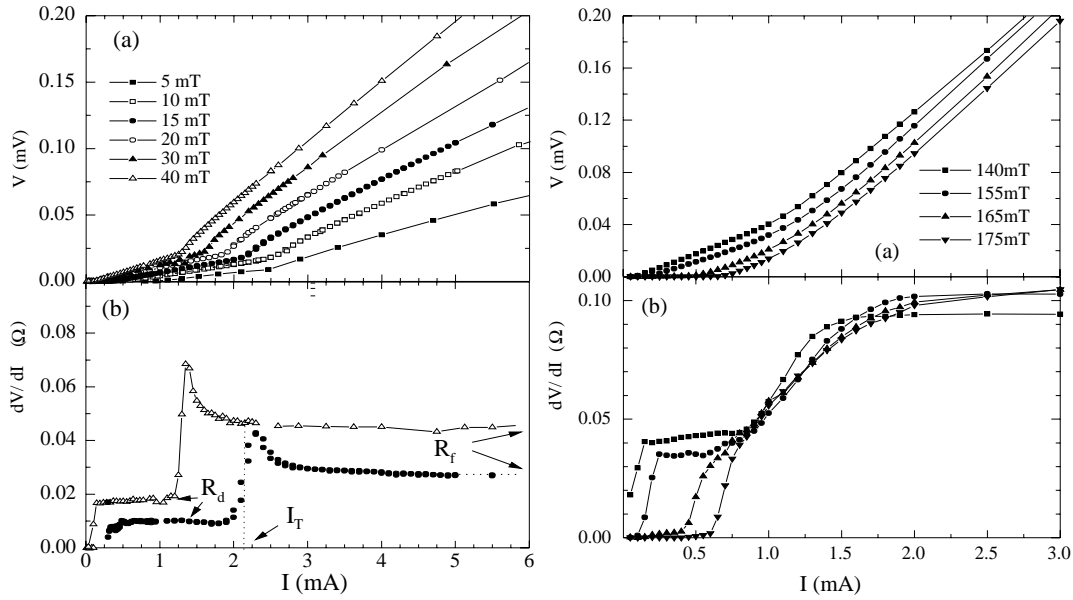


Figure 3.18: I-V curves (a) and resistance data (b) obtained from increasing-field measurements [88] . Left figure: $H < H_*$. Right figure: $H > H_*$.

for $I > I_T$ where $\nu_T < 1$ resembling the $f - v$ curves of our weakly disordered model in the commensurate state with $\nu = 1/2$. On the other hand, the linear behavior measured for $I < I_T$ is similar to what is observed in the incommensurate state of our model just above the small interval around the depinning transition. Comparing the resistance dV/dI below and above I_T , one finds that the flux flow resistance R_f for $I \gg I_T$ is by a factor three larger than the resistance in the defective low mobility regime R_d for $I < I_T$, $R_f \sim 3R_d$. This suggests that above I_T the number of vortex rows moving in the channel has increased by a factor three. Then the number of vortex rows moving in the channel would be larger than one above I_T .

In the IF measurements, the edge currents that flow along the channel edges for $H < H_*$ generate a Bean-Livingston barrier for vortices. Besides directing and ordering the static vortex lattice in the neighborhood of the channel edge they seem to squeeze the mobile vortices in the channel. This leads to a gradient of the vortex density transverse to the edge as has been lately observed in magnetic decoration experiments [88]. If several vortex rows are in the channel, we expect that the frustration of the lattice increases from the edges to the center of the channel. The inner rows are thus strongly frustrated with respect to the rest of the lattice.

A possible depinning scenario for three vortex rows in the channel for $H < H_*$ could be the following. At the low threshold current I_c first the inner row depins. Then at the larger current I_T the outer rows depin. The low threshold I_c for the inner row can be attributed to the strong frustration such that the entry barrier for defects is lowered or even has vanished. The depinning threshold current I_T of the outer rows is expected to be larger, since they are less frustrated. Their depinning leads to the crossover to I-V curves with downward curvature, $\nu < 1$.

At $H \sim H_*$ the Bean-Livingston barrier vanishes. For $H > H_*$ the transverse order of vortices along the channel edges vanishes and the effective disorder becomes strong. Consequently, the I-V curves become similar to the DF results.

3.4 Discussions and Conclusions

In this chapter we have developed a model for artificial vortex-flow channels motivated by recent experiments [47–49]. We have studied the depinning properties of vortices in channels of finite length taking into account inhomogeneities such as the sample boundaries and disorder.

Throughout our analysis, we have neglected the influence of thermal or quantum fluctuations on the depinning process. To see that this is well-justified with respect to the experiments that have been performed so far, let us estimate the magnitude of both types of fluctuations in conventional type-II superconductors which have been used to fabricate the channels. The typical pinning energies of topological lattice defects are larger than the vortex self energy, which is about 10 eV , whereas the thermal energy is $\sim 10^{-4} \text{ eV}$ since the samples are cooled down to $\lesssim 2 \text{ K}$. Hence, only when the resulting energy barriers are reduced by a factor $\sim 10^{-5}$ one can expect to observe thermal creep of vortex lattice

defects. Since the barrier energy scales as $\propto (1 - j/j_c)^{3/2}$, the width of the current density interval around j_c at which thermal creep can be observed is $\Delta j \lesssim 10^{-3} j_c$.

To estimate the relevance of quantum creep, we consider the effective Euclidean action as a function of the current density, $S_E^{eff}(j)$. At equilibrium, $j = 0$, $S_E^{eff}(j = 0) \approx \xi \hbar^2 / (e^2 \rho) (j_d/j_c)^{1/2}$, see Ref. [36]. Here the coherence length is $\xi \sim 10 \text{ nm}$, the resistivity in the normal state is $\rho \sim 10^{-6} \Omega m$, the depairing current is $j_d \sim 10^9 \text{ A/m}^2$, and the critical current is $j_c \sim 10^6 \text{ A/m}^2$. We find $S_E^{eff}(j = 0)/\hbar \sim 10^3$. For an overdamped vortex dynamics, which is characteristic for conventional superconductors, $S_E^{eff}(j)/\hbar \sim 10^3 (1 - j/j_c)^{3/4}$. Quantum effects become irrelevant for $S_E^{eff}(j) \sim \hbar$, hence $\Delta j \sim 10^{-4} j_c$. Thus, in artificial vortex-flow channels made of conventional superconductors thermal and quantum fluctuations only become relevant in an extremely narrow interval around the critical current which has not been resolved in the experiments discussed here. In a first step, we have therefore entirely neglected fluctuations and have studied a purely classical mechanical model at zero temperature.

First, we have considered a perfectly ordered vortex lattice in the channel environment, which effectively produces a periodic potential experienced by the vortices in the channel. We have studied the overdamped dynamics of a chain of interacting vortices in the effective channel potential. In our simplified description we have restricted the considerations to channels with a width of the order of the lattice spacing, $w \sim b_0$. We have assumed that the resulting confinement perpendicular to the channel direction is strong such that the transverse motion of the vortices in the channel can be neglected. Further, since in all known channel experiments even for the lowest achievable magnetic inductions $\lambda \gtrsim a_0$ holds, to a very good accuracy only the first harmonic of the periodic potential is kept. These assumptions and restrictions allow to determine the coefficients of a driven generalized Frenkel-Kontorova model (FKM). For $\lambda \gtrsim a_0$ where the typical length of a topological defect in the channel is much larger than the lattice spacing, $l_s \gg l_d \gg a_0$, the dynamics in the channel is conveniently described by the continuum limit of the FKM known as the driven Sine-Gordon model.

The depinning scenario depends on the frustration parameter $\chi = (a - a_0)/a_0$, which measures the mismatch between the lattice constant a_0 of the channel environment and the preferred lattice spacing in the channel a . In the absence of frustration, $\chi = 0$, depinning occurs via a trivial homogeneous solution when the barrier of the tilted washboard potential vanishes and the threshold force is given by the amplitude of the sinusoidal channel pinning force, $f_c = \mu$. In the presence of frustration, depinning occurs via the formation of topological defects at one of the sample boundaries. For weak frustration, $|\chi| \ll \chi_c(0)$, we find $f_c = \mu \{1 - (1/2)[\sqrt{3} \chi/\chi_c(0)]^{4/3}\}$, whereas close to the threshold frustration, $\chi_c(0) - |\chi| \ll \chi_c(0)$, we obtain $f_c = (4\mu/\pi)[1 - \chi/\chi_c(0)]$ and for $|\chi| > \chi_c(0)$ the depinning force vanishes, $f_c = 0$. By performing a numerical integration of the equation of motion we have determined the values of $f_c(\chi)$ in between these limits.

Further, we have numerically calculated the force-velocity curves which correspond to the current-voltage characteristics of the sample. In the commensurate regime, $|\chi| < \chi_c(0)$ we find a characteristics typical to a saddle-point bifurcation scenario, $v \sim (f - f_c)^{1/2}$, whereas in the incommensurate regime, where the commensurability gap has vanished,

the response is linear, $v \sim f$. This behavior is typical for a system with open boundary conditions, where the density of topological defects is a function of *both* the frustration χ and the driving force f .

In systems with twisted periodic boundary conditions, where the density of topological defects is constant, the force-velocity characteristics is different in the incommensurate regime [49]. One observes a linear low-mobility regime for small driving forces, $f \ll \mu$. The slope of the linear part is proportional to the density of topological defects in the system which is *fixed* by the magnitude of the twist at the ends of the system. The slope of the low-force regime is thus considerably smaller than in the high force regime $f \gg \mu$. For $f \gtrsim \mu$ the curves show a square-root dependence, $v \sim (f - \mu)^{1/2}$ and only in the high force limit they become linear again. The resulting force-velocity characteristics thus differ significantly from our results in the incommensurate phase, which is linear for all forces.

We conclude that the boundary conditions strongly affect the force-velocity characteristics. The reason is that in frustrated systems the presence of (open) boundaries supports the formation of topological defects which lead to depinning. Further, the entry barriers at the boundaries determine the rate at which defects enter the sample, thus ruling the dynamic behavior entirely. The main problem in determining the behavior of vortex-flow channels is thus to model realistic sample boundaries. Note that other boundary effects than considered here might modify the picture. For example, the vortex lattice of the channel environment may be distorted due to the presence of screening currents along the sample boundary causing a local variation of the frustration. Further, screening currents may lead to Bean-Livingston barriers for vortices which would increase the energy to form a defect at the sample edge. However, the conclusion that transport in artificial vortex-flow channels with a perfectly ordered vortex lattice in the environment is ruled by the entry barriers at the sample boundary persists even if further boundary effects are taken into account.

The picture that depinning occurs only via defect formation at the boundaries does not hold if inhomogeneities are present in the bulk. For example, local distortions of the vortex lattice in the channel environment caused by quenched disorder may generate weak spots that support the formation of vacancy-interstitial pairs at sufficiently large driving force.

To investigate this issue, we have extended the model by accounting for small static displacements $\mathbf{d}(\mathbf{r})$ of the vortices in the channel environment. We assumed the channel environment to be in the elastic limit, $|\nabla \cdot \mathbf{d}| \sim \xi/R_c \ll 1$, where ξ is the coherence length measuring the typical displacement within a distance given by the in-plane correlation length R_c for lattice distortions. Further, we assumed that close to the channel edges $\lambda\xi/R_c \ll a_0/2$ in order to obtain a local approximation for the displacement fields of the static vortices close to the channel edge. Since $\xi/R_c \ll 1$ this approximation should be valid as long as the penetration depth is not orders of magnitudes larger than the typical vortex lattice constants. Further, we took only into account longitudinal displacements along the channel edge. For narrow channels, $b_0 \sim w$, we then obtained a generalized amplitude and phase-disordered Frenkel-Kontorova model which in the continuum limit corresponds to a disordered Sine-Gordon model. Transverse displacements imply modifications of the

disordered phase and amplitude of the sinusoidal pinning force and to additional pinning force terms. This issue and its consequences for depinning have not been considered here.

In order to gain a basic understanding, we have first investigated depinning caused by a specific longitudinal vortex-lattice distortion field along the channel edges. Depending on their location, these distortions cause additional local frustration of the system modifying the threshold force for depinning. Distortions at the boundary of the sample affect the entry barrier for topological defects and cause shifts of the $\chi - f$ curve along the χ -axis. Local distortions in the bulk are shown to act as nucleation seeds reducing the threshold force.

Finally, we have studied the effect of small disorder-induced displacements of vortices in the channel environment. We model disorder by uncorrelated relative displacements which are represented by random values that are independent identically distributed according to a box-distribution. In the absence of frustration local lattice distortions in the channel environment lead to an effective channel potential with weak spots. At the weakest spots vacancy-interstitial pairs are formed when reaching the depinning threshold force. In the presence of frustration, a crossover from bulk depinning to boundary depinning occurs when the entry barrier becomes smaller than the smallest bulk pinning barrier. Increasing the frustration the entry barrier is decreased until it becomes smaller than the typical bulk pinning force for kinks due to disorder. Applying a finite driving force that is large enough to overcome the entry barrier, but smaller than the bulk pinning force, topological defects enter the channel and become pinned in the bulk. The finite depinning force in this regime is thus again determined by bulk properties. Increasing the driving force up to the threshold, topological defects which travel some distance until becoming trapped are successively introduced. Above the depinning threshold this leads to a jerky motion with successive depinning and pinning of topological defects.

Realizing that the Frenkel-Kontorova model (FKM) and the sine-Gordon model (SGM) are equivalent, the question arises, whether the disordered FKM studied here is related to the Fukuyama-Lee-Rice model (FLRM) [89–92] for charge density waves (CDW's). This question is especially interesting with respect to the characteristics of the depinning transition. The FLRM and simplified versions have been studied both analytically [93–96] and numerically [97–99], mostly in higher dimensions. The FLRM possesses a phase-disordered sinusoidal potential where the phases are chosen randomly from an interval $[-\pi, \pi]$. This model shows critical behavior for $d < 4$. Approaching the threshold from below, the critical state is formed by the release of avalanches characterized by typical sizes that diverge with a power-law behavior. Above threshold the motion is typically jerky [97] and the velocity shows a power-law behavior $v \sim (f - f_c)^\nu$, where the exponent ν depends on the dimensionality of the system.

One is tempted to say that vortex flow channels provide a physical realization of the one-dimensional FLRM. However, we find that the depinning process and the dynamics above threshold strongly depend on the the type of boundaries at the sample edges, the strength of the frustration, and the strength and type of disorder. In finite weakly disordered systems as studied in this work three depinning regimes can be identified. Increasing the frustration depinning first takes place via defect nucleation at weak spots in the bulk, then

via defect nucleation at the boundary, and finally by releasing pinned pre-existing defects when the frustration is so strong that the entry barrier for defects has become irrelevant.

This is indeed very different compared to the FLRM where system boundaries are not taken into account and the disorder is of a different type. If at all, characteristics of the FKLM like the avalanching below depinning threshold, the roughness of the critical state at threshold, and the jerky motion above the depinning threshold resemble to what we observe in the incommensurate state in the presence of weak disorder. However, to date it is unclear, whether the behavior of our model observed in numerical simulations at weak disorder and strong frustration is similar or even equivalent to what is known from the FLRM. It would be interesting to clarify this issue.

Finally, we compared the theoretical results to available experimental data [47–49, 88]. Sets of current voltage characteristics have been measured in the increasing-field (IF) and decreasing field (DF) mode. Whereas DF data display properties we can only vaguely interpret within our model, the low magnetic field IF data shows similar features as our disordered FKM.

Since the theoretical results are only valid for narrow channels with one mobile row, weak longitudinal disorder, and since the squeezing effects of channel edge currents were not taken into account, the interpretation of the available experimental data remains speculative. It would thus be interesting to extend the model to include these additional properties.

Chapter 4

Summary

In this thesis certain physical phenomena that emerge due to metastability and depinning in driven dissipative systems are studied. The two fields of interest, metastability and depinning are treated in separate and rather self-contained chapters.

First, we study the thermal and quantum decay of harmonically coupled degrees of freedom from a metastable state. Depending on the coupling strength, finite chains either behave like a point-like zero-dimensional object or like an elastic line, which is a one-dimensional manifold. One may then ask: How does the decay rate depend on the effective dimension of the system? Which decay regimes are encountered when the parameters that alter the dimension are varied? What types of transitions occur between the decay regimes? In which physical systems may the effects be observed ?

To answer these questions, we calculate the decay rate using the thermodynamic method. To shortly introduce this method and give an overview, we first review the current state of the art of rate theory. Starting with classical multi-dimensional systems, we re-derive the spatial-diffusion-limited decay rate in the Markovian limit. Following Langer [15], one either starts with a Fokker-Planck equation or the equivalent Langevin equation and ends up with a multi-dimensional generalization of Kramers' result for one-dimensional systems [54]. Langer applied his general formula to calculate the rate in the overdamped limit. Here we show that the range of validity can easily be extended to the moderate-to-strong damping limit. This possibility has been already noted by Grote and Hynes [58], but to our knowledge has never been derived explicitly within Langer's framework.

The thermal decay rate has the Arrhenius form $\Gamma_{cl} = P \exp(-\beta V_s)$, where V_s is the energy of a state most likely leading to decay from metastability and P is a pre-exponential factor taking into account the contributions of all equivalent states. In general, V_s and thus Γ_{cl} is a function of macroscopic external parameters that characterize the system under consideration. Upon tuning the parameters several distinct decay regimes may be entered. At the boundaries of these regimes the first or second derivative of V_s with respect to a system parameter may become discontinuous. Consequently, the corresponding derivative of the rate becomes discontinuous. In analogy to classical phase transitions, we define the crossovers between the decay regimes to be of first (second) order if the first (second) derivative of the rate becomes discontinuous.

The thermal decay rate of a harmonic chain trapped in a cubic-parabola potential undergoes a second order crossover from rigid to elastic decay. In the crossover regime, the prefactor of the rate P exhibits a universal scaling property. In the rigid regime, the stiffness of the chain is fairly large compared to the barrier height of the potential, such that the decay is particle-like (zero-dimensional). Elastic decay occurs when the interaction energy between the chain beads is much smaller than the barrier height. Then, the escape from the potential well takes place via line-like (one-dimensional) excitations. A finite chain with loose ends, energetically prefers to decay via nucleation at the system boundaries. These “surface” states most likely lead to elastic decay close to the rigid-elastic crossover. With increasing barrier height a second crossover from boundary to bulk nucleation occurs when the many possibilities to excite a state in the bulk outnumber the two surface states.

At low temperatures quantum fluctuations become relevant. To determine the low temperature rate, we apply quantum transition state theory, which is a specific limit of quantum reactive-flux theory neglecting barrier re-crossings. Within the semiclassical approximation, the decay rate is then found to have the form $\Gamma \sim \exp(-S_B/\hbar)$, where S_B is the extremal Euclidean action. In the high temperature limit, the rate converges to the classical one with $S_B/\hbar \rightarrow V_s/k_B T$. Reducing the temperature, quantum fluctuations first modify the classical pre-exponential factor. These quantum corrections are independent of dissipation terms. At still lower temperatures, when the thermal fluctuations are of the order of the quantum fluctuations, a second order crossover from thermal to quantum decay occurs at the characteristic temperature T_0 .

For the rigid regime the known single particle results apply. To determine the decay behavior of a chain of arbitrary length in the elastic regime, we use quantum rate theory. First, T_0 is evaluated close to the rigid-elastic crossover. Then, we calculate approximate solutions for the most probable chain configurations leading to decay, the non-uniform instantons. The instanton calculations are already non-trivial for a particle or an infinite line. The reason is that due to the peculiar form of the potential generating metastability one is confronted with the calculation of non-linear differential equations. Further complications arise due to an integral term with a non-local kernel when coupling the system to a heat bath to model dissipation. Whereas some equations arising in the decay problem of a chain of coupled particles can still be solved in the thermal regime, it is absolutely hopeless to find exact solutions in the quantum regime. One way to tackle the problem analytically is to linearize the equations appropriately. We have systematically worked out a perturbation scheme and have applied it to determine approximate non-uniform instanton solutions.

The extremal action S_B is obtained by evaluating the Euclidean action at the instanton solution. Analyzing S_B , we determine the crossover line from quantum rigid to quantum elastic decay. At low temperatures and low barrier height, the crossover is of second order. Interestingly, at higher temperatures and barrier height, a “tricritical” point exists beyond which the quantum rigid-to-elastic crossover is of first order. The various decay regimes are summarized in a decay diagram.

Finally, knowing the extremal action, we compute the decay rate to exponential accuracy, $\Gamma \sim \exp(-S_B/\hbar)$ in the quantum elastic regime. With this result, the decay rate of a finite overdamped chain in a weakly metastable state is now determined for all four

regimes.

We expect that the crossovers discussed here occur in many weakly metastable chain-like systems in the presence of dissipation. Here, the results are mainly discussed in the context of two systems, namely current-driven vortices in high temperature superconductors with columnar defects and one-dimensional current-biased Josephson Junction arrays, so called discrete Josephson transmission lines. The latter provide an ideal experimental system to observe the crossovers investigated here.

The last chapter of this thesis is devoted to the depinning transition in driven systems neglecting thermal or quantum fluctuations. Motivated by recent experiments on artificial vortex flow channels [47–49] we study the depinning of elastic chains and lines that interact with their environment.

First, we develop a model for artificial vortex flow channels. Starting from a London description of straight vortices in a superconductor, we calculate the effective channel potential produced by a static vortex lattice in the environment. The result, which is strictly valid only at inductions far below B_{c2} is generalized to higher inductions by taking into account the vortex core and by introducing a field dependent coherence length and penetration depth. To understand the basic depinning mechanisms, we consider only a single vortex row in the channel. Further, we simplify the problem by mapping the model onto a generalized Frenkel-Kontorova model [50] or equivalently, a Sine-Gordon model. Deriving the coefficients of the Frenkel-Kontorova model, we make use of the fact that in the experimentally interesting regime the magnetic inductions are so large that the average vortex spacing is of the order or smaller than the penetration depth. Then, the resulting channel potential is sinusoidal to a very good approximation. Further, since the vortex-vortex interactions drop off exponentially on distances larger than the penetration depth, within the channel only harmonic interactions between a finite number of nearest neighbors are taken into account. In the continuum Sine-Gordon limit this cut-off is used to obtain an effective local theory.

After deriving the coefficients of the Frenkel-Kontorova model, we investigate the Commensurate-Incommensurate transition commonly known to occur in this model at thermal equilibrium. Since our focus is on the depinning problem *in the absence of fluctuations*, we modify the theory. We define a “mechanical” Commensurability-Incommensurability transition. It turns out, that the boundaries of the system play a crucial role if one supposes that the number of static vortices in the strong pinning environment is constant: the purely mechanical Commensurate-Incommensurate transition occurs, if the entry barrier for discommensurations at the boundary vanishes.

This concept can be generalized to describe depinning at finite driving forces. The reason is that the entry barrier for discommensurations is reduced when a driving force is applied. Depinning takes place when the entry barrier for discommensurations vanishes. This occurs at frustrations below the zero force threshold frustration at which the mechanical Commensurate-Incommensurate transition occurs. In this regime, the entry barrier is by far the largest barrier in the system.

Above the zero-force threshold frustration, in the incommensurate regime, the entry barrier has vanished and discommensurations enter the system until the mutual repulsion

between the defects prevents new ones to flow in. The extremely small Peierls-Nabarro barrier which may arise due to the discreteness of the system [83] is not taken into account.

The analytically calculated threshold force is compared with data obtained by the Leiden group from molecular dynamics simulations of channels with a perfectly ordered environment and from measurements of the critical current in artificial vortex flow channels [49, 81, 88]. Unfortunately experimental data for a single vortex row in the channel has not been available, such that the comparison can only be made on a qualitative level. In the commensurate regime the experimentally obtained threshold force is reduced whereas in the incommensurate phase it is considerably enhanced compared to the calculated depinning force expected for an ordered channel.

The enhancement of the depinning threshold in the incommensurate phase is taken as an indication that quenched disorder in the channel environment plays an important role. To investigate the properties in the presence of disorder, weak vortex lattice distortions along the channel edges are introduced into the model. Weak perturbations are a reasonable assumption if the pinning energy due to point-like defects in the channel environment is much smaller than the interaction between the vortices. Further, we assume that lattice defects are not present in the pinned environment and that along the channel transverse distortions can be neglected if the material step at the channel edge produces a fairly strong pinning well. Taking only longitudinal lattice distortions into account we derive an integral expression for the effective channel potential. This expression is evaluated in the limit of small and smooth disorder induced lattice displacements. Performing similar derivation steps as in the perfectly ordered case we end up with a disordered Frenkel-Kontorova model and its continuous counterpart, the disordered Sine-Gordon model. Similar models are known from the Charge-Density-Wave studies [89–99]. The main difference to our model is that the disorder induced variations of the phase are smooth on the scale of a lattice constant.

To obtain a basic understanding of (de-)pinning in systems with a distorted vortex lattice environment, we study some simple examples. A similar line of reasoning was followed by Fukuyama back in the nineteen-seventies when Charge-Density-Wave models became en vogue [89]. The main difference to the problem treated here is that he was considering a system close to thermal equilibrium whereas here we are interested in the depinning behavior far from equilibrium. We identify typical configurations that act as sources which produce vacancy-interstitial pairs and thus lower the depinning threshold. These we call weak spots. We find also other configurations that pin the topological defects. The system is static if all topological defects that enter the system via the boundaries or are induced at weak spots are trapped by lattice distortions of the pinning type. Depinning takes place when the density of topological defects becomes larger than the density of pinning sites. It is thus clear that an enhancement of the depinning threshold can only occur in systems with a considerable amount of pinning sites formed by lattice distortions in the channel.

In order to investigate the depinning transition in channels with randomly distorted edges, we perform numerical simulations. By analyzing the time evolution of the displacement fields, we observe the main features described above: In the absence of frustration,

depinning occurs via the formation of vacancy-interstitial pairs at weak-spots generated by the randomly distorted vortex lattice in the channel edge. In the presence of frustration we find three regimes: At low frustration, the threshold for boundary nucleation is larger than the threshold for nucleation at weak spots in the bulk. Hence, depinning still occurs at weak spots. At larger frustration a crossover from bulk to boundary depinning occurs when the boundary depinning threshold becomes smaller than the weak-spot depinning threshold. When the frustration is further increased, the entry barrier for defects vanishes. Defects can enter the system until they become pinned and their mutual repulsion prevents new defects to flow into the system. Increasing the driving force, defects successively enter the system. The system depins, when all pinning sites are occupied. Then a new defect entering the system cannot become pinned and freely moves to the channel exit.

We obtain the force-velocity characteristics, the threshold force as a function of the frustration, and the threshold force as a function of the disorder for an ensemble of channels with randomly perturbed channel edges.

Appendix A

Thermal prefactor

A.1 Curvature Matrix: Determinant and eigenvalues

A.1.1 Recurrence relation for the Hessian matrix

As was shown in Sec. 2.3.2, the prefactor P of the thermal decay rate is a function of the determinant and the eigenvalues of the curvature matrix evaluated at the relative minimum and the saddle points, respectively, see Eq. (2.107). The curvature or Hessian matrix \mathbf{V}_N with matrix elements $V_{nm}(\mathbf{x}_0) = \partial_n \partial_m E(\mathbf{x}_0)$ determines the nature of E at the extremum \mathbf{x}_0 . If all eigenvalues of $\mathbf{V}_N(\mathbf{x}_0)$ are negative (positive), \mathbf{x}_0 is a relative maximum (minimum). If some of the eigenvalues are positive and some are negative, then \mathbf{x}_0 is a saddle point. For $E(\mathbf{x}_0)$ with $N \geq 3$, the Hessian matrix reads

$$\mathbf{V}_N(\mathbf{x}) = \begin{pmatrix} \partial_0^2 E(\mathbf{x}) & -\kappa & 0 & \cdots & 0 & -b\kappa \\ -\kappa & \ddots & \ddots & & & 0 \\ 0 & \ddots & \ddots & \ddots & & \vdots \\ \vdots & & \ddots & \ddots & \ddots & \vdots \\ 0 & & & \ddots & \ddots & -\kappa \\ -b\kappa & 0 & \cdots & 0 & -\kappa & \partial_{N-1}^2 E(\mathbf{x}) \end{pmatrix}.$$

In the case of open boundary conditions $b = 0$, the diagonal elements are given by

$$\partial_n^2 E(\mathbf{x}) = \begin{cases} \kappa + U''(x_n), & n = 0, N-1 \\ 2\kappa + U''(x_n), & 0 < n < N-1. \end{cases}$$

In the discussion that follows, we introduce

$$D_N = \det_N \begin{pmatrix} 1+z_0 & -1 & 0 & \cdots & 0 \\ -1 & 2+z_1 & -1 & \cdots & \vdots \\ \vdots & \ddots & \ddots & \ddots & \vdots \\ \vdots & \ddots & \ddots & 2+z_{N-2} & -1 \\ 0 & \cdots & 0 & -1 & 1+z_{N-1} \end{pmatrix}, \quad (\text{A.1})$$

which is used to calculate both the determinant and the characteristic polynomial of \mathbf{V}_N . For example, in order to calculate the determinant of the normalized Hessian \mathbf{V}_N/κ for $N > 4$, one sets $z_n = U''(x_n)/\kappa$. Below, we will derive a recurrence relation, which is used to determine D_N in some special cases.

By shifting the last column to the first and then lifting the bottom row to the top, one can rewrite the determinant as

$$D_N = \det_N \begin{pmatrix} 1 + z_{N-1} & 0 & 0 & \cdots & 0 & -1 \\ 0 & 1 + z_0 & -1 & 0 & \cdots & 0 \\ 0 & -1 & & & & \\ \vdots & 0 & & & & \\ 0 & \vdots & & A_{N-2} & & \\ -1 & 0 & & & & \end{pmatrix},$$

where the $(N-2) \times (N-2)$ matrix A_{N-2} is given by

$$A_{N-2} = \begin{pmatrix} 2 + z_1 & -1 & 0 & \cdots & 0 \\ -1 & 2 + z_2 & -1 & \cdots & \vdots \\ 0 & \ddots & \ddots & \ddots & 0 \\ \vdots & \ddots & -1 & 2 + z_{N-3} & -1 \\ 0 & \cdots & 0 & -1 & 2 + z_{N-2} \end{pmatrix}.$$

In the following, we will consider the case where $z_1 = \dots = z_{N-2} = z$. Note that z_0 and z_{N-1} can be arbitrary.

Expanding D_N , we find with $G_n = \det A_n$

$$\begin{aligned} D_N &= (1 + z_{N-1})[(1 + z_0)G_{N-2} - G_{N-3}] \\ &\quad - (1 + z_0)G_{N-3} + G_{N-4}. \end{aligned} \tag{A.2}$$

Expanding the determinant G_n according to the last row of A_n , one finds the recursive relation [100] $G_n = (2 + z_n)G_{n-1} - G_{n-2}$ that can be rewritten as a difference equation

$$(G_n - G_{n-1}) - (G_{n-1} - G_{n-2}) - z_n G_{n-1} = 0. \tag{A.3}$$

The initial conditions are given by the determinants G_1 and G_2 ,

$$\begin{aligned} G_1 &= 2 + z, \\ G_2 &= (2 + z)^2 - 1. \end{aligned} \tag{A.4}$$

For $2 \leq N \leq 4$, we can use the recurrence relations for G_n , if we define $G_0 = 1$, $G_{-1} = 0$, and $G_{-2} = -1$.

A.1.2 Uniform case

The solution of these difference equations is possible for special cases. We now analyze the uniform case where $z = z_0 = \dots = z_{N-1}$. Then Eq. (A.2) simplifies to

$$D_N = (1 + z)^2 G_{N-2} - 2(1 + z) G_{N-3} + G_{N-4}. \quad (\text{A.5})$$

Determinant at the relative minimum, $z \geq 0$

We first discuss the case of the local minimum $\mathbf{x} = \mathbf{x}_{min}$, where $z = \omega^2 > 0$. Imposing the initial conditions given by Eq. (A.4), one obtains a solution [100] of Eq. (A.3),

$$G_{N-1}^{min} = \frac{\sinh(N\Omega)}{\sinh \Omega}, \quad (\text{A.6})$$

where

$$\sinh \frac{\Omega}{2} = \frac{\omega}{2}.$$

Using Eqs. (A.5) and (A.6), we obtain

$$D_N^{min} = \omega^2 G_{N-1}^{min} = 2 \tanh\left(\frac{\Omega}{2}\right) \sinh(N\Omega). \quad (\text{A.7})$$

Determinant at the rigid saddle, $z < 0$

In the same way as for the local minimum, one obtains D_N at the rigid saddle $\mathbf{x} = \mathbf{x}_{rs}$ but now with negative $z = -\tilde{\omega}^2 < 0$. One finds

$$G_{N-1}^{rs} = \frac{\sin(N\tilde{\Omega})}{\sin \tilde{\Omega}},$$

where

$$\sin \frac{\tilde{\Omega}}{2} = \frac{\tilde{\omega}}{2}, \quad (\text{A.8})$$

and hence

$$D_N^{rs} = 2 \tan\left(\frac{\tilde{\Omega}}{2}\right) \sin(N\tilde{\Omega}) \quad (\text{A.9})$$

Eigenvalues

The eigenvalues of \mathbf{V}_N are found by evaluating the roots of the characteristic polynomial, $\det(\mathbf{V}_N - \mu \mathbf{I}) = 0$. We have again a determinant of the form of Eq. (A.1), but now with $z_n = U''(x_n)/\kappa - \mu/\kappa$, such that we can define $D_N(\mu) = \kappa^{-N} \det(\mathbf{V}_N - \mu \mathbf{I})$. Using Eq. (A.9) we find that the roots where $D_N(\mu) = 0$ are given by $\tilde{\Omega}_m = m\pi/N$, where $m = 0, \dots, N-1$. Inserting $\tilde{\Omega}_m$ into Eq. (A.8) yields $\tilde{\omega}_m = 2 \sin(\tilde{\Omega}_m/2)$, hence $D_N(\mu_m) = 0$ for

$$\mu_m = 4\kappa \sin^2\left(\frac{m\pi}{2N}\right) + U''(x_0), \quad (\text{A.10})$$

which are the eigenvalues of $\mathbf{V}_N(\mathbf{x}_0)$ for a given uniform extremal solution $\mathbf{x}_0 = (x_0, \dots, x_0)$.

A.1.3 Nonuniform case

Approximate solutions for the determinant and the eigenvalues can be obtained deep in the elastic regime, $\Delta/\Delta_* \gg 1$.

Elastic boundary saddle ($\Delta_{bs} > \Delta \gg \Delta_*$)

For the elastic boundary saddle-point configurations obtained in Eqs. (2.97)-(2.99), to highest order in Δ/Δ_* one finds that $U''(x_0) = \dots = U''(x_{N-3}) \approx 6U_B\Delta/r^2$, $U''(x_{N-2}) \approx 6U_B\Delta/r^2 - 2\kappa$, and $U''(x_{N-1}) \approx -6U_B\Delta/r^2 - 2\kappa$.

With $z_n = U''(x_n)/\kappa$ one obtains for the determinant up to $\mathcal{O}(\Delta^{N-2})$

$$D_N^{es} \approx (1 + z_{N-1})(2 + z_{N-2})(1 + z_0)G_{N-3}^{min}. \quad (\text{A.11})$$

The ratio D_N^{min}/D_N^{es} , which is needed to calculate the prefactor in the elastic regime is found to be

$$\frac{D_N^{min}}{D_N^{es}} = -1 - \frac{\kappa r^2}{3U_B\Delta} + \mathcal{O}[(\Delta_*/\Delta)^2].$$

To calculate the eigenvalues, we set again $z_n = U''(x_n)/\kappa - \mu/\kappa$. The characteristic polynomial $D_N(\mu)$ is now up to $\mathcal{O}(\Delta^{N-2})$, given by

$$D_N(\mu) \approx (1 + z_{N-1})(2 + z_{N-2})(1 + z_0)G_{N-3}(\mu).$$

Thus, to lowest order in Δ , we find that the smallest eigenvalue is

$$\mu_0^{es} \approx -\kappa - \frac{6U_B\Delta}{r^2}. \quad (\text{A.12})$$

Elastic bulk saddle ($\Delta > \Delta_{bs}$)

For the elastic bulk saddle-point configurations obtained in Eqs. (2.101) and (2.102) to highest order in Δ/Δ_* one finds for a double kink situated at m , $U''(x_m) \approx -6U_B\Delta/r^2 - 4\kappa$, $U''(x_{m\pm 1}) \approx 6U_B\Delta/r^2 - 4\kappa$, and for $|n - m| > 1$ $U''(x_n) \approx 6U_B\Delta/r^2$. With $z_n = U''(x_n)/\kappa$ and using periodic boundary conditions, the determinant is approximately given by

$$D_N^{bs} \approx (2 + z_{m+1})(2 + z_m)(2 + z_{m-1})G_{N-3}^{min}.$$

The ratio D_N^{min}/D_N^{bs} is

$$\frac{D_N^{min}}{D_N^{bs}} = -1 - \frac{4\kappa r^2}{3U_B\Delta} + \mathcal{O}[(\Delta_*/\Delta)^2]. \quad (\text{A.13})$$

The characteristic polynomial $D_N(\mu)$ is now up to $\mathcal{O}(\Delta^{N-2})$ given by

$$D_N(\mu) \approx (2 + z_{m+1})(2 + z_m)(2 + z_{m-1})G_{N-3}(\mu),$$

where $z_n = U''(x_n)/\kappa - \mu/\kappa$. Thus, to lowest order in Δ , we find that the smallest eigenvalue is

$$\mu_0^{bs} \approx -2\kappa - \frac{6U_B\Delta}{r^2}. \quad (\text{A.14})$$

A.2 Prefactor in the crossover regime

A.2.1 Rigid regime ($\Delta \lesssim \Delta_*$)

For $\Delta \rightarrow \Delta_*$, both the eigenvalue μ_1^{rs} and the determinant D_N^{rs} vanish. Hence the Gaussian integral containing μ_1^{rs} in Eq. (2.107) diverges, and third-order terms in q_1 have to be taken into account. In the rigid regime, the third-order expansion of E in q_1 is given by Eq. (2.84). The contributions to P of all degrees of freedom except $q_1 \in \mathcal{S}$ are found by Gaussian integration:

$$P = \frac{1}{2\pi} \left(\sqrt{\frac{\gamma^2}{4} + \frac{3U_B\Delta_*|\lambda_0^{rs}|}{mr^2}} - \frac{\gamma}{2} \right) \left(\frac{|\lambda_0^{rs}| \prod_{n=0}^{N-1} \lambda_n^{min}}{\prod_{n=2}^{N-1} \lambda_n^{rs}} \right)^{1/2} \left(\frac{3NU_B\Delta^3}{2\pi k_B T} \right)^{1/2} \\ \times \int_{-\infty}^{\infty} dq_1 \exp \left[-\frac{3NU_B\Delta^3}{2k_B T} (\lambda_1^{rs} q_1^2 + Dq_1^4) \right], \quad (\text{A.15})$$

where $D = 2\pi\delta$ as defined above in Eq. (2.87) arises during the Gaussian integrations over q_0 and q_2 . In the following we first derive an approximate expression for $\prod \lambda_n^{min} / \prod_{n \neq 1} \lambda_n^{rs}$ and then evaluate the remaining integral over q_1 .

For the calculation of the product term we use the relation

$$\prod \lambda_n^{min} / \prod_{n \neq 1} \lambda_n^{rs} = \lambda_1^{rs} D_N^{min} / D_N^{rs}.$$

Let us analyze D_N^{rs} for λ_1^{rs} close to zero. Recall that

$$\tilde{\omega}^2 = -\frac{U''(u_0)}{\kappa} = 4 \sin^2 \left(\frac{\pi}{2N} \right) - \frac{\mu_1^{rs}}{\kappa}.$$

Inserting this expression into Eq. (A.8) in the limit of small μ_1^{rs} , we find

$$\tilde{\Omega} \approx \frac{\pi}{N} - \frac{\mu_1^{rs}}{2\kappa \sin(\pi/N)},$$

such that, to lowest order in μ_1^{rs} ,

$$\sin(N\tilde{\Omega}) \approx \frac{N\mu_1^{rs}}{2\kappa \sin(\pi/N)},$$

and

$$\tan \left(\frac{\tilde{\Omega}}{2} \right) \approx \tan \left(\frac{\pi}{2N} \right).$$

Hence

$$\lambda_1^{rs} \frac{D_N^{min}}{D_N^{rs}} = -\frac{\kappa r^2}{3NU_B\Delta} \cos^2 \left(\frac{\pi}{2N} \right) \tanh \left(\frac{\Omega}{2} \right) \sinh(N\Omega).$$

The integration over q_1 yields

$$\begin{aligned} & \int_{-\infty}^{\infty} dq_1 \exp \left[-\frac{3N\tilde{U}_B}{2k_B T} (\lambda_1^{rs} q_1^2 + Dq_1^4) \right] \\ &= \frac{1}{2} \sqrt{\frac{\lambda_1^{rs}}{D}} \exp \left[\frac{3N\tilde{U}_B(\lambda_1^{rs})^2}{16k_B T D} \right] K_{1/4} \left[\frac{3N\tilde{U}_B(\lambda_1^{rs})^2}{16k_B T D} \right], \end{aligned} \quad (\text{A.16})$$

where $K_{1/4}$ is the modified Bessel function. We make the substitution $\lambda_1^{rs} = -2\epsilon$. After defining

$$\begin{aligned} P_s &= \frac{1}{2\pi} \left(\sqrt{\frac{\gamma^2}{4} + \frac{3U_B \Delta_* |\lambda_0^{rs}|}{mr^2}} - \frac{\gamma}{2} \right) \left(\frac{|\lambda_0^{rs}| \prod_{n=0}^{N-1} \lambda_n^{min}}{\prod_{n=2}^{N-1} \lambda_n^{rs}} \right)^{1/2} \left(\frac{3NU_B \Delta^3}{4\pi^2 k_B T D} \right)^{1/4} \\ &\approx \left(\sqrt{\frac{\gamma^2}{4} + \frac{3U_B \Delta_* |\lambda_0^{rs}|}{mr^2}} - \frac{\gamma}{2} \right) \frac{[\tanh(\Omega/2) \sinh(N\Omega)]^{1/2}}{4\pi \tan(\pi/2N)} \left(\frac{3U_B \Delta_*^3}{8\pi^3 N k_B T \delta} \right)^{1/4} \end{aligned} \quad (\text{A.17})$$

and

$$\epsilon_s = \left(\frac{4k_B T D}{3N \Delta_*^3 U_B} \right)^{1/2}, \quad (\text{A.18})$$

which are constants to leading order in ϵ , we obtain the prefactor of the rate for the rigid region of the crossover regime $\delta \lesssim \delta_*$:,

$$P(\epsilon) = \frac{\pi P_s}{\sqrt{2}} \sqrt{\left| \frac{\epsilon}{\epsilon_s} \right|} \left[I_{-1/4} \left(\frac{\epsilon^2}{\epsilon_s^2} \right) - I_{1/4} \left(\frac{\epsilon^2}{\epsilon_s^2} \right) \right] \exp \left(\frac{\epsilon^2}{\epsilon_s^2} \right). \quad (\text{A.19})$$

A.2.2 Elastic regime ($\Delta \gtrsim \Delta_*$)

In the elastic regime near the crossover, where $\epsilon \gtrsim 0$, we expand $\mathcal{V}(\mathbf{q})$ around the perturbative elastic saddle-point solution (2.85),

$$\mathcal{V}(\mathbf{q}) = \mathcal{V}(\mathbf{q}_{es}) + \frac{1}{2} \mathcal{V}^{(2)}(\{\xi_k\}) + \frac{1}{6} \mathcal{V}^{(3)}(\{\xi_k\}),$$

where $\mathcal{V}^{(2)}$ and $\mathcal{V}^{(3)}$ contain the terms of second and third order, respectively, and $\xi_k = q_k - q_k^{es}$ are the fluctuations around the elastic saddle point. By introducing the shifted fluctuation coordinates for $m \neq 1$,

$$\hat{\xi}_m = \xi_m + \frac{2q_1^{es} \xi_1 A_m}{\lambda_m^{rs}},$$

with $A_0 = -2$, $A_2 = -\sqrt{2}$ and $A_{i>2} = 0$, we find, for the quadratic part to leading order in ϵ ,

$$\mathcal{V}^{(2)} = -2\lambda_1^{rs} \xi_1^2 + \sum_{m \neq 1} \lambda_m^{rs} \hat{\xi}_m^2.$$

Note that λ_m^{rs} are the dimensionless eigenvalues evaluated at the *rigid* saddle-point configuration. Within the crossover regime, to leading order in ϵ , the eigenvalues at the elastic saddle-point solution $\lambda_{i \neq 1}^{es} = \lambda_{i \neq 1}^{rs}$ are independent of ϵ , except $\lambda_1^{es} = -2\lambda_1^{rs} = \epsilon$. The higher order contributions to the expansion read

$$\frac{1}{6}\mathcal{V}^{(3)} = \left(\sum_{m \neq 1} A_m \hat{\xi}_m \right) \xi_1^2 + 2Dq_1^{es} \xi_1^3.$$

Transforming the fluctuation coordinates a second time,

$$\begin{aligned} \tilde{\xi}_{m \neq 1} &= \hat{\xi}_m + \frac{A_m}{\lambda_m^{rs}} \xi_1^2, \\ \tilde{\xi}_1 &= \xi_1 + q_1^{es}, \end{aligned}$$

we find

$$\mathcal{V}(\mathbf{q}) = \mathcal{V}(\mathbf{q}_{es}) + \frac{1}{2} \sum_{m \neq 1} \lambda_m^{rs} \tilde{\xi}_m^2 + \frac{D}{2} \left[\tilde{\xi}_1^2 - (q_1^{es})^2 \right]^2.$$

By using $(q_1^{es})^2 = -\lambda_1^{rs}/2D = \epsilon/D$, we evaluate the integrals as in the previous paragraph, [101]

$$\begin{aligned} & \int_{-\infty}^{\infty} d\tilde{\xi}_1 \exp \left\{ -\frac{D}{2k_B T} \left[\tilde{\xi}_1^2 - (q_1^{es})^2 \right]^2 \right\} \\ &= \frac{\pi}{2\sqrt{2}} \sqrt{\left| \frac{\lambda_1^{rs}}{D} \right|} \left\{ I_{-1/4} \left[\frac{(\lambda_1^{rs})^2}{16k_B T D} \right] + I_{1/4} \left[\frac{(\lambda_1^{rs})^2}{16k_B T D} \right] \right\} \\ & \times \exp \left[-\frac{(\lambda_1^{rs})^2}{16k_B T D} \right], \end{aligned} \tag{A.20}$$

where $I_{1/4}$ and $I_{-1/4}$ are modified Bessel functions. The prefactor of the rate for the elastic regime $\Delta \gtrsim \Delta_*$ in the crossover region then reads

$$P(\epsilon) = \frac{\pi P_s}{\sqrt{2}} \sqrt{\frac{\epsilon}{\epsilon_s}} \left[I_{-1/4} \left(\frac{\epsilon^2}{\epsilon_s^2} \right) + I_{1/4} \left(\frac{\epsilon^2}{\epsilon_s^2} \right) \right] \exp \left(\frac{\epsilon^2}{\epsilon_s^2} \right). \tag{A.21}$$

Bibliography

- [1] P. Hänggi, P. Talkner, and M. Borkovec, *Rev. Mod. Phys.* **62**, 251 (1990).
- [2] I. Affleck, *Phys. Rev. Lett.* **46**, 388 (1981).
- [3] A. O. Caldeira and A. J. Leggett, *Phys. Rev. Lett.* **46**, 211 (1981).
- [4] A. O. Caldeira and A. J. Leggett, *Ann. Phys.* **149**, 374 (1983).
- [5] A. O. Caldeira and A. J. Leggett, *Physica A* **121**, 587 (1983).
- [6] A. I. Larkin and Y. N. Ovchinnikov, *Zh. Eksp. Theor. Fiz.* **85**, 1510 (1983); *Sov. Phys. JETP* **57**, 876 (1983).
- [7] A. I. Larkin and Y. N. Ovchinnikov, *Zh. Eksp. Theor. Fiz.* **86**, 719 (1984); *Sov. Phys. JETP* **59**, 420 (1984).
- [8] H. Grabert, U. Weiss, and P. Haengggi, *Phys. Rev. Lett.* **52**, 2193 (1984).
- [9] H. Grabert and U. Weiss, *Phys. Rev. Lett.* **53**, 1787 (1984).
- [10] H. Grabert and U. Weiss, *Z. Phys. B* **56**, 171 (1984).
- [11] H. Grabert, P. Olschowski, and U. Weiss, *Phys. Rev. B* **36**, 1931 (1987).
- [12] U. Weiss, in *Quantum Dissipative Systems*, Vol. 2 of *Series in Modern Condensed Matter Physics*, 2nd ed., edited by I. E. Dzyaloshinski, S. O. Lundquist, and Y. Lu (World Scientific, Singapore, 1999).
- [13] J. S. Langer, *Ann. Phys. (N.Y.)* **41**, 108 (1967).
- [14] J. S. Langer, *Phys. Rev. Lett.* **21**, 973 (1968).
- [15] J. S. Langer, *Ann. Phys. (N.Y.)* **54**, 258 (1969).
- [16] S. Coleman, *Phys. Rev. D* **15**, 2929 (1977).
- [17] C. G. Callan and S. Coleman, *Phys. Rev. D* **16**, 1762 (1977).
- [18] E. M. Chudnovsky, *Phys. Rev. A* **46**, 8011 (1992).

- [19] E. M. Chudnovsky and D. A. Garanin, Phys. Rev. Lett. **79**, 4469 (1997); D. A. Garanin and E. M. Chudnovsky, Phys. Rev. B **56**, 11102 (1997); D. A. Garanin, X. Martinez Hidalgo, and E. M. Chudnovsky Phys. Rev. B **57**, 13639 (1998); D. A. Garanin and E. M. Chudnovsky, Phys. Rev. B **59**, 3671 (1999).
- [20] K. K. Likharev, Zh. Eksp. Teor. Fiz. **61**, 1700 (1971); Sov. Phys. JEPT **34**, 906, (1972).
- [21] S. Hontsu and J. Ishii, J. Appl. Phys. **63**, 2021 (1988).
- [22] G. K. G. Hohenwarter *et al.*, IEEE Trans. Magn. **25**, 954 (1989).
- [23] A. V. Ustinov, priv. comm. (1999).
- [24] H. Simanjuntak and L. Gunther, Phys. Rev. B **42**, 930 (1990).
- [25] M. G. Castellano *et al.*, Phys. Rev. B **54**, 15417 (1996).
- [26] H. Simanjuntak and L. Gunther, J. Phys. C **9**, 2075 (1997).
- [27] H. C. Brinkmann, Physica (Utrecht) **22**, 149 (1956); R. Landauer and J. A. Swanson, Phys. Rev. **121**, 1668 (1961).
- [28] G. Grüner, Rev. Mod. Phys. **60**, 1129 (1988).
- [29] S. Bhattacharya and M. J. Higgins, Physica C **257**, 232 (1996).
- [30] R. Seshadri and R. M. Westervelt, Phys. Rev. B **46**, 5142 (1992).
- [31] R. Seshadri and R. M. Westervelt, Phys. Rev. B **46**, 5150 (1992).
- [32] V. M. Vinokur, P. H. Kes, and A. E. Koshelev, Physica C **168**, 29 (1990).
- [33] L. Balents and M. P. A. Fisher, Phys. Rev. Lett. **75**, 4270 (1995).
- [34] D. Cule and T. Hwa, Phys. Rev. Lett. **77**, 278 (1996).
- [35] V. L. Pokrovsky and A. L. Tapalov, Phys. Rev. Lett. **42**, 65 (1979).
- [36] G. Blatter, M. V. Feigel'man, V. B. Geshkenbein, A. I. Larkin, and V. Vinokur, Rev. Mod. Phys. **66**, 1125 (1994).
- [37] S. Bhattacharya and M. J. Higgins, Phys. Rev. Lett. **70**, 2616 (1995).
- [38] S. Bhattacharya and M. J. Higgins, Physica C **257**, 232 (1996).
- [39] R. Wordenweber, P. Kes, and C. Tsuei, Phys. Rev. B **33**, 3172 (1986).
- [40] P. Berghuis and P. Kes, Phys. Rev. B **47**, 262 (1993).

- [41] A. C. Marley, M. J. Higgins, and S. Bhattacharya, Phys. Rev. Lett. **74**, 3029 (1995).
- [42] G. D'anna *et al*, Phys. Rev. Lett. **75**, 3521 (1995).
- [43] H. J. Jensen, A. Brass, and A. J. Berlinsky, Phys. Rev. Lett. **60**, 1676 (1988).
- [44] H. J. Jensen, A. Brass, Y. Brecht, and A. J. Berlinsky, Phys. Rev. B **38**, 9235 (1988).
- [45] H. J. Jensen, Y. Brechet, and A. Brass, J. Low Temp. Phys. **74**, 293 (1989).
- [46] M. C. Hellerquist *et al*, Phys. Rev. Lett. **76**, 4022 (1996).
- [47] A. Pruymboom and P. H. Kes, Phys. Rev. Lett. **60**, 1430 (1988).
- [48] M. H. Theunissen, E. Van der Drift, and P. H. Kes, Phys. Rev. Lett. **77**, 159 (1996).
- [49] R. Besseling, R. Niggebrugge, and P. H. Kes, Phys. Rev. Lett. **82**, 3144 (1999).
- [50] J. Frenkel and T. Kontorova, Zh. Eksp. Teor. Fiz. **8**, 1340 (1938); Phys. Z. Sov. **13**, 1 (1938).
- [51] J. H. Van't Hoff, *Études de Dynamiques Chimiques* (F. Muller and Co., Amsterdam, 1884).
- [52] S. Arrhenius, Z. Phys. Chem. (Leipzig) **4**, 226 (1889).
- [53] L. Farkas, Z. Phys. Chem. (Leipzig) **125**, 236 (1927).
- [54] H. A. Kramers, Physica **7**, 284 (1940).
- [55] J. Ankerhold and H. Grabert, Phys. Rev. E **52**, 4704 (1995).
- [56] R. F. Grote and J. T. Hynes, J. Chem. Phys. **73**, 2715 (1980).
- [57] M. Polanyi and E. Wigner, Z. Phys. Chem. Abt. A **139**, 439 (1928).
- [58] R. F. Grote and J. T. Hynes, J. Chem. Phys. **74**, 4465 (1981).
- [59] E. HersHKovitz and E. Pollak, J. Chem. Phys. **106**, 8 (1997).
- [60] R. Zwanzig, J. Stat. Phys. **9**, 215 (1973).
- [61] W. H. Miller, J. Chem. Phys. **61**, 1823 (1974).
- [62] W. H. Miller, J. Chem. Phys. **62**, 1899 (1975).
- [63] M. C. Gutzwiller, J. Math. Phys. **12**, 343 (1971).
- [64] P. Hänggi and W. Hontscha, J. Chem. Phys. **88**, 4094 (1988).
- [65] R. P. Feynman and F. L. Vernon, Ann. Phys. **24**, 118 (1963).

- [66] R. D. Bock, J. R. Phillips, H. J. S. van der Zant, and T. P. Orlando, *Phys. Rev. B* **49**, 10009 (1994).
- [67] A. E. Koshelev, P. Le Doussal, and V. M. Vinokur, *Phys. Rev. B* **53**, R8855 (1996).
- [68] V. Lefevre-Seguin, E. Turlot, C. Urbina, D. Esteve, and M. H. Devoret, *Phys. Rev. B* **46**, 5507 (1992).
- [69] T. Christen, *Europhys. Lett.* **31**, 181 (1995); *Phys. Rev. E*, **51**, 604 (1995).
- [70] B. Ivlev and Y. N. Ovchinnikov, *Zh. Eksp. Teor. Fiz.* **93**, 668 (1987); *Sov. Phys. JETP* **66**, 378 (1987).
- [71] C. Morais Smith, B. Ivlev, and G. Blatter, *Phys. Rev. B* **49**, 4033 (1994).
- [72] S. Han, J. Lapointe, and J. E. Lukens, *Phys. Rev. Lett.* **63**, 1712 (1989).
- [73] E. H. Brandt, *Europhys. Lett.* **18**, 635 (1992).
- [74] D. R. Nelson and V. M. Vinokur, *Phys. Rev. Lett.* **68**, 2398 (1992).
- [75] T. Dröse and C. Morais-Smith, *Phys. Rev. B* **61**, 1506 (2000).
- [76] D. A. Gorokhov and G. Blatter, *Phys. Rev. B* **56**, 3130 (1997).
- [77] T. Dröse and C. Morais-Smith, *Phys. Rev. B* **60**, 9763 (1999).
- [78] P. Le Doussal and T. Giamarchi, *Phys. Rev. B* **57**, 11356 (1998).
- [79] A. E. Koshelev, *Physica C* **223**, 276 (1994).
- [80] A. E. Koshelev, *Phys. Rev. B* **51**, 12063 (1995).
- [81] R. Besseling and P. H. Kes, *priv. comm.* (2000).
- [82] E. H. Brandt, *Phys. Rev. B* **34**, 6514 (1986).
- [83] O. M. Braun and Y. S. Kivshar, *Phys. Rep.* **306**, 1 (1998).
- [84] M. Büttiker and R. Landauer, *Phys. Rev. A* **23**, 1397 (1981).
- [85] S. Aubry, *J. Phys. D* **7**, 240 (1983).
- [86] E. H. Brandt, *Phys. Status Solidi B* **77**, 551 (1976).
- [87] T. Giamarchi and P. Le Doussal, *Phys. Rev. B* **52**, 1242 (1995).
- [88] R. Besseling, PhD thesis, Leiden University, to be published (2001).
- [89] H. Fukuyama, *J. Phys. Soc. Jpn.* **41**, 513 (1976).

- [90] H. Fukuyama and P. A. Lee, Phys. Rev. B **17**, 535 (1978).
- [91] H. Fukuyama, J. Phys. Soc. Jpn. **45**, 1474 (1978).
- [92] P. A. Lee and T. M. Rice, Phys. Rev. B **19**, 3970 (1979).
- [93] D. S. Fisher, Phys. Rev. Lett. **50**, 1468 (1981).
- [94] D. S. Fisher, Phys. Rev. B **31**, 1396 (1981).
- [95] O. Narayan and D. S. Fisher, Phys. Rev. Lett. **68**, 3615 (1992).
- [96] O. Narayan and D. S. Fisher, Phys. Rev. B **46**, 11520 (1992).
- [97] S. N. Coppersmith and D. S. Fisher, Phys. Rev. A **38**, 6338 (1988).
- [98] A. A. Middleton and D. S. Fisher, Phys. Rev. Lett. **66**, 92 (1991).
- [99] C. R. Myers and J. P. Sethna, Phys. Rev. B **47**, 11171 (1993).
- [100] I. M. Gelfand and A. M. Yaglom, J. Math. Phys. **48**, 1 (1960).
- [101] I. S. Gradshteyn and I. M. Ryzhik, in *Table of Integrals, Series, and Products*, 5 ed., edited by A. Jeffrey (Academic Press, London, 1994), Chap. 3.54, No. 3.548.

Acknowledgments

At this point I would like to express my gratitude to all people who supported me. First of all, I would like to mention Prof. Dr. C. de Morais Smith who gave me the opportunity to write this thesis and who supported me until the end. The many discussions we had were both inspiring and motivating. She opened many opportunities to let me participate on international conferences and workshops. I want to thank her for all that.

I thank Prof. Dr. H. Schmidt for initiating this project and for the discussions we had. It was a pleasure to discuss with Prof. Dr. J. Kötzler, Prof. Dr. J. Appel, Dr. D. Reiß, Dr. A. Huck, Dr. A. van Otterlo, Dr. Isa Zharekeshev, Dr. N. Hasselmann, S. Willenbücher, F. Mintert, and T. Vorrath.

A special thank goes to Prof. Dr. D. Baeriswyl, who arranged my scientific visit at the University of Fribourg. He was a great host during my entire stay and whenever I passed by. I am grateful for the invitations from Prof. Dr. G. Blatter, Prof. Dr. A. Ustinov, and Prof. Dr. P. Kes and the chance to give talks in their seminars.

It really was a pleasure to collaborate with Dr. R. Besseling by excessively using communication media. I appreciated the valuable exchange of ideas I had with him.

Last, but not least, I want to thank Svenja, Lukas, Margit, Gerhard, Henner, and Sigrid for patience, never ending support, and encouragement.